



**UNIVERSITÀ
DI TRENTO**

Department of Physics
Doctoral Program in Physics
XXXV Cycle

**Laser Ablation Propulsion:
Synthesis and Analysis of
Materials and Impulse
Measurements**

Candidate:
Pietro Battocchio

Supervisor:
Prof. Antonio Miotello

Contents

Introduction	1
1 New Space Economy	5
1.1 Space Debris	6
1.2 Nanosatellite propulsion	7
1.3 Laser Ablation Propulsion	12
2 Laser Ablation	25
2.1 Metals	26
2.1.1 Laser-material interaction and heating	26
2.1.2 Mass ejection mechanisms	28
2.2 Polymers	33
2.2.1 Ablation mechanisms	34
2.2.2 Experimental observations	36
2.3 Laser Ablation Propulsion	37
3 Experimental setup	47
3.1 Considerations	47
3.1.1 Experimental techniques for impulse measurements	48
3.2 Apparatus for impulse measurement	51
3.2.1 Technical design of the apparatus	51
3.2.2 Physical analysis of pendulum motion	58
3.3 Data analysis	60
3.3.1 Video tracking	60
3.3.2 From displacement to pendulum motion	64
3.3.3 Analysis of pendulum motion	67
3.4 Measurement of mass parameters of the pendulum	69
3.5 Test of the performances of the apparatus	71

3.5.1	Damping	71
3.5.2	Impulse measurement	73
3.5.3	Ablated mass measurement	74
4	Beam homogeneity	79
4.1	Problems related to laser fluence	79
4.2	Non-uniform beam energy distribution	81
4.2.1	Measurement of energy deposited on target	82
4.2.2	Measurement of the irradiated area	83
4.2.3	Impulse measurement	84
4.3	Uniform energy distribution	89
4.4	Optimal configuration	91
5	Impulse generation by PVC	95
5.1	Sample preparation	96
5.1.1	Materials	96
5.1.2	Preparation procedure	97
5.2	Characterization	100
5.2.1	Sample structure	100
5.2.2	Differential Scanning Calorimetry (DSC)	100
5.2.3	Thermal Desorption Spectroscopy (TDS)	104
5.2.4	UV-visible spectroscopy	107
5.2.5	Impulse measurements	110
5.3	Discussion	116
6	Role of CNPs in PVC ablation	121
6.1	Sample preparation	122
6.1.1	Materials	122
6.1.2	Preparation procedure	122
6.2	SEM analysis of samples	123
6.3	Optical characterization	126
6.4	Impulse measurement	129
6.5	Analysis of ablation craters	131
6.6	Correlation with size	133
7	Open problems and future works	137
7.1	Impulse generated by multiple laser pulses	138
7.2	Measurements of specific impulse	140

CONTENTS

v

7.3 Confined ablation 143

Conclusion **147**

Introduction

Among the many possible applications of laser ablation one of the more recent taken is related to nanosatellites propulsion. The study of Laser Ablation Propulsion (LAP) requires research activity on different fields like high power pulsed lasers, laser ablation itself, because it is still a problem to relate the well known mechanisms to impulse generation, and finally materials that represent the fuel in LAP.

This thesis presents a research activity on LAP from its very beginning, with the development of an experimental apparatus to measure laser generated impulse and the first results on metals and polymers that paves the way to the development of future LAP materials.

Chapter 1 presents an overview of the actual situation of space economy and its recent fast evolution that led in the last years to the exploitation of space for many different applications, also by private companies. The so called New Space Economy is the background on which LAP develops, as an attractive propulsion technique for nano satellites, nowadays extremely diffused in all kind of space missions, and as a possible solution for the space debris problem. In this Chapter typical results obtained in LAP are also reviewed and compared with other solutions both for space debris and propulsion, in order to obtain a better image of its applicability range.

Chapter 2 deals with laser ablation. Initially the parameters that play a role in laser ablation are discussed, in particular those related to the laser source like wavelength, pulse duration and repetition rate, to give an overview of the experimental conditions involved. Then general phenomenological observations on laser ablation are presented and related to the physical mechanisms involved, both in the case of metals and polymers, highlighting the main differences between these two classes of materials.

The experimental part of this thesis starts in Chapter 3, with the description of the experimental apparatus developed to measure the laser generated mechanical impulses in the order of $\mu\text{N s}$. The different strategies to perform this kind of measurements are reviewed and compared to the one adopted in this work, based on a ballistic pendulum, and main advantages and problems are discussed. A technical description of the apparatus is given, focusing in particular on all the precautions that have been taken in order to let the pendulum operate in as ideal as possible conditions. The measurement procedure developed during this work is then described in detail, by discussing data analysis and showing some examples.

Chapter 4 also deals with the development of the apparatus, in particular for what concerns the estimation of the laser energy density that reaches the target material (fluence), a fundamental parameter for LAP measurements. Some measurements on metals are also presented here in order to discuss some features related to the measurements of some common LAP parameters.

Chapter 5 and 6 deal with LAP using polymers, and in particular with experiments devoted to the understanding of material properties that mainly affect LAP performances. The starting material chosen for these experiments is poly(vinyl chloride)(PVC), a benchmark in LAP experiments. Chapter 5 compares localized or uniform laser absorption by PVC, that can be obtained respectively by including carbon nanoparticles in the polymer matrix or by mixing PVC with an absorbing polymer (poly(styrene sulfonate)). The comparison is carried out from the optical and thermodynamical point of view, along with impulse generation. Specific ablation mechanisms are also discussed, showing that a localized absorption of laser radiation is more energetically efficient for impulse generation.

Chapter 6 then continues the work on PVC containing nanoparticles, investigating the role of their size, morphology and concentration in laser ablation and in impulse generation. Both commercial and green produced carbon nanoparticles are used for these experiments showing that, at least in the considered size range, the only parameter that affects laser ablation is the number density of absorption centers in the polymer matrix, and not size or morphology. This points the direction to follow in the development

of a polymeric material for LAP applications.

Some open problems and future works are presented in Chapter 7. Effects on impulse generated by irradiating multiple times the same region are discussed, showing opposite behaviours between metals and polymers, for which still there is not a clear explanation. Then experimental issues and some results on specific impulse measurements are presented, and difficulties related to this measurement in metals briefly discussed. Finally laser ablation in a confined geometry is considered as an attracting technique to enhance impulse generation. And some results on PVC are shown.

As a conclusion, main results obtained in this thesis are highlighted, and possible future research activities, developments and perspectives are discussed.

Chapter 1

Overview: New Space Economy and Laser Ablation Propulsion

Starting from early tests in 1950s and 1960s space has been increasingly exploited in many ways, producing a huge technological comeback in other fields on earth. Even if the development of new space applications always increased in time, in the last twenty years space market has grown at an increasing rate and changing radically from the past.

In the initial stages of its history exploitation of space was a matter only of an extremely limited number of countries and was conducted only by large public organizations. Recently however the situation changed, with the advent of many smaller private companies that allowed an almost worldwide spread of the space-related market, drastically increased[1, 2, 3, 4]. This new way to exploit space is nowadays called "New Space Economy".

Thanks to the availability of reliable data and knowledge acquired by the early space missions, these new private companies introduced new solutions and faster development strategies that are now deeply affecting this market. This movement is also receiving a great impulse because of the increasing number of space-related applications[1], in particular earth observation, with very important outcomes related to disaster monitoring and climate change[5]; and in telecommunications, with the deployment of megaconstellations of nanosatellites[6, 7]. Other activities include space exploration and research[8, 9] and even space tourism with companies like Blue Origin[10] and Virgin Galactic[11].

1.1 Space Debris

After all these years of activity in space, and in particular after its recent intensification, Earth orbit is now dangerously crowded. The problem of space debris is now becoming of primary importance: a very large numbers of dismissed spacecrafts, rocket stages and fragments still orbiting uncontrolled represents a serious threat for active missions, as presented in Figure(1.1). Moreover this problem may become even worst and uncontrollable in the future, as predicted by Kessler in 1978[12]: once density of debris increase enough it will give rise to a collisional cascade that will produce an even larger number of objects with smaller and smaller size, therefore impossible to track. It is then of primary importance not only to reduce the production of space debris, but also to actively remove them from orbit.

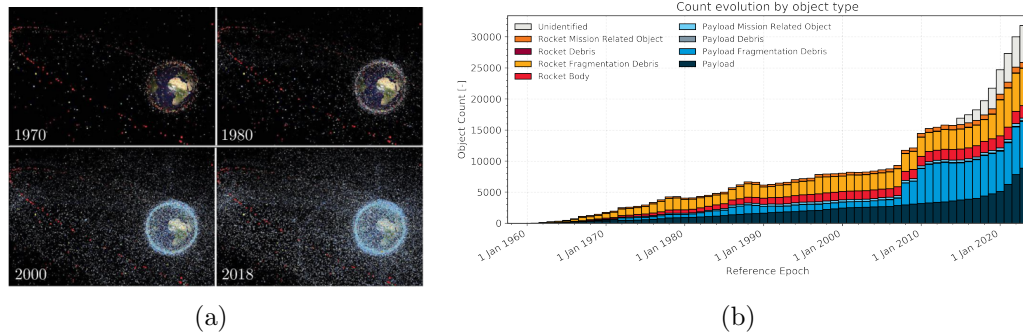


Figure 1.1: a) Distribution of space debris around earth in time. b) Count of the objects on orbit in time adapted from[13], the number of space debris is clearly increasing as visible in particular by two events: in 2007 a Chinese antisatellite test destroyed the Fenyngun-1C, while in 2009 there was an accidental collision between Kosmos2251 and Iridium 33[13].

While this problem is largely caused by the increased activity in space, the necessity to find a solution is pushing the development of many new systems to remove debris and to allow the re-entry of new satellites at the end of the mission[13].

Many different methods for the deorbiting of space debris have been proposed in these last years, however none of them has been tested up to now. The general strategy to achieve active debris removal is based on the idea

of moving them from their orbit, either slowing them down so that their altitude is reduced and they re-enter in the atmosphere and degrade because of drag, or by placing them in a so-called graveyard orbit where they don't represent a risk anymore. Many proposed ways to remove space debris then include a specifically designed spacecraft that mechanically grabs the debris by using mechanical arms, nets or similar technologies and then bring it in the defined new orbit[14, 15]. Of course the main problem in this kind of mission comes from the fact that the debris are usually rotating around a not known axis, in particular if they are produced by collisions, moreover also their mass and moment of inertia is not known so that the physical contact with the rescuing spacecraft becomes a serious problem.

Other proposed solutions avoid the mechanical contact of the rescuing spacecraft with the debris, and employ foams that stick around the object to remove in order to increase the effect of drag, if the starting orbit is sufficiently low[16], or also the use of solar sails to slow down the object helping its re-entry on Heart[15]. Even if no mechanical contact is needed in this case, these solution still require the use of a spacecraft that comes close to the debris and, in the case of solar sails, it also requires some control electronics to move the sail in order to act only as break and not accelerate the debris. Laser ablation propulsion gives an attracting solution to this problem, as discussed in the following of this chapter.

1.2 Nanosatellite propulsion

One of the driving forces for the rise of New Space Economy, that lead to the contribution in space activities of many private companies, is the diffusion of microelectronics.

First spacecrafts were developed by large institution, exploiting technologies developed for the single specific application: this of course implied long development times and high costs. The advent of microelectronics and in particular its diffusion on the large scale radically changed the development of new satellites. Size of satellites is now becoming smaller and smaller, so that is now preferable to have many of them with a few kg mass instead of a single satellite that may weight several tons. A categorization of satellites with respect to their mass was also made, as listed in table(1.2). Moreover the development of new electronic devices is now extremely fast, so that the majority of the instrumentation on board is commercial and not designed for

the specific mission, therefore development times and costs are reduced[4].

name	mass [kg]
Large satellite	>1000
Small satellite	500 to 1000
Mini-satellite	100 to 500
Micro-satellite	10 to 100
Nano-satellite	1 to 10
Pico-satellite	0.1 to 1
Femto-satellite	<0.1

Table 1.1: Categorization of satellites with respect to their mass.

More recently another important step in this direction was made by introducing standard shapes and masses for nanosatellites, by using the so called CubeSats. As their names says, CubeSats allow to build satellites of different sizes and masses by adding single cubic units (1U) with 10 cm side and 1 kg mass, as presented in Figure(1.2). CubeSats now are becoming very popular in many different missions[17, 18], helped by the fact that a standard shape allows to use also standard deployment systems again reducing costs. Similarly to what happened with the use of standard electronics, CubeSats pushed even further the private contribution to space market, with many companies now offering services based on these kind of spacecrafts. It can be

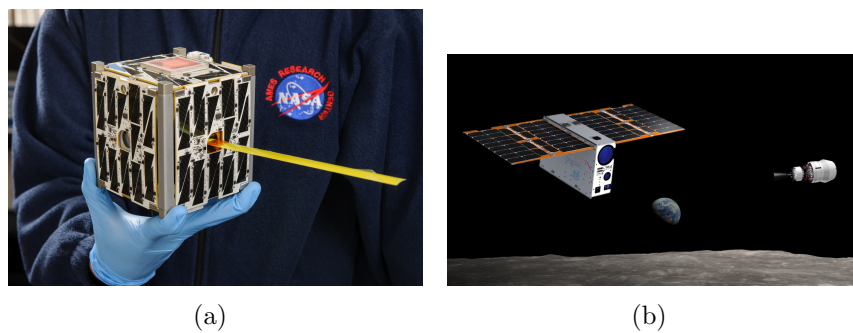


Figure 1.2: a) A 1U Cubesat [19]; b)The 6U Cubesat ArgoMoon, deployed in the mission Artemis 1 directed to the Moon[20]

easily imagined at this point that the kind of satellites employed is radically

changed in the last twenty years and, most of all, their number in orbit is enormously increased. Figure(1.3) shows the number of deployed satellites per year in the last years: it is clearly visible that their number is increasing, in particular in the case of nanosatellites, and an even larger number is expected in the following years.

This intense exploitation of space is now presenting some new problems,

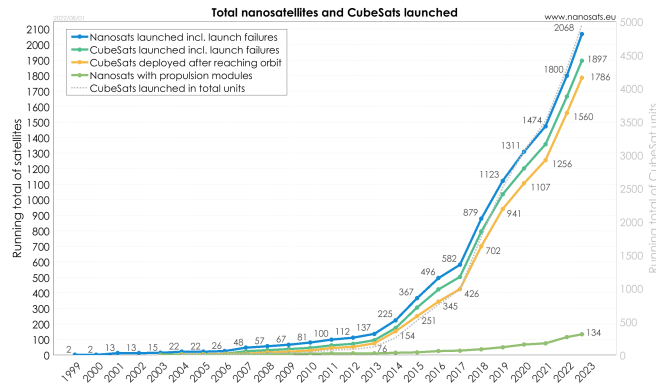


Figure 1.3: Total number of nanosatellites in orbit.

that have to be faced along with the space debris issue. First of all, while the development of nanosatellites is generally cheaper than the case of large satellites, launchers are still optimized to much heavier objects, so that they are usually deployed as secondary payloads to reduce costs, although other options can be to use present launchers to deploy many small satellites at the same time. Other fascinating solutions are now tested to create systems that allow many launches per day with a light payload, like SpinLaunch that exploits a rotating arm in vacuum to throw a rocket in the upper part of atmosphere drastically reducing fuel consumption and allowing multiple launches per day[21].

Another serious problem is then related to both space debris and the exploitation of small satellites for particular missions. By reducing the size of the satellite, and in particular by standardizing its mass and shape, strong limitations are imposed to power storage and propulsion system, so that at the present time many nanosatellites don't have any kind of thruster. Without the possibility to correct orbit and attitude of a satellite, missions can be very limited: many nanosatellites work in low earth orbit(LEO) at around

500 km of altitude where atmospheric drag still plays a role, so that it re-enters on earth after a short time. Moreover one of the great advantages of using small satellites is the possibility to create large constellations that offer good coverage of all Earth. However, to achieve that, orbit correction is needed to maintain relative positions between the satellites.

Finally the propulsion problem is also related to the space debris one, since now to avoid a further increase of objects in orbit a new rule has been introduced that requires that each satellite must re-enter on Earth after 25 years from the end of the mission[13]. Also small satellites then must have a system to allow their reenter after this period of time.

To solve the problem of propulsion systems for small satellites new thrusters are being developed, in order to reduce size and power and fuel consumption: this is another field in which laser ablation propulsion offers a very attractive solution.

Intense research activity has been done in the last few years in order to develop new propulsion systems for nanosatellites, or to miniaturize existing ones. A great step forward in this direction came with the introduction of so called Micro Electro Mechanical Systems (MEMS)[22]: new fabrication techniques that allow an extreme size reduction of common propulsion systems. The main idea is therefore to miniaturize some of the existing propulsion systems, based on the combustion of a propellant and on the acceleration of products through a nozzle. The most main micropropulsion systems under: development are the following

- **Resistojet:** A resistance is used to heat a liquid or solid propellant that becomes gaseous and consequently is accelerated through a nozzle. The main propellant considered for this kind of thruster is water, due to its safety and good performances[23], with the main drawback represented by its high heat of vaporization. This kind of devices requires optimized design and fabrication to ensure efficient heating fuel, moreover propellant storage represents another challenge.
- **Cold-gas microthrusters:** In this case thrust is generated by accelerating a pressurized gas through a nozzle. Propellant can be stored in gaseous, liquid or solid phase, in the last two cases of course gas has to be generated before ejection. Due to its simplicity this kind of thrusters is at an advanced state of development, however some problems are still present related to leakage in fuel storage, that has to be

reduced to a minimum because waiting times for nanosatellites can be very long being secondary payload.

- **Solid propellant microthrusters:** A small amount of solid propellant is contained in a chamber, along with an igniter that initiate combustion, thrust is then generated by accelerating products through a nozzle. The main advantage of this kind of thrusters is that they are very compact, so that many of them can be put in a nanosatellite, however some problems are still present in obtaining complete combustion of propellant in the chamber. The main drawback of this system is that they cannot be controlled after ignition and, in order to use them more than once, several stages have to be used, increasing the complexity of the system.
- **Liquid propellant microthrusters:** In this case a liquid propellant reacts with a catalyst producing hot gas that is accelerated by a nozzle. This device then consists of a propellant inlet that delivers it in a catalyst chamber through some valves, and by a nozzle. The main problem with such a system is that it still requires toxic and flammable fuels like hydrazine, even if other propellants are being tested[24].
- **Electrospray thrusters:** An ionic liquid in a capillary is accelerated with an electric potential. Above a threshold potential the liquid at the tip of the capillary forms a cone, emitting either droplets or single ions. Thousands of emitters per thruster can be used, making it a promising propulsion system that allows finely controlled thrust.

There are then other already tested propulsion systems that showed interesting performances and that now are tried to be miniaturized. In these cases it is not possible to use MEMS so that, also because of other physical limitations, they are still difficult to apply to nanosatellites.

- **Pulsed Plasma Thruster (PPT):** A capacitor generates a discharge that ablates the solid propellant, usually PTFE (Teflon), which is also partially ionized. Ions are accelerated by self induced Lorentz forces, while neutrals are heated and accelerated by the pressure gradient generated by the ablation process[25]. This kind of thrusters generate impulse bits rather than a continuous force on the spacecraft, so the main limit in this case is represented by the time needed to charge the capacitor.

- **Ion thrusters:** A gas propellant is ionized in a chamber by using hollow cathode electron emission, microwave heating or radio frequency; the produced plasma is then accelerated by a grid and neutralized at the exit of the thruster by using a separate electron source. Such systems proved to be efficient and reliable[26], however miniaturization is limited by the mean free path of electron in the ionization chamber that may prevent plasma formation.
- **Hall thrusters:** Electrons generated by a hollow cathode are accelerated in a chamber where a radial magnetic field is present, so that Hall currents are generated. By injecting an inert gas like Xenon in this chamber a plasma is generated because of this currents and is then accelerated like in a ion thruster. This working principle allows an easier miniaturization of the thruster, promising attractive development for the future.
- **Solar Sails:** The last propulsion system that must be considered here is the one based on solar sails[27]. This technology exploits the radiation pressure generated by the reflection of photons to generate thrust. In this case of course miniaturization directly affects thrust generation so it is not possible. However this technique presents the attracting advantage of not needing any fuel or power storage. Its main problems on the other hand are related to the difficulty of deploying the sail in space and to the impossibility to start or stop thrust at any desired time.
Even if solar sails cannot be strictly defined as micropropulsion systems, this system must be considered in this overview since they share many points in common with LAP.

1.3 Laser Ablation Propulsion

When a material is irradiated by intense laser pulse undergoes to extreme physical or chemical conditions that lead to modifications in its structure and to mass ejection from the irradiated region, mainly because of the high temperature attained at the surface. This phenomenon is exploited in many applications like etching[28], micromachining[29], and materials production[30, 31] and is defined as laser ablation.

Despite the quantity of ejected mass (m_e) is in general small, it leaves the

irradiated region with extremely high velocities (v_e). As shown in Figure(1.4) momentum conservation can be applied to such a system so that a measurable net thrust is generated on the ablated material.

$$J = m_e v_e \quad (1.1)$$

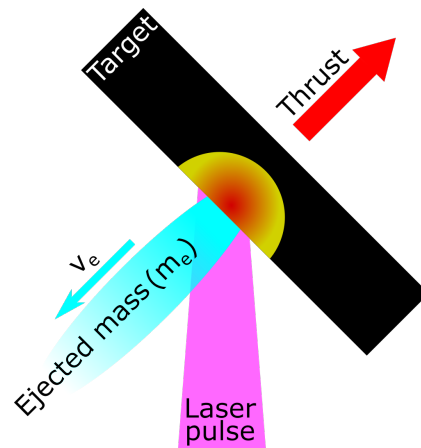


Figure 1.4: Scheme of impulse generation during laser ablation.

Laser ablation propulsion [32] then exploits the material on the spacecraft as a fuel, and it doesn't need any other equipment on board. This means that in principle thrust can be generated on any object even if it is situated at very large distances from the laser, since there's no need of a power source for propulsion in the spacecraft. This is an extremely attractive advantage when looking for possible solutions for space debris removal or propulsion for nanosatellites.

Starting from 1970's, when the first ideas of laser powered rockets were proposed, some research has been conducted on this, with several theoretical models and experimental activities[33, 34]. Interest in laser propulsion however rapidly grew in the last twenty years due to the advent of the New Space Economy. In particular the large scale employment of smaller and smaller satellites and the urgency of the space debris problem, together with the development of increasingly powerful lasers, is now offering a large number of possible applications for Laser Ablation Propulsion.

When comparing LAP with the previously described strategies for active debris removal it appears clearly that its main advantage is the possibility to act on the debris from large distances, so that all the problems related to bring a satellite close to an object with no clear motion can be avoided. At the present time LAP is the only technique that allows to do this and different works tried to simulate the deorbiting of a given debris[35, 36], by using the generated thrust to slow down the object and help its re entering on Earth, as shown in Figure(1.5). Considering space debris of course it is not

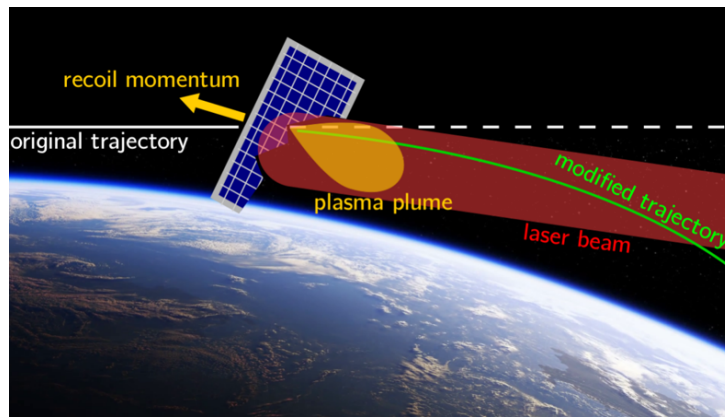


Figure 1.5: Deorbiting of a space debris using LAP.

possible to optimize the target material to increase the generated impulse, since the one composing the object must be used. Research in this field is therefore moving towards the characterization of impulse generated by the most common materials present on orbit, for instance aluminum or silicon. In particular it is important to understand in these cases how generated impulse changes with multiple laser pulses in the same region also considering different repetition rates that result in different thermal loads on the material.

While in the case of debris the main advantage of LAP with respect to other solution is logistic, the comparison with other propulsion systems lies on more deeper grounds. All space propulsion systems used nowadays, being they chemical or electrical, generate thrust by accelerating some mass in the direction opposite to motion, that is, they exploit momentum conservation. In other words the total force F acting on the system spacecraft+ejecta is always zero. Considering the force acting on the spacecraft as it accelerates

it is possible to write

$$F = M \frac{dv}{dt} \quad (1.2)$$

since momentum is conserved and the total force on the spacecraft is zero it must also be that an opposite force is applied on the ejected mass

$$F = -v_e \frac{dM}{dt} \quad (1.3)$$

Therefore equating eq.(1.2) and eq.(1.3) gives

$$M \frac{dv}{dt} = -v_e \frac{dM}{dt} \quad (1.4)$$

integration of eq(1.4) leads to the so called Tsiolkovsky rocket equation that describes the fraction of ejected mass over the total initial mass of the spacecraft to increase its velocity by Δv , given the velocity of the ejected material v_e .

$$\frac{M_e}{M_0} = 1 - \exp\left(-\frac{v_e}{\Delta v}\right) \quad (1.5)$$

In order to reduce the fuel mass that has to be carried on board its ejection velocity must then be increased. Increasing the ejection velocity becomes particularly relevant in the case of small spacecrafts due to the strict mass and size limitations.

As an example Figure(1.6) shows the value of M_e/M_0 for some commonly used thrusters, not only for small spacecrafts. Common chemical propulsion systems commonly used as launchers from earth generate very high thrust, however the ejection velocity of the combustion products is much lower than the desired $\Delta v \simeq 10 \text{ km s}^{-1}$ to reach orbit, therefore almost all of the mass of the spacecraft is composed by fuel.

A much different situation is observed in the case of electrical propulsion systems where, being thrust generated by accelerating ions, ejection velocity is much higher. It must be noted however that thrust generated by electrical propulsion systems is much lower than that needed to lift an object on heart, so that they are not used as launchers but as thrusters to control satellites. As a consequence there's no need to reach such high Δv , but much smaller values of order 100 m s^{-1} are sufficient to complete a mission in low Earth orbit or around Moon. (LEO)[37]. Δv of several km s^{-1} however may be also necessary for satellites to accomplish interplanetary missions[25]. In any

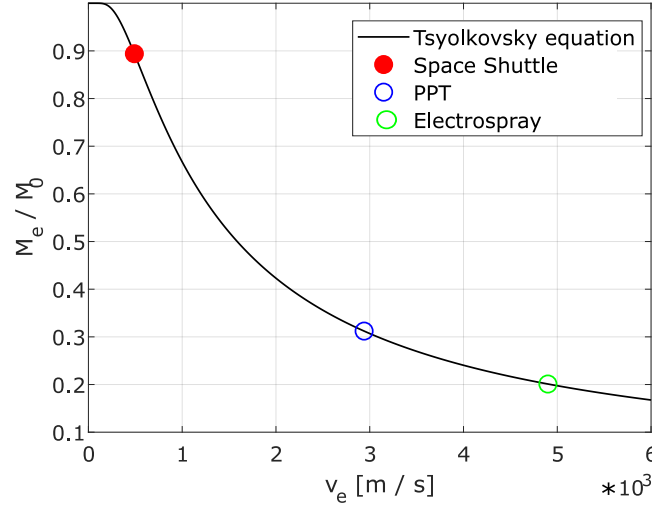


Figure 1.6: Ratio of fuel mass over total spacecraft mass to reach $\Delta v \simeq 10 \text{ km s}^{-1}$, needed to reach Earth orbit. Full circle represents the result for a typical launcher, the Space Shuttle, for which this requirement is true. Open circles show the results obtained for electrical propulsion systems used to control satellites, that usually require much lower Δv

case Tsiolkovsky equation and Figure(1.6) offer a clear picture of the drastic improvement in fuel consumption that can be achieved by increasing exhaust velocity.

A typical parameter used to characterize thrusters from this point of view is the so called *specific impulse*, that express v_e :

$$I_{sp} = \frac{\text{generated impulse}}{\text{expelled weight}} = \frac{m_e v_e}{m_e g} \quad (1.6)$$

From its definition it is clear that I_{sp} represents the efficiency in impulse generation on terms of mass consumption. A thruster with a high I_{sp} value therefore allows to reduce the mass of the on board fuel to accomplish a specific mission. Figure(1.7) shows typical I_{sp} intervals for some common types of space thrusters. LAP showed very attractive results from this point of view, especially in the case of metals that showed I_{sp} values up to several thousands, comparable to electric propulsion systems.

If on one hand electric propulsion systems allow to reduce mass consumption with high I_{sp} values, the main drawback is that this requires high power; this is a problem for nanosatellites where on board power is limited to a few W, in the case of CubeSats power is usually limited to 3 W per unit[22].

All this discussion directly comes as a consequence of momentum conservation, the principle at the base of all propulsion techniques. A possible way to deal with limitations imposed by physics consists on separating power storage or generation from the nanosatellites it happens in the case of LAP or solar sails.

These two techniques are then reasonably the most appropriate to be used as propulsion systems in case of nanosatellites, but a further more quantitative comparison is possible considering the thrust they can generate and in particular the energy efficiency of this process. This last parameter is an important figure of merit in LAP, and is called *laser-impulse coupling coefficient*, C_m , defined as

$$C_m = \frac{\text{generated impulse}}{\text{laser pulse energy}} \quad (1.7)$$

Even if C_m is commonly defined for laser-powered systems, it allows an interesting comparison between LAP and solar sails[38].

In the case of solar sails thrust is generated by radiation pressure, caused by the reflection of photons on the sail. Considering an ideal case in which photons are impinging normally to the sail and are perfectly reflected by it, the variation in momentum of the reflected photon will be $\Delta p = 2p$ with $p = E/c$ and E the energy of the photon. Coupling coefficient can then be computed as

$$C_m = \frac{2p}{E} = \frac{2}{c} = 6.76.7 \text{ nN W}^{-1} \quad (1.8)$$

In the case of LAP on the other hand C_m depends on the irradiated material and on other parameters, as it will be discussed in the following chapter, but can reach more than $1000 \mu\text{N W}^{-1}$ [32]: much larger values compared to solar sails. Laser ablation is then much more effective in generating a mechanical impulse than the simple reflection of photons; moreover it also allows to tune the magnitude of the generated impulse by changing laser energy density, as also discussed in the following of the thesis.

Finally impulse generated by LAP can be compared with other proposed micropropulsion techniques, whose performances are presented in Figure(1.7).

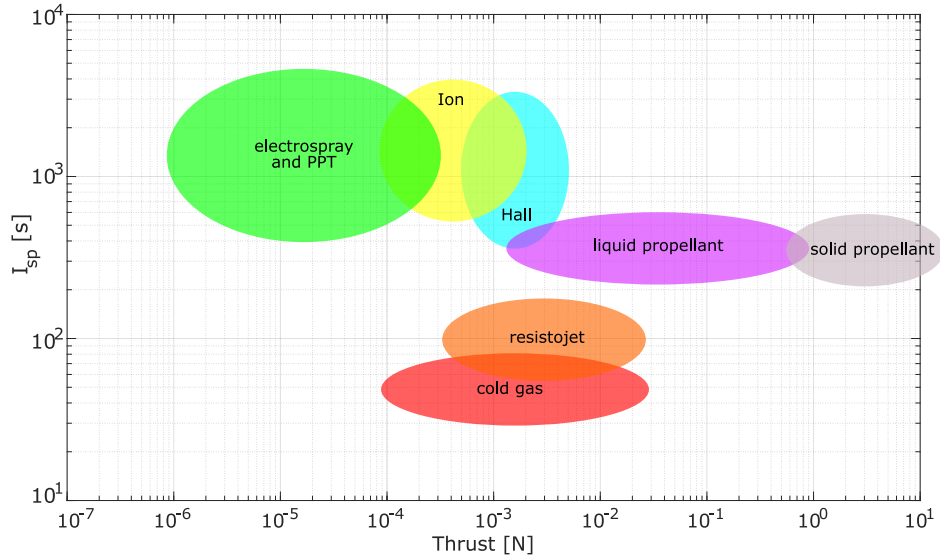


Figure 1.7: Specific impulse and thrust generated by some common micro-propulsion systems[22, 39, 25, 40, 41, 42]

As an order of magnitude estimation it is possible to say that generally systems like resistojets and cold gas thruster generate thrusts in the order of hundreds of μN up to several mN with I_{sp} values usually lower than 100s. Much higher thrust in the order of N can be obtained in the case of solid and liquid propellant thrusters, again with I_{sp} of hundreds of s. Strictly electrical propulsion systems on the other hand generate lower thrust, but since ions are accelerated I_{sp} higher than 1000s can be obtained.

A direct comparison of thrust generated by LAP is tricky, because in this last case a very short impulse is applied rather than a continuous force; it is possible however to make an estimate of the force applied on the irradiated material by assuming a reasonable impulse duration.

Depending on the target material and laser parameters mass ejection during laser ablation can last up to some tens of μs , as discussed more in detail in the next chapter. Since generally mechanical impulses in the range of 10 nN s up to more than 100 μN s are generated in LAP, this means that a thrust in the mN to N regime are obtained for very short times. Average thrust can also be computed as the product of generated impulse and laser pulse repetition frequency. Considering that nowadays repetition rates much higher than kHz are possible, average thrust of the order of mN is easily achievable;

and this is possible in principle without affecting I_{sp} .

Specific impulse on the other hand can be compared directly, since depending on the material it can be in the order of 100s in the case of polymers up to several thousands s for metals[43].

This comparison allows to highlight the main advantages of LAP with respect to the other techniques here considered. As previously discussed LAP is particularly attractive because it does not need power source and other components on board. From a more quantitative point of view it is possible to say that, while the force applied to the spacecraft is similar to the other propulsion systems, it is applied for extremely short time periods and with easily variable intensities, so that it can generate both very small or high variation in the velocity of the spacecraft. Moreover this can be done with very high specific impulse, so that fuel mass on board is reduced or, alternatively, longer missions are possible.

To sum up this chapter, LAP represents a really promising solution to some of the problems that are now arising with the much more intense space activity brought up by the New Space Economy, like active debris removal and nanostellite propulsion. In order to exploit LAP for these applications is therefore of fundamental importance to understand how impulse generation can be related to the possible ablation mechanism and laser and material properties.

Different works investigated many materials in order to find the best propulsion performances, often with the strategy to perform a direct comparison between them. Even if this approach allows to make some general conclusions, a simple comparison between materials is usually very difficult from the point of view of laser ablation and impulse generation because of the many optical and thermodynamical properties involved.

The goal of this work is to investigate how a material can be designed to be used as a fuel for LAP, so obtained results concern the application of this technique for nanosatellite propulsion. Many considerations however can be made also on space debris removal. In order to do this it becomes of fundamental importance to isolate material properties that mainly affect impulse generation. A large part of this thesis is therefore devoted to the study of laser ablation of poly(vinyl chloride) (PVC), considered a promising LAP material, in which single properties are selectively changed in order to allow a coherent observation of their role in impulse generation.

Bibliography

- [1] OECD. *The Space Economy in Figures*. 2019. doi: <https://doi.org/https://doi.org/10.1787/c5996201-en>. URL <https://www.oecd-ilibrary.org/content/publication/c5996201-en>.
- [2] Agenzia Spaziale Italiana. La nuova frontiera dell'economia oltre l'atmosfera terrestre, 2021. URL <https://www.asi.it/space-economy/>.
- [3] Giovanni Rossettini, Luca; Sylos Labini. "la new space economy italiana tra scienza, tecnologia e industria". *Energia ambiente e innovazione*, 2021.
- [4] Martin N. Sweeting. Modern small satellites-changing the economics of space. *Proceedings of the IEEE*, 106(3):343–361, 2018. doi: 10.1109/JPROC.2018.2806218.
- [5] Joseph R. Kopacz, Roman Herschitz, and Jason Roney. Small satellites an overview and assessment. *Acta Astronautica*, 170:93–105, 2020. ISSN 0094-5765. doi: <https://doi.org/10.1016/j.actaastro.2020.01.034>.
- [6] Giacomo Curzi, Dario Modenini, and Paolo Tortora. Large constellations of small satellites: A survey of near future challenges and missions. *Aerospace*, 7(9), 2020. ISSN 2226-4310. doi: 10.3390/aerospace7090133. URL <https://www.mdpi.com/2226-4310/7/9/133>.
- [7] Salvo Marcuccio, Silvia Ullo, Marco Carminati, and Olfa Kanoun. Smaller satellites, larger constellations: Trends and design issues for earth observation systems. *IEEE Aerospace and Electronic Systems Magazine*, 34(10):50–59, 2019. doi: 10.1109/MAES.2019.2928612.
- [8] Stephen Serjeant, Martin Elvis, and Giovanna Tinetti. The future of astronomy with small satellites. *Nature Astronomy*, 4(11):1031–1038, 2020.
- [9] Robyn M. Millan, Rudolf von Steiger, Meir Ariel, Sergey Bartalev, Maurice Borgeaud, Stefano Campagnola, Julie C. Castillo-Rogez, René Fléron, Volker Gass, Anna Gregorio, David M. Klumpar, Bhavya Lal, Malcolm Macdonald, Jong Uk Park, V. Sambasiva Rao, Klaus Schilling,

- Graeme Stephens, Alan M. Title, and Ji Wu. Small satellites for space science: A cospar scientific roadmap. *Advances in Space Research*, 64(8):1466–1517, 2019. ISSN 0273-1177. doi: <https://doi.org/10.1016/j.asr.2019.07.035>. URL <https://www.sciencedirect.com/science/article/pii/S0273117719305411>.
- [10] Blue origin webpage. URL <https://www.blueorigin.com/>.
- [11] Virgin galactic webpage. URL <https://www.virgingalactic.com/>.
- [12] Donald J. Kessler and Burton G. Cour-Palais. Collision frequency of artificial satellites: The creation of a debris belt. *Journal of Geophysical Research: Space Physics*, 83(A6):2637–2646, 1978. doi: <https://doi.org/10.1029/JA083iA06p02637>.
- [13] Esa webpage. URL https://www.esa.int/Space_Safety/Space_Debris/Mitigating_space_debris_generation.
- [14] C. Priyant Mark and Surekha Kamath. Review of active space debris removal methods. *Space Policy*, 47:194–206, 2019. ISSN 0265-9646. doi: <https://doi.org/10.1016/j.spacepol.2018.12.005>.
- [15] Minghe Shan, Jian Guo, and Eberhard Gill. Review and comparison of active space debris capturing and removal methods. *Progress in Aerospace Sciences*, 80:18–32, 2016. ISSN 0376-0421. doi: <https://doi.org/10.1016/j.paerosci.2015.11.001>.
- [16] Lourens Visagie, Vaios Lappas, and Sven Erb. Drag sails for space debris mitigation. *Acta Astronautica*, 109:65–75, 2015. ISSN 0094-5765. doi: <https://doi.org/10.1016/j.actaastro.2014.12.013>.
- [17] Chantal Cappelletti and Daniel Robson. Cubesat missions and applications. In Chantal Cappelletti, Simone Battistini, and Benjamin K. Malphrus, editors, *Cubesat Handbook*, pages 53–65. Academic Press, 2021. ISBN 978-0-12-817884-3. doi: <https://doi.org/10.1016/B978-0-12-817884-3.00002-3>.
- [18] Armen Poghosyan and Alessandro Golkar. Cubesat evolution: Analyzing cubesat capabilities for conducting science missions. *Progress in Aerospace Sciences*, 88:59–83, 2017. ISSN 0376-0421. doi: <https://doi.org/10.1016/j.paerosci.2016.11.002>.

- [19] National Aeronautics and Space Administration (NASA) website. URL https://www.nasa.gov/mission_pages/station/research/news/cubesats_possibilities.
- [20] Agenzia Spaziale Italiana, 2021. URL <https://www.asi.it/2021/05/con-argomoon-litalia-vola-verso-la-luna/>.
- [21] Spinlaunch webpage. URL <https://www.spinlaunch.com/>.
- [22] Marsil A.C. Silva, Daduá C. Guerrieri, Angelo Cervone, and Eberhard Gill. A review of mems micropropulsion technologies for cubesats and pocketqubes. *Acta Astronautica*, 143:234–243, 2018. ISSN 0094-5765. doi: <https://doi.org/10.1016/j.actaastro.2017.11.049>.
- [23] R. H. Lee, A. M. Bauer, M. D. Killingsworth, T. C. Lilly, J. A. Duncan, and A. D. Ketsdever. Free-molecule-microresistojet performance using water propellant for nanosatellite applications. *Journal of Spacecraft and Rockets*, 45(2):264–269, 2008. doi: 10.2514/1.32341.
- [24] A. P. London, A. H. Epstein, and J. L. Kerrebrock. High-pressure bipropellant microrocket engine. *Journal of Propulsion and Power*, 17(4):780–787, 2001. doi: 10.2514/2.5833.
- [25] Kristina Lemmer. Propulsion for cubesats. *Acta Astronautica*, 134:231–243, 2017. ISSN 0094-5765. doi: <https://doi.org/10.1016/j.actaastro.2017.01.048>.
- [26] John R. Brophy. Nasa’s deep space 1 ion engine (plenary). *Review of Scientific Instruments*, 73(2 II):1071, 2002. doi: 10.1063/1.1432470.
- [27] Michael Souder and Matthew West. *Solar Sail Technology for Nanosatellites*. 2008. doi: 10.2514/6.2008-7078.
- [28] V. Srinivasan, Mark A. Smrtic, and S. V. Babu. Excimer laser etching of polymers. *Journal of Applied Physics*, 59(11):3861–3867, 1986. doi: 10.1063/1.336728.
- [29] Rafael R Gattass and Eric Mazur. Femtosecond laser micromachining in transparent materials. *Nature photonics*, 2(4):219–225, 2008.

- [30] Luca Basso, Nicola Bazzanella, Massimo Cazzanelli, and Antonio Miotello. On the route towards a facile fluorescent nanodiamonds laser-synthesis. *Carbon*, 153:148–155, 2019.
- [31] F Gorrini, M Cazzanelli, N Bazzanella, R Edla, M Gemmi, V Cappello, J David, C Dorigoni, A Bifone, and A Miotello. On the thermodynamic path enabling a room-temperature, laser-assisted graphite to nanodiamond transformation. *Scientific Reports*, 6(1):1–9, 2016.
- [32] Claude Phipps, Mitat Birkan, Willy Bohn, Hans-Albert Eckel, Hideyuki Horisawa, Thomas Lippert, Max Michaelis, Yuri Rezunkov, Akihiro Sasoh, Wolfgang Schall, Stefan Scharring, and John Sinko. Review: Laser-ablation propulsion. *Journal of Propulsion and Power*, 26(4):609–637, 2010. doi: 10.2514/1.43733.
- [33] A. PIRRI and R. WEISS. *Laser propulsion*. doi: 10.2514/6.1972-719.
- [34] C. R. Phipps, T. P. Turner, R. F. Harrison, G. W. York, W. Z. Osborne, G. K. Anderson, X. F. Corlis, L. C. Haynes, H. S. Steele, K. C. Spicochi, and T. R. King. Impulse coupling to targets in vacuum by krf, hf, and co2 single-pulse lasers. *Journal of Applied Physics*, 64(3):1083–1096, 1988. doi: 10.1063/1.341867.
- [35] Claude R. Phipps. A laser-optical system to re-enter or lower low earth orbit space debris. *Acta Astronautica*, 93:418–429, 2014. ISSN 0094-5765. doi: <https://doi.org/10.1016/j.actaastro.2013.07.031>.
- [36] Claude R. Phipps. L’adroit - a spaceborne ultraviolet laser system for space debris clearing. *Acta Astronautica*, 104(1):243–255, 2014. ISSN 0094-5765. doi: <https://doi.org/10.1016/j.actaastro.2014.08.007>.
- [37] A. Cervone, F. Topputo, S. Speretta, A. Menicucci, E. Turan, P. Di Lizia, M. Massari, V. Franzese, C. Giordano, G. Merisio, D. Labate, G. Pilato, E. Costa, E. Bertels, A. Thorvaldsen, A. Kukharenska, J. Vennekens, and R. Walker. Lumio: A cubesat for observing and characterizing micro-meteoroid impacts on the lunar far side. *Acta Astronautica*, 195:309–317, 2022. ISSN 0094-5765. doi: <https://doi.org/10.1016/j.actaastro.2022.03.032>.

- [38] Claude R. Phipps. *Laser Ablation Propulsion and Its Applications in Space*, pages 217–246. Springer International Publishing, 2018. ISBN 978-3-319-96845-2. doi: 10.1007/978-3-319-96845-2_8.
- [39] Igor Levchenko, Kateryna Bazaka, Yongjie Ding, Yevgeny Raitses, Stéphane Mazouffre, Torsten Henning, Peter J. Klar, Shunjiro Shinohara, Jochen Schein, Laurent Garrigues, Minkwan Kim, Dan Lev, Francesco Taccogna, Rod W. Boswell, Christine Charles, Hiroyuki Koizumi, Yan Shen, Carsten Scharlemann, Michael Keidar, and Shuyan Xu. Space micropropulsion systems for cubesats and small satellites: From proximate targets to furthestmost frontiers. *Applied Physics Reviews*, 5(1):011104, 2018. doi: 10.1063/1.5007734.
- [40] Hui Liu, Xiang Niu, Ming Zeng, Shangsheng Wang, Kai Cui, and Daren Yu. Review of micro propulsion technology for space gravitational waves detection. *Acta Astronautica*, 193:496–510, 2022. ISSN 0094-5765. doi: <https://doi.org/10.1016/j.actaastro.2022.01.043>.
- [41] W.P. Wright and P. Ferrer. Electric micropropulsion systems. *Progress in Aerospace Sciences*, 74:48–61, 2015. ISSN 0376-0421. doi: <https://doi.org/10.1016/j.paerosci.2014.10.003>.
- [42] Akshay Reddy Tummala and Atri Dutta. An overview of cube-satellite propulsion technologies and trends. *Aerospace*, 4(4), 2017. ISSN 2226-4310. doi: 10.3390/aerospace4040058.
- [43] C. Phipps, J. Luke, D. Funk, D. Moore, J. Glowonia, and T. Lippert. Laser impulse coupling at 130fs. *Applied Surface Science*, 252(13):4838–4844, 2006. ISSN 0169-4332. doi: <https://doi.org/10.1016/j.apsusc.2005.07.079>. Proceedings of the European Materials Research society 2005 - Symposium-J: Advances in Laser and Lamp Processing of Functional Materials.

Chapter 2

Laser Ablation

When a short and sufficiently intense laser pulse impinges on a material mass removal is observed from the irradiated region, generally with the formation of a plume. After laser irradiation either a crater or surface modifications are observed on the irradiated region, offering some hints in the investigation of the interaction of the laser with the material and the involved mechanisms. The principal parameter in laser ablation is the energy density deposited in the irradiated region, called fluence. This is defined as

$$F = \frac{E}{\text{irradiated area}} \quad (2.1)$$

with E the laser energy deposited on the target. Commonly used fluences range from few mJ/cm² up to tens of J/cm² but also much higher values are possible. To obtain such fluence values high power pulsed lasers are employed with wavelengths both in the IR spectrum, obtained with solid state lasers like Nd:YAG, or in the UV spectrum by using excimer lasers or harmonics of IR lasers, that also allow some visible wavelengths. Similarly, also different pulse durations are possible, that range from μ s down to fs.

To obtain an explanation of laser ablation it is important to understand how laser-material interaction leads to the observed mass removal and to the other possible modifications. This chapter then will discuss how ablation proceeds depending on material and laser parameters like energy density, wavelength and pulse duration. All these parameters play an extremely important role in determining mechanisms and thermodynamic conditions involved, that in turn affect the condition of the ablated material and the morphology of the crater left.

All this discussion is finally related to the generation of a mechanical impulse during mass ejection. In fact, depending on the quantity of mass ejected, its velocity and its physical state, that can be gaseous liquid or solid, the obtained propulsion performances change noticeably so that it becomes fundamental for the development of LAP materials.

2.1 Metals

Metals are the most studied category of materials in laser ablation and their mass removal mechanisms are already well defined. [1].

A description of laser ablation of metals can be roughly divided in two steps, that depending on laser pulse duration may occur almost simultaneously. The first step is the interaction of the laser pulse with the material, that leads to an extremely fast heating; the second step consists in phase transitions that occur because of the high temperature reached, that result in different mass ejection mechanisms. These steps are described in the following sections.

2.1.1 Laser-material interaction and heating

Laser interaction with a metal always brings to a fast temperature increase, however, depending on laser intensity and pulse duration very different outcomes are possible. When the laser pulse hits the surface of a metal, a part of photons is reflected, the rest is absorbed by free electrons [2] in a depth of the order of tens of nm[3]. Absorbed laser energy heats up these electrons that consequently thermalize with the lattice increasing its temperature with a typical time $\tau_e \sim 0.1 - 1$ ps [4].

The electron-lattice relaxation time sets a timescale with which the laser pulse duration must be compared. In the case of pulse duration much longer than τ_e temperature profile $T(x, t)$ in the material can be modeled by considering a heat diffusion equation[3, 5, 6]

$$c_p \frac{\partial T(x, t)}{\partial t} = \frac{\partial}{\partial x} \left[K(x, t) \frac{\partial T(x, t)}{\partial x} \right] + S(x, t) \quad (2.2)$$

with c_p the specific heat of the material, K the thermal conductivity, ρ the mass density and $S(x, t)$ the heat source term that in the case of laser

ablation is the laser pulse and is usually described according to Lambert-Beer theory[7, 6]

$$S(x, t) = \alpha I(t) \exp(-\alpha x) \quad (2.3)$$

where $I(t)$ is laser intensity and α the absorption coefficient of the metal. Two points must be noted in this approach. As first, equation (2.2) is here presented in only one dimension while heat diffusion should be described in principle in three dimensions. However, if the size of the irradiated region is much larger than the typical heat diffusion length, border effects can be neglected and the solution in one dimension is a good approximation[3]. As discussed in the following chapters, the experimental work presented in this thesis exploits large laser spot sizes of the order of few mm while typical heat diffusion lengths in metals are of the order of 0.1 - 1 μm for the timescales of interest (~ 100 ns). The 1D picture here presented is therefore a good description for the experimental conditions used for this work.

The second point to consider is the temperature dependence of the physical parameters involved in equations (2.2) and (2.3). Because of the extreme energy intensities reached by pulsed lasers, that can be also much higher than GW cm^{-2} , heating rates of the order of $10^{12} - 10^{14} \text{ K s}^{-1}$ are reached so that temperature dependence can't be neglected[8]. This of course represents an obstacle to overcome to perform calculations, in particular because often temperature dependence is not known for the involved parameters.

The heating process just described is the one that will be considered in the following of this work, since a laser with a pulse duration of 20 ns is used, as described more in detail in the next chapter.

If laser pulse duration is in the fs range, electron-lattice relaxation occurs after the end of irradiation, so that all of the energy of the photons is absorbed by free electrons and is then deposited on the lattice after the end of the laser pulse. This means that in the time interval between the end of the laser pulse and τ_e electrons and lattice have two different temperatures and are therefore in a non-equilibrium state. To describe this situation a so called two temperature model is considered[9]

$$\begin{aligned} c_{p,e} \frac{\partial T_e(x, t)}{\partial t} &= \frac{\partial}{\partial x} \left[K_e(x, t) \frac{\partial T_e(x, t)}{\partial x} \right] - G(T_e)(T_e - T_l) + S(x, t) \\ c_{p,l} \frac{\partial T_l(x, t)}{\partial t} &= \frac{\partial}{\partial x} \left[K_l(x, t) \frac{\partial T_l(x, t)}{\partial x} \right] + G(T_e)(T_e - T_l) \end{aligned} \quad (2.4)$$

In equation (2.4) it is possible to note that two heat diffusion equations are considered, one for electrons and one for the lattice. The heat source term is applied to the heat equation for electrons, since they are responsible for heat absorption, moreover a heat transfer coefficient $G(T_e)(T_e - T_l)$ is also inserted in this equation as a loss term, representing thermalization of electrons with the lattice. This heat transfer term couples the equations for electrons and lattice, being inserted in the second one as a source term.

2.1.2 Mass ejection mechanisms

The laser induced heating just described allows to reach temperatures that can be also much higher than the boiling temperature of the metal target. This of course means that the irradiated region under such extreme thermodynamic conditions undergoes different phase transitions. As a consequence some mass can be ejected in the form of single atoms, either neutral or ionized, or as liquid nanodroplets, depending on laser fluence.

Vaporization

A vapour phase always exists in the vicinity of the metal surface at any value of temperature and ambient pressure, however this is usually negligible in normal ambient conditions. As described, during laser irradiation temperature rapidly increases to very high values, so that vaporization of the metal surface becomes much faster and vapour partial pressure increases according to Clausius-Clapeyron equation[10]:

$$\frac{dp(T_s)}{dT_s} = \frac{l}{T_s \Delta V} \quad (2.5)$$

where l is the latent heat of vaporization and ΔV the change in specific volume between the liquid and the vapour phase.

This generated vapour then leaves the irradiated surface and expands into vacuum with a process that can be modeled in two main steps, namely the formation of a so called Knudsen layer followed by an unsteady adiabatic expansion[11]. Immediately after leaving the surface the velocity of vapour atoms in the direction normal to the surface points only outward, while components parallel to surface can be present at all angles. Since this mass ejection

tion is thermally activated, velocities can be described in principle through a Maxwellian distribution[11]

$$f_s^+ \propto \exp \left[-\frac{2E_I + m(v_x^2 + v_y^2 + v_z^2)}{2k_B T_S} \right] \quad (2.6)$$

$$v_x > 0; -\infty \leq v_y, v_z \leq \infty$$

This region, defined as Knudsen layer develops close to surface in the space needed for atoms to make 2-3 collisions with each other, that is usually in the order of few nm[11, 12]. Beyond this region, due to the multiple collisions, the motion of vapour atoms changes from singular ballistic motion to a collective flow, therefore also a velocity component directed normally towards the surface appear and a flow velocity u_K can be defined, that at the boundary of the Knudsen layer equals sound velocity in the medium[11]. The velocity distribution of this gas is then described as

$$f_K^+ \propto \exp \left[-\frac{2E_I + m((v_x - u_K)^2 + v_y^2 + v_z^2)}{2k_B T_S} \right] \quad (2.7)$$

$$-\infty \leq v_x, v_y, v_z \leq \infty$$

Overcoming this region the motion of the gas is described as an unsteady adiabatic expansion, and is therefore governed by a set of conservation equations for mass, momentum and energy known as Euler equations for a compressible medium[11, 12, 8]

$$\begin{cases} \frac{\partial \rho}{\partial t} = -\frac{\partial(\rho v)}{\partial x} \\ \frac{\partial(\rho v)}{\partial t} = -\frac{\partial}{\partial x}(p + \rho v^2) \\ \frac{\partial}{\partial t} \left(E + \frac{v^2}{2} \right) = -\frac{\partial}{\partial x} \rho v \left(E + \frac{p}{\rho} + \frac{v^2}{2} \right) \end{cases} \quad (2.8)$$

During this expansion then the gas increase its flow velocity to values larger than sound velocity, while its density drops moving far from the surface. At a given distance from surface eventually density decreases below a critical value, and atoms don't collide with each other anymore therefore the fluid dynamics description provided by Euler equation is no more valid[11].

Phase Explosion

Even if vaporization occurs at all temperatures, during laser ablation melting and boiling point and critical temperature can be easily reached by irradiat-

ing a metal with a fluence of few J/cm^2 . It is then worth to discuss boiling and the extreme phenomena occurring when metal becomes a superheated liquid above boiling temperature, namely phase explosion.

Normal boiling, called heterogeneous boiling starts when vapour pressure overcomes ambient pressure, and proceeds with the nucleation of vapour bubbles from defects. In the case of ablation however bubble formation and growth and its motion toward the surface takes too long times to be considered as a predominant ablation mechanism[13].

There is however another way to reach boiling that has been proved to be the main responsible for mass removal in laser ablation of metals. When laser fluence overcomes a given threshold, heating rate becomes so high that the liquid phase has not enough time to boil following heterogeneous nucleation and becomes then a superheated liquid[13]. This is well represented by the P-T phase diagram in Figure(2.1), where phase change under equilibrium conditions is represented by the so called binodal line.

When heating rates become sufficiently high the liquid phase can over-

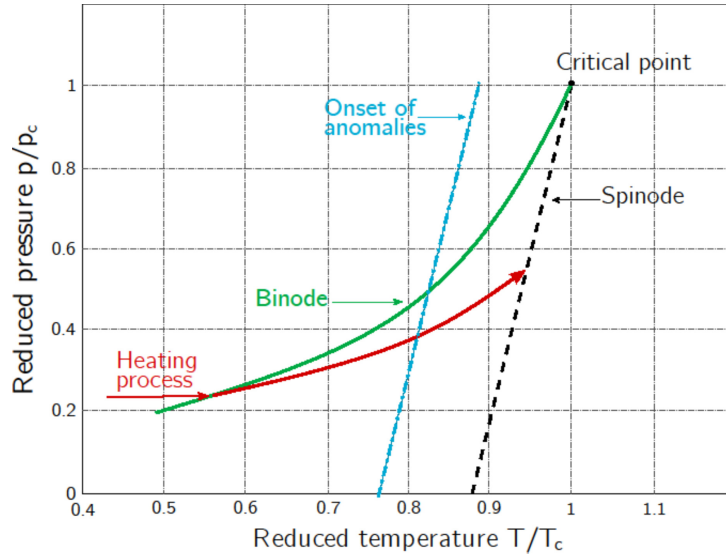


Figure 2.1: p-T diagram showing equilibrium heating with phase change at binodal line and non equilibrium heating with occurrence of phase explosion approaching critical temperature.

come binodal line without undergoing any phase transition and therefore its temperature continues to increase. The temperature of this superheated

liquid can increase only up to values close to the critical temperature T_c . This value, represented in the phase diagram by the spinodal line, represents the limit above which a liquid phase can not exist, so that a violent phase change occurs here. In this region of the phase diagram the liquid metal is in a non equilibrium state, so that strong fluctuations in density are present, and become nucleation sites for vapour bubbles as the liquid approaches the critical temperature. Compared to the heterogeneous nucleation previously described, this mechanism doesn't need defects as nucleation sites, but bubbles can form in any part of the superheated liquid, so that it is called homogeneous nucleation. Another difference is the rate at which the process occur: during homogeneous nucleation vapour bubbles can in principle generate in any point, so that when this phase change starts it proceed with extreme rapidity, with the density of vapour bubbles that grows of more than twenty orders of magnitude in an extremely short time[14].

During this intense nucleation bubbles grow until they touch each other[14], this results in an explosive ejection of both vapour and also of the interstitial liquid volumes present between bubbles, that take the form of nano sized droplets after the emission. This explosive mass ejection caused by the extremely rapid phase change is the reason why this phenomenon is usually referred to *phase explosion* or *explosive boiling*.

Phase explosion is proved experimentally to be the most efficient mass removal mechanism for metals[15] by measuring the ablation rate in terms of crater depth per pulse. Ablation rate is obtained by measuring total crater depth or total ablated mass after a given number of pulses, that can range from few hundreds to several thousands, and then considering the average value per pulse. In this kind of measurements phase explosion appears clearly as a step in ablation rate when laser fluence overcomes a material dependent threshold.

As a concluding observation, since through phase explosion liquid nanodroplets are ejected, this ablation regime represents a physical method for the synthesis of nanoparticles or nanostructured materials and surfaces.

The production of nanoparticles is usually made exploiting laser ablation in liquid. The target material is immersed in a liquid medium, like water or other organic solvents, then laser irradiation causes phase explosion and nanodroplets ejection as described, which then cool down in the liquid medium and are kept as a colloidal suspension so that can be easily collected. Compared to other chemical paths, this technique allows the production of clean

nanoparticles, that is, without the presence of residual molecules on their surface[16]. Moreover, thanks to the extreme heating and cooling rates and to the extreme thermodynamic conditions that can be reached in laser ablation in liquid, also nanodiamonds can be produced by irradiating carbon[17]. If, instead of a liquid, ablation is carried out in vacuum or in a given atmosphere, generated nanoparticles can be collected on a substrate positioned in front of the irradiated region producing a nanostructured film[18]. This technique is known as pulsed laser deposition (PLD). Depending on the presence or not of an atmosphere both metal, oxide, or core shell nanoparticles can be synthesized, so that this technique finds application in the fabrication of semiconductors that are used for instance in catalysis[19] and other fields of application.

Photomechanical spallation

Another mechanism that is worth considering is the so called photomechanical ablation, or spallation. As suggested by the name, in this case mass removal occurs because of a mechanical breaking of the irradiated surface, that results then in the ejection of solid material[20, 21].

Because of the rapid heating of the irradiated region, the volume of interaction undergoes thermal expansion, so that mechanical stress arise and a shock wave is generated that travels in the material in the direction perpendicular to the irradiated surface. If this wave reaches the opposite surface to the irradiated one a solid layer is removed when it is reflected back; instead, if its amplitude is sufficiently high, a solid layer can be removed directly from the irradiated surface[21].

An interesting point is that this ablation mechanism does not involve any phase transition, so that latent heats don't play a role and energetic efficiency is greatly increased[21]. For this reason, and because of the extremely limited thermal damage, this mechanism is now considered for application in the removal of biological tissue[21].

In order to achieve photomechanical ablation a sufficient amplitude of the shock wave must be obtained: this requires thermal and stress confinement. Thermal confinement is achieved if heat generated after laser absorption is confined in the interaction volume, this requires heat diffusion to be sufficiently low so that pulse duration is much shorter than the thermal relaxation time $t_{th} = d^2/4D$, with d the smallest dimension of the irradiated spot

(usually optical penetration depth) and D the thermal diffusivity[21]. This confined thermal increase leads to a volume expansion that must also be confined in order to increase the generated stress. Such a condition is defined stress or inertial confinement and requires the pulse duration to be much shorter than the acoustic relaxation time of the material $t_{ac} = d/c_s$ where c_s is sound velocity in the medium.

Because of these two conditions photomechanical ablation is possible in metals only with ps pulses or shorter, while in the case of polymers thermal confinement is often achieved also for ns pulses because of the low thermal diffusivity, but stress confinement is usually not reached[21]. Since pulse duration used for this work is 20 ns, this ablation mechanism will not take part in the discussion presented in the following chapters; however the diffusion of fs lasers is providing interesting results also in terms of impulse generation so this mechanism must be considered when looking at the state of the art of LAP.

2.2 Polymers

Polymers are an extremely wide category of materials with a large variety of properties. It is possible however to find some fundamental differences with metals that are responsible for the different ablation mechanism observed in this case.

From a very general point of view, polymers can be described as formed by entangled macromolecules, that are represented by chains of repeat units, called monomers. The molecular weight of such macromolecules usually ranges from 10^3 to more than 10^6 g mol⁻¹ and plays a major role in defining properties of a polymer. This means for example that increasing molecular weight (that is increasing chain length) the same polymer can change its physical state from liquid to solid, for instance[22]. This constitutes a considerable structural difference from metals, that are composed by a lattice of single atoms. It is then reasonable to expect that larger molecules are released during ablation instead of single atoms, as discussed more in detail in the following.

Unlike metals, polymers are generally dielectrics, therefore no free electrons are present as in metals. This strongly affects interaction of laser with polymers, since in this case photon energy must be sufficiently high to excite

electrons, otherwise the material is transparent[23]. As a consequence many polymers present strong light absorption only for UV wavelengths, so that in the past research on laser ablation of this category of materials was mainly conducted by using excimer lasers, that emit in this part of the spectrum. Another difference between polymers and metals concerns phase transitions: while in metals it is possible to define melting and boiling, this is hardly possible in the case of polymers. Due to their chain structure polymers are often amorphous, so that melting is usually not observed, with a few exception for those polymers that are partially crystalline. A glass transition is often observed instead, when with increasing temperature polymer chains are allowed to move with respect to each other[22]. Moreover, the transition to a gaseous phase can not be described as a vaporization, but rather as a decomposition of the polymer chains into volatile products.

2.2.1 Ablation mechanisms

Laser ablation of polymers is described in terms of a decomposition initiated by the absorption of laser photons, whose products cause a volume increase in the interaction region that leads to material ejection[24, 25]. Obviously polymers present huge differences from one another, both from the physical and chemical point of view; as a consequence decomposition follows different paths and results in different products depending on the specific polymer. A general categorization can be adopted to describe the behaviour of polymers during laser ablation, as presented in Figure(2.2), that is based on how the decomposition proceeds, either chemically or thermally.

The starting point is always the absorption of laser photons, described in general with Lambert-Beer equation[24], that leads to excitation of electrons, then decomposition can proceed in two different ways usually called *photothermal* and *photochemical*. In photothermal ablation the excited electrons relax increasing the temperature in the interaction volume, so that the system is described as in metals by the heat diffusion equation (2.2). Once temperature overcomes a material-dependent value, thermal decomposition of polymer chains starts, generating usually gaseous products, that are ejected, and residual solid products that remain in the ablation crater[26]. To model this kind of ablation a threshold on the density of the decomposition products is considered, once it is exceeded mass ejection starts. The decomposition reaction is then modeled as a rate equation following an Arrhenius

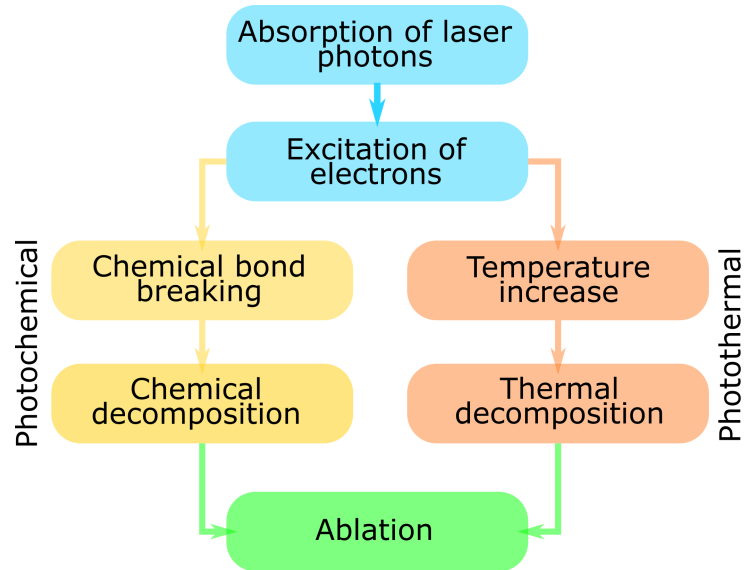


Figure 2.2: Scheme of the two generally observed ablation paths for polymers.

behaviour with temperature[24], that in turn is usually estimated from the energy absorbed following again Lambert-Beer law[24].

Photochemical ablation on the other hand does not involve any temperature increase, since excited electrons lead to direct bond breaking but also in this case a threshold in the density of products must be exceeded to obtain the ejection of material.

Independently on the ablation mechanism, laser ablation of polymers always include some kind of chemical reaction. This first of all leads to a large variety of possible ejected products, that can be single atoms, much heavier molecules like chain fragments, or even solid fragments. Moreover also energy release is possible when exothermic decomposition is present[23] that may contribute to increase the energy efficiency of the overall ablation process. The chemical modification of the irradiated region finally brings some consequences when considering multiple pulses in the same area. After the first pulse, independently if material removal was achieved or not, following pulses find a different material so that ablation process may change. In particular if a fluence below ablation threshold is used, mass removal may be observed in any case after a given number of pulses: this effect is called *incubation*[23, 27] and is caused by the fact that multiple irradiation progressively increase the number of decomposition products until mass removal is

achieved.

2.2.2 Experimental observations

An observation shared by laser ablation of all polymers is that ablation occurs only above a threshold fluence, beyond which mass removal or crater depth per pulse always grows with increasing fluence. Three fluence regions are generally observed, as shown in Figure(2.3): just above threshold a slow increase in ablation rate is observed[23], then at higher fluences ablation rate grows rapidly due to a more efficient polymer decomposition, then another slowly increasing rate is observed at high fluences where incoming laser pulse is screened by ejection products and the generated plasma plume.

Ablation rate in this three fluence ranges is usually fitted by defining a spe-

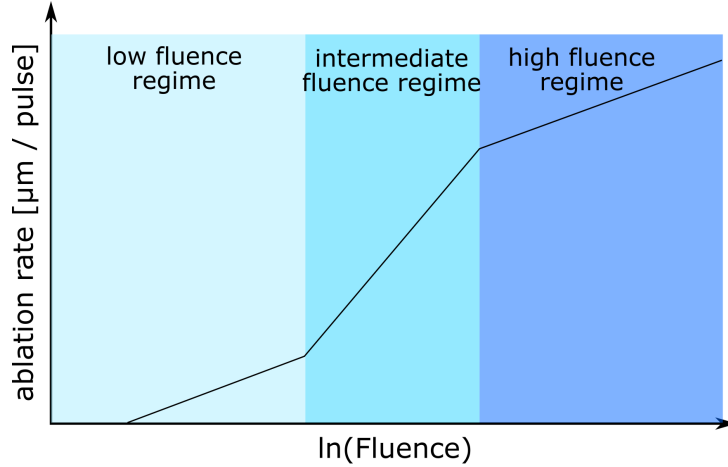


Figure 2.3: General observed behaviour for ablation rate of polymers. Adapted from[23].

cific fluence threshold F_{th} and an effective absorption coefficient α_{eff} which is in general much higher than the measured one because of the conditions of the polymer during intense irradiation or because it includes also the shielding effect of the plasma plume. Considering a Lambert-Beer behaviour a logarithmic relation for the ablated depth is then obtained

$$d(F) = \frac{1}{\alpha_{eff}} \ln \left(\frac{F}{F_{th}} \right) \quad (2.9)$$

Since its first observation[28] laser ablation of polymers attracted interest mainly as a technique for high spatial resolution etching for micromachining applications[29]. The vast majority of studies therefore concentrated on understanding the ablation process for specific polymers in the UV range, and relating it to the composition, cleanliness and resolution of the etched region. The goal for this kind of applications is to obtain efficient material removal, with spatial resolution under $1\ \mu\text{m}$ [29]: this requires high laser absorption, a limited heat affected zone, and no ablation products redeposit on the irradiated region.

Differently from metals, polymers are often transparent for visible wavelengths, therefore research mainly directed on the development of specific photosensitive polymers with high absorption coefficients at tunable wavelength [30].

For this purpose, in order to unlock laser ablation of transparent polymers, a commonly adopted approach consists in adding a chromophore to the polymer. In the majority of the cases this was obtained by introducing absorbing molecules, in order to obtain a uniformly distributed absorption throughout all the sample[29, 31, 32]; in a few cases instead absorption was increased by introducing absorbent nanoparticles embedded in the polymer, so that absorption was localized[33]. Even if some interesting results were obtained, this last approach received less interest as a possible solution to obtain clean, well defined etching profiles, since ablation starts from hotspots so that it may result in explosive material ejection[34].

2.3 Laser Ablation Propulsion

After the general discussion in the previous sections, it is now worth considering how features of laser ablation affects the generation of a mechanical impulse relating it to the ablation mechanisms presented and on literature works.

With respect to the majority of applications of laser ablation, in LAP interest is paid mainly on the features of the ejected products, rather than on the quality of the ablated surface, since mechanical impulse is generated through momentum conservation as described by equation (1.1).

By considering the ablation mechanisms previously described it is possible to draw some main observations concerning laser generated impulse both for polymers and metals, as presented in Figure(2.4).

Laser ablation of metals proceeds at low fluences with ejection of vapour

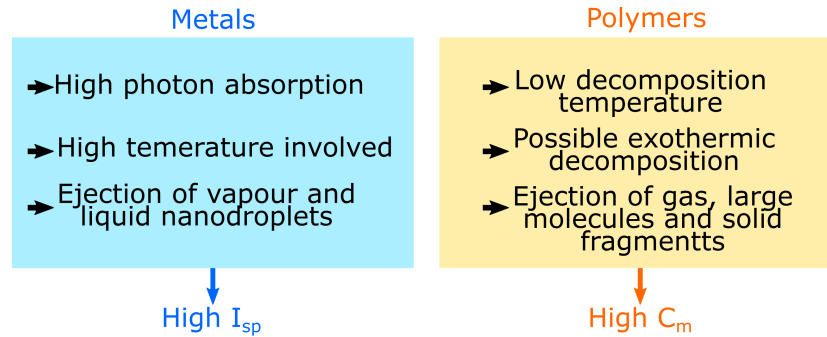


Figure 2.4: Main features of ablation of metals and polymers and their consequences in propulsion performances

which is partially ionized producing a plasma plume, while at higher fluences also liquid nanodroplets are ejected. In particular in the low fluence regime it is therefore reasonable to expect that single atoms are ejected as a gas with high temperature, so that its flow velocity will be high. In terms of propulsion performances, this means that thrust is generated accelerating light objects like single atoms or ions to extremely high exhaust velocity, so that high specific impulse (equation 1.6) of order of 10^3 s can be obtained, comparable with present electric propulsion systems. This observation also finds experimental confirmation in several works investigating impulse generated by laser ablation of several metals[35, 36, 37]. Moving then to higher fluences, phase explosion leads to a consistent increase in ablated mass[15], since also liquid phase is ejected along with vapour. However the role of this sudden increase in ejected mass in impulse generation is still not clear, since the behaviour of generated impulse with fluence seems not to be affected by this evident change in ablation mechanism[38]

Laser ablation of polymers on the other hand can produce a wide variety of different products, that can be, depending on the specific material, single atoms and heavy molecules in the gas phase up to solid fragments[23], Moreover much lower absorption coefficients are usually present in this case so that the interaction volume with the laser is increased. Also involved temperatures are different between metals and polymers, since polymer decomposition occurs in general at temperatures roughly one order of magnitude lower than boiling or critical temperature of metals. Ablation threshold for

polymers is then lower than that required for metals.

As a consequence, laser ablation of polymers results in the ejection of a large quantity of mass at low fluences, but with lower exhaust velocity, because of the lower temperatures involved. This means that the energetic efficiency of the impulse generation process is enhanced, with respect of metals, and therefore a high laser-impulse coupling coefficient, C_m is obtained (equation (1.7)), as confirmed by experimental works[39, 40].

Despite the different values, a common behaviour of C_m with fluence is observed both for metals and polymers, as presented in Figure(2.5), while I_{sp} dependence on fluence is still not so clear.

As visible C_m grows rapidly up to a maximum value and then decrease for

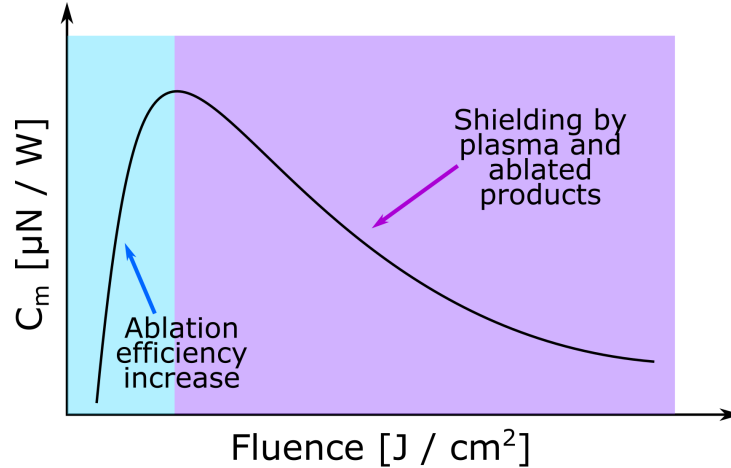


Figure 2.5: General C_m behaviour observed both for metals and polymers.

higher fluences. Considering that C_m represents the energetic efficiency in the impulse generation process, the increasing part of the curve is qualitatively explained by the fact that just above threshold fluence mass ejection becomes more and more effective[23]. This region can be roughly superimposed to the first two sections of Figure(2.3). Beyond the maximum on the other hand ablation is already well developed, but because of the interaction of a part of the laser pulse with the ejected products or with the plasma plume the laser energy that effectively reaches the target is reduced and so also the energetic efficiency[41]. This is clearly only a very general explanation of this experimental observation, and a deeper analysis can be made only considering specific cases since, as previously discussed, very different

processes are involved. In particular, while an increasing C_m trend will always be present, in some cases after the maximum the curve may decrease extremely slowly or become constant because mass ejection starts after the laser pulse.

It is then worth mentioning also the phenomenon of the confined laser ablation, that offers an interesting way to increase the mechanical impulse generated. When the surface that absorbs the laser pulse is covered by another medium the ejection of the ablated products and their expansion is somewhat hindered. In other words, the medium covering the ablated region becomes a confinement agent. Such a confinement can be obtained using a gas, a liquid or a solid and greatly enhance the mechanical impulse generated on the irradiated surface, since the pressure generated on this area is increased, as well as the time needed for the plasma plume to cool down[42]. Moreover also the confinement agent can be considered as ejected mass which can be much higher than the ablated products, but moves at much lower velocity.

Since the confinement medium is ideally transparent in this configuration, fluence threshold is not affected but generated impulse significantly grows. This means that higher C_m can be reached. For this reason recently several work considered confined ablation as a possibility to expand the applicability of LAP[43, 44, 45].

The general picture of laser ablation and its application in impulse generation that appears from this chapter is that the choice of target material must depend on the specific application. Considering the ablation mechanisms here discussed is in fact possible to define a rough guideline on propulsion properties of metals and polymers, as shown in Figure(2.4).

To go further from this first categorization of LAP materials it is now important to understand which properties are mainly relevant in impulse generation and to describe their role in this process. The final goal of this investigation will allow define pathways for the future development of specific LAP materials, as presented in the rest of this thesis.

Bibliography

- [1] Maxim V. Shugaev, Miao He, Yoann Levy, Alberto Mazzi, Antonio Miotello, Nadezhda M. Bulgakova, and Leonid V. Zhigilei. *Laser-Induced Thermal Processes: Heat Transfer, Generation of Stresses, Melting and Solidification, Vaporization, and Phase Explosion*, pages 1–81. Springer International Publishing, Cham, 2020. ISBN 978-3-319-69537-2. doi: 10.1007/978-3-319-69537-2_11-1.
- [2] Maxim V. Shugaev, Chengping Wu, Oskar Armbruster, Aida Naghilou, Nils Brouwer, Dmitry S. Ivanov, Thibault J.-Y. Derrien, Nadezhda M. Bulgakova, Wolfgang Kautek, Baerbel Rethfeld, and et al. Fundamentals of ultrafast laser–material interaction. *MRS Bulletin*, 41(12): 960–968, 2016. doi: 10.1557/mrs.2016.274.
- [3] A. Gragossian, S. H. Tavassoli, and B. Shokri. Laser ablation of aluminum from normal evaporation to phase explosion. *Journal of Applied Physics*, 105(10):103304, 2009. doi: 10.1063/1.3131689.
- [4] Leonid V. Zhigilei, Zhibin Lin, Dmitriy S. Ivanov, Elodie Leveugle, William H. Duff, Derek Thomas, Carlos Sevilla, and Stephen J. Guy. *Atomic/Molecular-Level Simulations of Laser–Materials Interactions*, pages 43–79. Springer Berlin Heidelberg, Berlin, Heidelberg, 2010. ISBN 978-3-642-03307-0. doi: 10.1007/978-3-642-03307-0_3.
- [5] Yeqing Wang, Ninggang Shen, Getachew K. Befekadu, and Crystal L. Pasiliao. Modeling pulsed laser ablation of aluminum with finite element analysis considering material moving front. *International Journal of Heat and Mass Transfer*, 113:1246–1253, 2017. ISSN 0017-9310. doi: <https://doi.org/10.1016/j.ijheatmasstransfer.2017.06.056>.
- [6] NM Bulgakova and AV Bulgakov. Pulsed laser ablation of solids: transition from normal vaporization to phase explosion. *Applied Physics A*, 73(2):199–208, 2001.
- [7] Nadezhda M. Bulgakova, Razvan Stoian, Arkadi Rosenfeld, and In-golf V. Hertel. *Continuum Models of Ultrashort Pulsed Laser Ablation*, pages 81–97. Springer Berlin Heidelberg, Berlin, Heidelberg, 2010. ISBN 978-3-642-03307-0. doi: 10.1007/978-3-642-03307-0_4.

- [8] Jacopo Terragni and Antonio Miotello. Laser ablation of aluminum near the critical regime: A computational gas-dynamical model with temperature-dependent physical parameters. *Micromachines*, 12(3), 2021. ISSN 2072-666X. doi: 10.3390/mi12030300.
- [9] SI Anisimov, BL Kapeliovich, TL Perelman, et al. Electron emission from metal surfaces exposed to ultrashort laser pulses. *Zh. Eksp. Teor. Fiz*, 66(2):375–377, 1974.
- [10] Andrea Peterlongo, Antonio Miotello, and Roger Kelly. Laser-pulse sputtering of aluminum: Vaporization, boiling, superheating, and gas-dynamic effects. *Phys. Rev. E*, 50:4716–4727, Dec 1994. doi: 10.1103/PhysRevE.50.4716. URL <https://link.aps.org/doi/10.1103/PhysRevE.50.4716>.
- [11] Roger Kelly. On the dual role of the knudsen layer and unsteady, adiabatic expansion in pulse sputtering phenomena. *The Journal of Chemical Physics*, 92(8):5047–5056, 1990. doi: 10.1063/1.458540.
- [12] Antonio Miotello, Andrea Peterlongo, and Roger Kelly. Laser-pulse sputtering of aluminium: gas-dynamic effects with recondensation and reflection conditions at the knudsen layer. *Nuclear Instruments and Methods in Physics Research Section B: Beam Interactions with Materials and Atoms*, 101(1):148–155, 1995. ISSN 0168-583X. doi: [https://doi.org/10.1016/0168-583X\(95\)00294-4](https://doi.org/10.1016/0168-583X(95)00294-4).
- [13] Antonio Miotello and Roger Kelly. Laser-induced phase explosion: new physical problems when a condensed phase approaches the thermodynamic critical temperature. *Applied Physics A*, 69(1):S67–S73, 1999.
- [14] Alberto Mazzi, Federico Gorrini, and Antonio Miotello. Liquid nanodroplet formation through phase explosion mechanism in laser-irradiated metal targets. *Phys. Rev. E*, 92:031301, Sep 2015. doi: 10.1103/PhysRevE.92.031301.
- [15] Cristian Porneala and David A. Willis. Observation of nanosecond laser-induced phase explosion in aluminum. *Applied Physics Letters*, 89(21):211121, 2006. doi: 10.1063/1.2393158.

- [16] S.I. Dolgaev, A.V. Simakin, V.V. Voronov, G.A. Shafeev, and F. Bozon-Verduraz. Nanoparticles produced by laser ablation of solids in liquid environment. *Applied Surface Science*, 186(1):546–551, 2002. ISSN 0169-4332. doi: [https://doi.org/10.1016/S0169-4332\(01\)00634-1](https://doi.org/10.1016/S0169-4332(01)00634-1). PROCEEDINGS OF THE EUROPEAN MATERIALS RESEARCH SOCIETY 2001-SYMPOSIUM L "PHOTON-INDUCED SURFACE PROCESSING".
- [17] Luca Basso, Nicola Bazzanella, Massimo Cazzanelli, and Antonio Miotello. On the route towards a facile fluorescent nanodiamonds laser-synthesis. *Carbon*, 153:148–155, 2019. ISSN 0008-6223. doi: <https://doi.org/10.1016/j.carbon.2019.07.025>.
- [18] Marco Bonelli, Claudio Cestari, and Antonio Miotello. Pulsed laser deposition apparatus for applied research. *Measurement Science and Technology*, 10(3):27, 1999.
- [19] R. Edla, N. Patel, M. Orlandi, N. Bazzanella, V. Bello, C. Maurizio, G. Mattei, P. Mazzoldi, and A. Miotello. Highly photo-catalytically active hierarchical 3d porous/urchin nanostructured Co_3O_4 coating synthesized by pulsed laser deposition. *Applied Catalysis B: Environmental*, 166-167:475–484, 2015. ISSN 0926-3373. doi: <https://doi.org/10.1016/j.apcatb.2014.11.060>. URL <https://www.sciencedirect.com/science/article/pii/S0926337314007772>.
- [20] E Leveugle, Dmitriy S Ivanov, and Leonid V Zhigilei. Photomechanical spallation of molecular and metal targets: molecular dynamics study. *Applied Physics A*, 79(7):1643–1655, 2004.
- [21] Günther Paltauf and Peter E Dyer. Photomechanical processes and effects in ablation. *Chemical reviews*, 103(2):487–518, 2003.
- [22] Leslie H Sperling. *Introduction to physical polymer science*. John Wiley & Sons, 2005.
- [23] Thomas Lippert. *UV Laser Ablation of Polymers: From Structuring to Thin Film Deposition*, pages 141–175. Springer Berlin Heidelberg, Berlin, Heidelberg, 2010. ISBN 978-3-642-03307-0. doi: [10.1007/978-3-642-03307-0_7](https://doi.org/10.1007/978-3-642-03307-0_7).

- [24] N. Bityurin, B. S. Luk'yanchuk, M. H. Hong, and T. C. Chong. Models for laser ablation of polymers. *Chemical Reviews*, 103(2):519–552, 2003. doi: 10.1021/cr010426b. PMID: 12580641.
- [25] H. Schmidt, J. Ihlemann, B. Wolff-Rottke, K. Luther, and J. Troe. Ultraviolet laser ablation of polymers: spot size, pulse duration, and plume attenuation effects explained. *Journal of Applied Physics*, 83(10):5458–5468, 1998. doi: 10.1063/1.367377.
- [26] Thomas Lippert and J. Thomas Dickinson. Chemical and spectroscopic aspects of polymer ablation: Special features and novel directions. *Chemical Reviews*, 103(2):453–486, 2003. doi: 10.1021/cr010460q.
- [27] R. Srinivasan, Bodil Braren, and Kelly G. Casey. Nature of “incubation pulses” in the ultraviolet laser ablation of polymethyl methacrylate. *Journal of Applied Physics*, 68(4):1842–1847, 1990. doi: 10.1063/1.346620.
- [28] R. Srinivasan and V. Mayne-Banton. Self-developing photoetching of poly(ethylene terephthalate) films by far-ultraviolet excimer laser radiation. *Applied Physics Letters*, 41(6):576–578, 1982. doi: 10.1063/1.93601.
- [29] Thomas Lippert, Akira Yabe, and Alexander Wokaun. Laser ablation of doped polymer systems. *Advanced Materials*, 9(2):105–119, 1997. doi: <https://doi.org/10.1002/adma.19970090203>.
- [30] T. Lippert, J. Stebani, J. Ihlemann, O. Nuyken, and A. Wokaun. Excimer laser ablation of novel triazene polymers: influence of structural parameters on the ablation characteristics. *The Journal of Physical Chemistry*, 97(47):12296–12301, 1993. doi: 10.1021/j100149a033.
- [31] Juergen Ihlemann, Matthias Bolle, Klaus Luther, and Juergen Troe. Near-UV laser ablation of doped polymers. In Manijeh Razeghi, editor, *Physical Concepts of Materials for Novel Optoelectronic Device Applications I: Materials Growth and Characterization*, volume 1361, pages 1011 – 1019. International Society for Optics and Photonics, SPIE, 1991. doi: 10.1117/12.24328.
- [32] R. Srinivasan, B. Braren, R. W. Dreyfus, L. Hadel, and D. E. Seeger. Mechanism of the ultraviolet laser ablation of polymethyl methacrylate

- at 193 and 248 nm: laser-induced fluorescence analysis, chemical analysis, and doping studies. *J. Opt. Soc. Am. B*, 3(5):785–791, May 1986. doi: 10.1364/JOSAB.3.000785.
- [33] Xiaoning Wen, David E. Hare, and Dana D. Dlott. Laser polymer ablation threshold lowered by nanometer hot spots. *Applied Physics Letters*, 64(2):184–186, 1994. doi: 10.1063/1.111526.
- [34] Rusty W. Conner and Dana D. Dlott. Time-resolved spectroscopy of initiation and ignition of flash-heated nanoparticle energetic materials. *The Journal of Physical Chemistry C*, 116(28):14737–14747, 2012. doi: 10.1021/jp303077f.
- [35] Andrew V. Pakhomov and Don A. Gregory. Ablative laser propulsion: An old concept revisited. *AIAA Journal*, 38(4):725–727, 2000. doi: 10.2514/2.1021.
- [36] Claude R Phipps, James R Luke, and Wesley D Helgeson. 3ks specific impulse with a ns-pulse laser microthruster. Technical report, PHOTONIC ASSOCIATES SANTA FE NM, 2005.
- [37] Claude R. Phipps, James R. Luke, and Wesley Helgeson. Laser-powered multi-newton thrust space engine with variable specific impulse. In Claude R. Phipps, editor, *High-Power Laser Ablation VII*, volume 7005, page 70051X. International Society for Optics and Photonics, SPIE, 2008. doi: 10.1117/12.786459.
- [38] J.M. Fishburn, M.J. Withford, D.W. Coutts, and J.A. Piper. Study of the fluence dependent interplay between laser induced material removal mechanisms in metals: Vaporization, melt displacement and melt ejection. *Applied Surface Science*, 252(14):5182–5188, 2006. ISSN 0169-4332. doi: <https://doi.org/10.1016/j.apsusc.2005.07.053>.
- [39] L. Urech, T. Lippert, C.R. Phipps, and A. Wokaun. Polymer ablation: From fundamentals of polymer design to laser plasma thruster. *Applied Surface Science*, 253(15):6409–6415, 2007. ISSN 0169-4332. doi: <https://doi.org/10.1016/j.apsusc.2007.01.026>. Proceedings of the Fifth International Conference on Photo-Excited Processes and Applications.

- [40] C. Phipps, J. Luke, T. Lippert, M. Hauer, and A. Wokaun. Micropropulsion using a laser ablation jet. *Journal of Propulsion and Power*, 20(6): 1000–1011, 2004. doi: 10.2514/1.2710.
- [41] Claude R. Phipps. *Laser Ablation Propulsion and Its Applications in Space*, pages 217–246. Springer International Publishing, Cham, 2018. ISBN 978-3-319-96845-2. doi: 10.1007/978-3-319-96845-2_8.
- [42] R. Fabbro, J. Fournier, P. Ballard, D. Devaux, and J. Virmont. Physical study of laser-produced plasma in confined geometry. *Journal of Applied Physics*, 68(2):775–784, 1990. doi: 10.1063/1.346783.
- [43] Y Zhang, X Lu, ZY Zheng, F Liu, PF Zhu, HM Li, YT Li, YJ Li, and J Zhang. Transmitted laser propulsion in confined geometry using liquid propellant. *Applied Physics A*, 91(2):357–360, 2008.
- [44] Haichao Yu, Xiao Wu, Yonggui Yuan, Hanyang Li, and Jun Yang. Confined geometry and laser energy affect laser plasma propulsion. *Opt. Express*, 27(7):9763–9772, Apr 2019. doi: 10.1364/OE.27.009763.
- [45] Soojin Choi, Tae-hee Han, Ardian B Gojani, and Jack J Yoh. Thrust enhancement via gel-type liquid confinement of laser ablation of solid metal propellant. *Applied Physics A*, 98(1):147–151, 2010.

Chapter 3

Experimental setup for impulse measurement

In the previous chapter the problem of space propulsion for nanosatellites was discussed, and laser ablation was introduced as an attractive solution, allowing thrust generation on far objects ideally without any need of power storage and propulsion systems on board. This chapter will now face the problem of the experimental measurement of propulsion performances obtained by laser ablation.

3.1 Considerations on orders of magnitude and experimental techniques

As a starting point for this experimental investigation it is worth summing up what are the parameters to measure and their order of magnitude, that are fundamental for a correct design for an apparatus. The main parameter to consider in LAP is the laser-impulse coupling coefficient, C_m , defined in equation (1.7). To obtain C_m the mechanical impulse generated by laser ablation must be measured, along with the energy of the laser pulse. Moreover from literature values[1, 2] it is also possible to obtain an order of magnitude estimation of the expected mechanical impulse generated. Commonly obtained C_m values are of order $10^2 \div 10^3 \mu\text{N W}^{-1}$ while, as discussed in the following, laser pulse energy of the laser employed for these experiments of the order of $10 \div 10^2$ mJ. This means that mechanical impulses of $\sim 10 \mu\text{N s}$

can be expected. It must also be noted here that these C_m values generally refer to the maximum of the curve, so also much lower impulses may be found, in particular at low fluences.

It is also interesting to make a comparison with apparatuses commonly employed for other micropropulsion systems: the main difference is that in these cases a continuous thrust is generated, rather than a short mechanical impulse, so that a continuous force for time duration of tens of seconds[3] is usually measured. The momentum variation obtained for example by applying a mN thrust for so long time is extremely larger than impulse generated by laser ablation, so these apparatuses can not be used for LAP purposes.

Another important parameter to consider is specific impulse I_{sp} , defined in equation (1.6), that can be reasonably expected to be $\sim 10^3$ s[1, 2]. I_{sp} is sometimes obtained by measuring the exhaust velocity of the ablated products[4], however it is desirable to obtain it by measuring generated impulse and ejected mass since this is more coherent with its definition of mass efficiency in thrust generation. Considering expected impulse values previously discussed it is possible to estimate that the ejected mass during impulse generation can be of $\mu\text{g}/\text{pulse}$, but again much smaller values are possible in case of smaller impulses.

3.1.1 Experimental techniques for impulse measurements

Given the particular magnitude of the laser generated impulse and of its timescale, specific apparatuses must be designed in order to obtain reliable measurements. Three main categories of systems are used: ballistic pendulums[5, 6, 7, 8, 9], torsion pendulums[10, 11] and load cells[12, 4, 13, 14].

In the case of a ballistic pendulum the target material is suspended using thin wires[5, 6, 8] or a blade edge[15, 7], with the aim of reducing friction as much as possible. The classical way to perform an impulse measurement with a ballistic pendulum consists in shining the laser on the target material while it is completely still, so that the generated impulse will make it oscillate under the restoring force given by gravity. The magnitude of the generated impulse can then be obtained by measuring the angle of maximum deflection, similarly to what is done in the measurement of the velocity of a bullet, even if on much different scales. Impulse can be obtained also if the

laser pulse irradiates the pendulum while it is oscillating[5, 9], in this case the variation in motion of the pendulum must be analyzed, rather than the amplitude of its oscillations. A detailed analysis of both these situation will be presented further in this chapter.

Despite its simplicity some details in a measurement based on a ballistic pendulum require particular care. First of all damping of pendulum motion must be reduced to a minimum or well known in order to be included in the analysis, since it affects either the amplitude of oscillations or how the impulse change its motion. As a consequence of this fact, it is not always possible to assure that the rotation of the pendulum after impulse proceeds around a single well defined axis, this of course also affect the measurement and requires the pendulum to be a rigid object. This brings to another problem: a pendulum composed by a rigid object often can not be treated as an ideal simple pendulum, but rather as a physical pendulum for which mass and moment of inertia matter. Lastly, since impulse to be measured are small, the pendulum must be light or with a low moment of inertia, making it difficult to obtain a stable structure.

Torsion pendulums rely on the restoring momentum given by the torsion of a thin wire on which they are hung, the principle at the basis of impulse measurement is therefore the same as that of a ballistic pendulum. The main advantage of such a system is that by correctly choosing the wire on which the pendulum is suspended it is possible to obtain a restoring momentum that can be much smaller than that given by gravity, making the pendulum more sensitive to small impulses. On the other hand, also because of the small restoring momentum, measurements with this kind of system can be unpractical because of its slow oscillations, and other vibrations possible around all other axes. Moreover a counterweight is needed to keep the arms of the pendulum in the horizontal position, so that each time a new target is fixed on it a new balancing must be made. A last important drawback for torsion pendulums is eventually the fact that the restoring momentum given by the wire is not known, so that a calibration is needed to perform the measurement, constituting an additional source of uncertainty. It must also be noted that calibration of the restoring momentum of the wire is usually made by applying a constant force to one arm of the pendulum and measuring the deflection[11]. This condition is far from the impulse generated by laser ablation which, given the same final deflection of the pendulum, is represented by a much more intense force applied for a much shorter time,

possibly leading also to vibrations.

The last technique to measure thrust generated by laser ablation is substantially different from ballistic or torsion pendulums and is based on piezoelectric sensors or load cells. In this case the sample is fixed on the sensor and the generated thrust is converted into an electric signal: therefore also in this case a calibration is needed.

With piezoelectric sensors also the force generated by a single impulse can be measured, but due to the short time duration it is applied also response time of the instrument must be taken into account, making analysis more complex and possibly increasing its uncertainty[4, 13]. Similarly, load cells can measure only the average force generated by continuously irradiating the target material with multiple pulses at a given frequency[14, 12]. Clearly, even if the impulse generated by a single pulse can be estimated knowing the laser repetition rate, the target material under these conditions is modified because of high temperatures and progressive change in surface roughness. This of course affects the impulse generated by a single laser pulse, in the sense that impulse generated by the first pulse will be different than that generated by later ones. This is particularly true for polymers, where chemical modification of surface occurs after laser irradiation.

Given all these consideration the ballistic pendulum was chosen as the most suitable apparatus for the research carried out in this thesis. The main reasons are the following:

- Measurements without any calibration are possible, provided that all parameters involved are known. This means that if oscillation period, center of mass position and moment of inertia are known the measurement can be carried out without testing the pendulum with a known impulse. Measurement of such parameters can be tricky on a complex object like a physical pendulum, and can be partially avoided by shining the laser on its center of mass[5]. This strategy however is extremely limiting so, as described in the following, a procedure to measure them was developed[16].
- The focus of this research is on material properties that affect impulse generation, so average thrust obtained by irradiating multiple times the same region can not give reliable information, so that load cells are excluded.

- Changing the target in such a system is much easier with respect to torsion pendulum, since no counterweight is needed and since target with non well defined shape can be used, because center of mass position and moment of inertia are measured.

3.2 Apparatus for impulse measurement

The ballistic pendulum is the most suitable apparatus for a systematic study aimed to impulse generated by laser ablation of a material and its properties. In the design of such a system several aspect must be considered carefully, in order to reduce uncertainties and obtain reliable and reproducible results. In particular, since the measurement is based on the motion of a physical object, this must be known with the best possible accuracy: this strongly affects both the design and the physical analysis of the system, presented in the following.

3.2.1 Technical design of the apparatus

Overall scheme of the apparatus

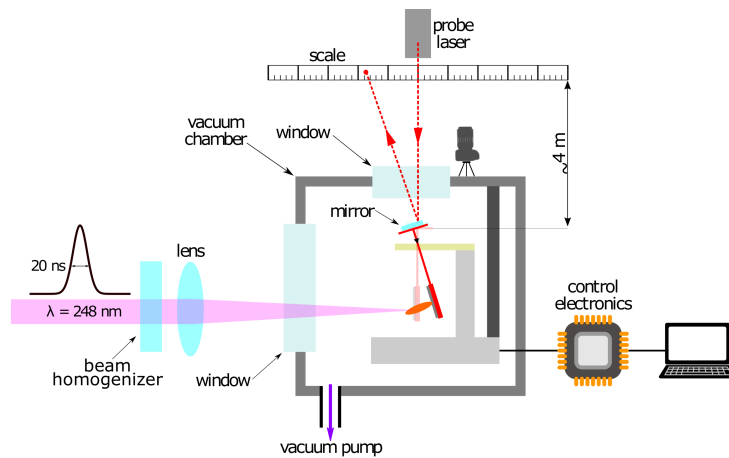


Figure 3.1: Overall scheme of the experimental apparatus for impulse measurements.

Figure(3.1) gives an overall scheme of the experimental apparatus. The laser pulse is generated by a KrF excimer laser, emitting at a wavelength of

248 nm with a pulse duration of 20 ns. The intensity distribution of the laser pulse is shaped by means of a beam homogenizer, as described in detail in next chapter, and is then focused by means of a spherical lens. Radiation then enters in the vacuum chamber through an anti reflection window and irradiates the pendulum, positioned in the chamber with all its supports and displacement systems.

Oscillations of the pendulum are usually of the order of a fraction of degree, therefore for an accurate detection they need to be amplified. This is done by means of a probe laser, which is a He-Ne emitting at 632 nm positioned on the ceiling, at about 4 m from the pendulum. The probe laser enters the vacuum chamber through an anti reflection window and is reflected by a mirror placed on the top of the pendulum, so that its oscillation appear amplified thanks to the motion of the reflected spot on a graduated scale, put at the same altitude of the probe laser.

The motion of the pendulum is eventually acquired by means of a camera that acquires a video at 1000 fps. The acquisition time is roughly 4 s, during which the motion of the pendulum before and after the impulse is collected. To ensure a steady pulse energy output from the laser, a some tenths of pulses are needed: a shutter synchronized with the camera is therefore used. The shutter is made by a pendulum that is kept fixed at a given amplitude by an electromagnet so that the first laser pulses hits it and can not reach optics and the pendulum. The electromagnet is used to release the shutter pendulum roughly 2 s after the camera starts recording. This system allows to avoid fluctuations in output energy of the laser and also to set the recording of the impulse at about half of the video, so that motion of the pendulum can be well acquired both before and after impulse. This system clearly do not allow to set precisely impulse instant in the acquired video, so that it must be identified during the analysis as described in the following.

Damping

The best way to use a ballistic pendulum for impulse measurements is to make it work in ideal conditions, so that its motion can be easily considered also from the theoretical point of view.

An ideal motion of the pendulum requires damping to be negligible, at least in the timescales required for the measure; this means that all the possible friction sources must be eliminated, or limited as much as possible. In the case of an oscillating pendulum the main sources of damping are essentially

three: viscous drag due to the atmosphere, friction on the fulcrum and also vibrations, that may act as an external force on the object.

Viscous drag clearly can be removed by operating the pendulum in vacuum. This is also suitable because, as discussed in the previous chapter, the presence of an atmosphere plays a role in laser ablation, acting as a confinement agent that in principle is not present in space.

The pendulum, along with all its supports and electronics, is therefore po-

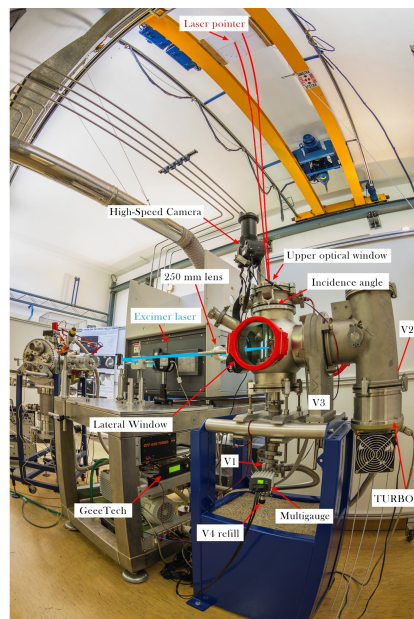


Figure 3.2: Picture showing all the parts of the apparatus.

sitioned in a vacuum chamber, presented in Figure(3.2), which is evacuated by means of a magnetic levitation turbomolecular pump backed by a rotary pump. In such a configuration the measurements can take place at pressure lower than 10^{-4} mbar.

The main drawback of using vacuum pumps is the presence of vibrations, that come also from the laser system because of electronics and cooling fans. In order to reduce vibrations as much as possible a support for the vacuum chamber was specifically designed so that vibrations coming from external environment can be suppressed by fixing it on the ground through some thick rubber foils and by stabilizing it with approximately 250 kg of sand. Addi-

tionally vibrations coming from the turbomolecular pump, that is in direct contact with the chamber, are extremely reduced thanks to its magnetic levitation and by separating its cooling fan from all the system.

The last damping factor to consider is the friction on the fulcrum of the pendulum. Many ballistic pendulums exploit thin wires to reduce friction, however in this configuration the pendulum is not a rigid object so that impulse generation may induce vibrations other than pendulum oscillations, affecting the measurement. In this case two sharp tips with a $10\ \mu\text{m}$ top diameter are used as fulcrum, as shown in Figure(3.3).

A first attempt used two iron tips, but due to their sharpness the weight of

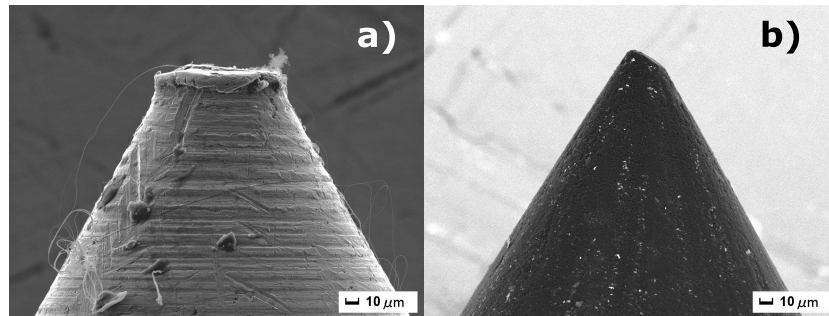


Figure 3.3: Fulcrum tips of the pendulum. **a)** Iron tip; **b)** Diamond cover tip.

the pendulum (roughly 8 g) was enough to deform them affecting drastically the oscillations, as visible in Figure(3.3,a). Much harder diamond covered tips have been used instead, avoiding deformations as clear from figure(3.3,b). This solution guarantees good results, as discussed in the following, but as a drawback these tips progressively scratch the quartz substrate on which the pendulum oscillates. Nevertheless this is only a matter of maintenance of the apparatus and is easily solvable.

Pendulum, supports and displacement system

In order to allow a systematic investigation, the shape of the pendulum must be designed carefully to avoid its unbalancing and unwanted movements of the target fixed on it. Similarly, systems for displacement of the pendulum are needed so that different regions of the target can be irradiated. Moreover also a system for a careful release of the pendulum must be used, so that

fulcrum tips and quartz substrate are not damaged and the position of the pendulum is well reproducible.

Thanks to its rapidity of design and easiness of fabrication, 3D printing was extensively used to build the pendulum and other parts of the apparatus. In the design of the pendulum particular care was taken to the position of its center of mass and of its moment of inertia, that are the main parameters that affect its motion and its sensitivity to the imparted mechanical impulse. For this reason two pendulums were made, one having a much smaller moment of inertia with respect to the other.

Figure(3.4,a) shows the heavier of the two pendulums, where important

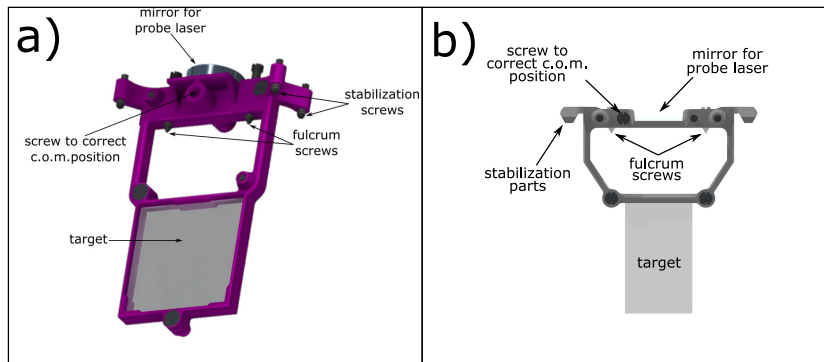


Figure 3.4: The two pendulums designed for the apparatus. The larger pendulum in **a)** has a moment of inertia about ten times higher than the pendulum in **b)**.

features are easily visible. The heavier pendulum is essentially constituted by a PLA frame in which a $26 \times 26 \text{ mm}^2$ target can be fixed. A series of screws is visible: the two fulcrum tips, four stabilization screws that are used to lift and release carefully the pendulum on the substrate and a screw to correct center of mass position, that may change for different targets. The mirror for the reflection of the probe laser is also shown. Similar features can be identified also for the other pendulum, in this case the moment of inertia is reduced to a minimum and is roughly one tenth with respect to the heavier pendulum. In order to do this the mass distribution was studied to reduce mass far from the rotation axis of the pendulum.

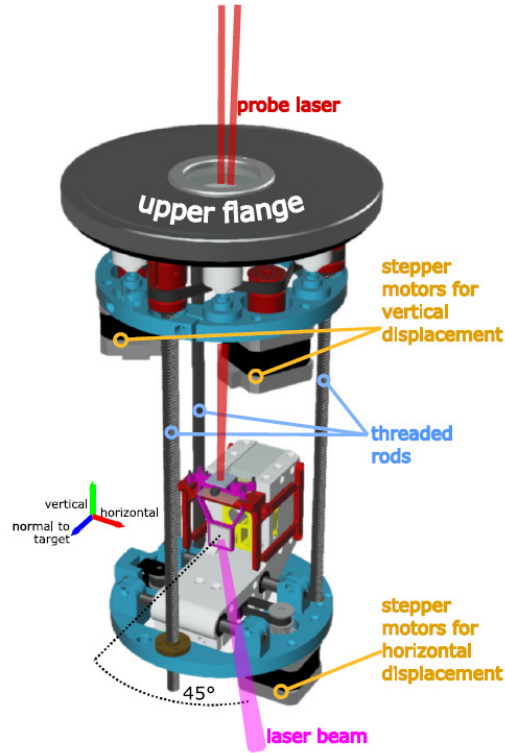


Figure 3.5: Displacement systems for the pendulum inside the chamber.

An overview of all the displacement systems is presented in Figure(3.5). Almost all the components are 3D printed, while the other parts and the control electronics are obtained by modifying a second 3D printer. The pendulum can be moved in the vertical direction and horizontally, as indicated in Figure(3.5). These movements are obtained using stepper motors, gears and threaded rods, that allow displacements as small as 0.1 mm. All the displacement system is then fixed on the upper flange of the vacuum chamber, so that the pendulum can also be tilted with respect to the incoming laser beam direction.

The last systems to consider is the support for the release of the pendulum, presented in Figure(3.6). The support is visible in red in Figure(3.6) and can move up to stop the oscillation of the pendulum and lift it from the substrate or down to release it for free oscillation. This movement is obtained by a plastic deformation of this red frame, obtained by the rotation of an eccentric pin given by a stepper motor. In order to keep the pendulum in a

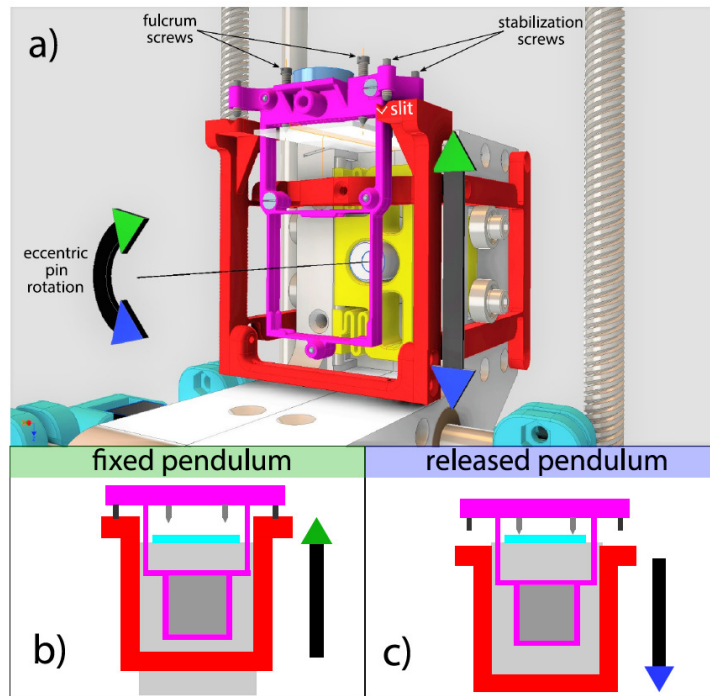


Figure 3.6: **a)** System for release and lift of the pendulum. The slits where the stabilization screws and the eccentric pin to move the supports are visible. The pendulum is fixed **(b)** when supports move upwards, while it is released **(c)** when supports move downward

well defined position four slits are present in the upper part of the support, where the four stabilization screws of the pendulum fit.

Ideally such a system should also allow to release the pendulum so that it is perfectly still. However, as also discussed in the following, the pendulum is never still after release and small oscillations are always detected.

These displacements systems can be easily programmed to perform automated motion, since they are built from a 3D printer. This offers an interesting capability to be exploited for ablated mass measurements, that require thousands of consecutive laser pulses. Automatic motion of the target allows to avoid irradiating many times the same region, so that a clean surface is always ablated. A target holder for ablated mass measurements was therefore specifically designed and printed, as shown in Figure(3.7). The target holder fits in the slits of the releasing support by means of four screws

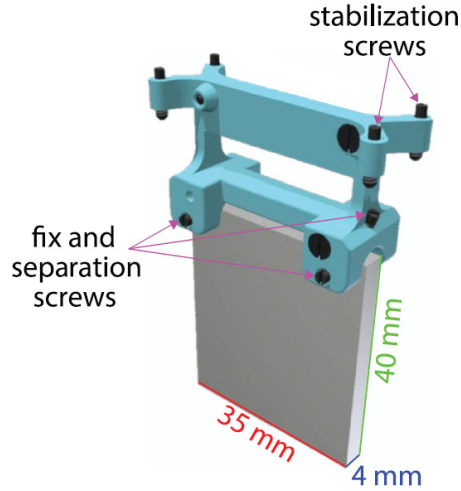


Figure 3.7: Target holder

identical to the stabilization screws of the pendulum, but it can not oscillate since as visible no fulcrum tips are present. A larger target is considered in this case, in order to have a wider area that can be irradiated and, due to its mass, reduce temperature increase due to the high number of laser pulses. Moreover, to limit as much as possible the contact of the hot target with the target holder, made of PLA, six screws are used.

3.2.2 Physical analysis of pendulum motion

It appears clear from Figure(3.4) that the ballistic pendulum used for this investigations can not be considered as an ideal pendulum, represented by a point mass tied to a massless wire. This means that, differently from the ideal case, the mass of the pendulum and in particular its spatial distribution play a role in determining its motion. Indeed, the equation of motion for a physical pendulum reads

$$I \frac{d\theta(t)}{dt} = -mgd \sin \theta(t) \quad (3.1)$$

with I the moment of inertia of the pendulum with respect to the rotation axis, m its mass, g gravity acceleration and d the distance of the center of mass of the pendulum from the rotation axis. Under the approximation for

small oscillations, that holds in this case, equation (3.1) clearly represents an harmonic motion with pulsation $\Omega^2 = mgd/I$ whose oscillation in time are described as

$$\theta(t) = \theta_0 \sin(\Omega t + \phi) \quad (3.2)$$

Effect of a mechanical impulse on pendulum motion

During laser ablation a force is applied to the irradiated surface for a time that is much shorter than the sampling rate with which the pendulum motion is observed. What is measured is therefore the impulse J caused by this force F :

$$\vec{J} = \int_0^\tau \vec{F}(t) dt \quad (3.3)$$

where τ is the time duration for which the force is applied. It must be noted here that F and consequently J are always normal to the irradiated region, due to the almost cylindrical symmetry of mass ejection. In addition there is only one axis around which the pendulum can rotate, the one defined by the fulcrum tips, moment of inertia therefore is a scalar.

The effect of the mechanical impulse imparted on the pendulum is to change its angular momentum ΔL . Given the considerations just made the direction of this vector is the same as that defined by the rotation of the pendulum therefore it can be simply written as

$$\Delta L = rJ = I\Delta\omega \quad (3.4)$$

where r is the arm of the force imparted on the pendulum, that is the distance of the irradiated spot from the rotation axis and $\Delta\omega$ is the instantaneous variation in angular velocity of the pendulum caused by the impulse.

From equation (3.4) it is clear that, to obtain J , a measure of $\Delta\omega$ must be made with the ballistic pendulum, while I and r are obtained with another measure discussed in the following. The simplest and most common way to obtain $\Delta\omega$ is to perform the measurement irradiating the pendulum while it is still. In this situation the variation in angular velocity of the pendulum is equal to its angular velocity immediately after the impulse, $\omega(t_{imp})$. This angular velocity can be obtained by measuring the amplitude of oscillation of the pendulum after the impulse, θ_{max} , that is related to $\omega(t_{imp})$ by energy conservation

$$\frac{1}{2}I\omega(t_{imp})^2 = mgd(1 - \cos\theta_{max}) \quad (3.5)$$

At this point, since $\Delta\omega = \omega(t_{imp})$ and knowing I and r , J can be obtained from equation (3.4) and (3.5)

$$J = \left[\frac{2I m g d}{r^2} (1 - \cos \theta_{max}) \right]^{\frac{1}{2}} \quad (3.6)$$

In the case in which all the motion of the pendulum can be acquired, a direct measurement of $\Delta\omega$ is possible, so that J can be obtained directly from equation (3.4). Moreover, this allows to measure J even if the pendulum oscillates both before and after impulse generation, so that $\Delta\omega$ is different from angular velocity just after impulse. This is a great advantage when damping of the pendulum is reduced to a minimum, like in the case considered here, so that it would take really long times from a measure to the following one, and in any case assuming the pendulum to be still at the instant of impulse generation is not possible.

3.3 Data analysis

Oscillations of this pendulum are usually of fractions of degree, for this reason its motion is acquired by reflecting a probe laser with a long optical path, so that oscillations as well as variations in motion are amplified. The motion of the pendulum in time is therefore reconstructed starting from the acquired video and considering then the geometry of the apparatus. Once pendulum motion is known, time instant in which impulse occurred can be found, so that also $\Delta\omega$ is obtained. Figure(3.8) shows the flowchart of data analysis to compute the generated impulse, that is described in detail in the following.

3.3.1 Video tracking

The output of the measurement is a video recording 4s of motion of the reflected probe laser on a graduated scale. In order to extract this motion, distances on the scale must be calibrated using known references on it, and the position of the reflected spot on the scale must be measured for each frame.

A picture of the scale and the reflected spot is presented in Figure(3.9). The lines on the scale give known distances to calibrate the measure and are so positioned in order to have the majority of the scale of the same color, so

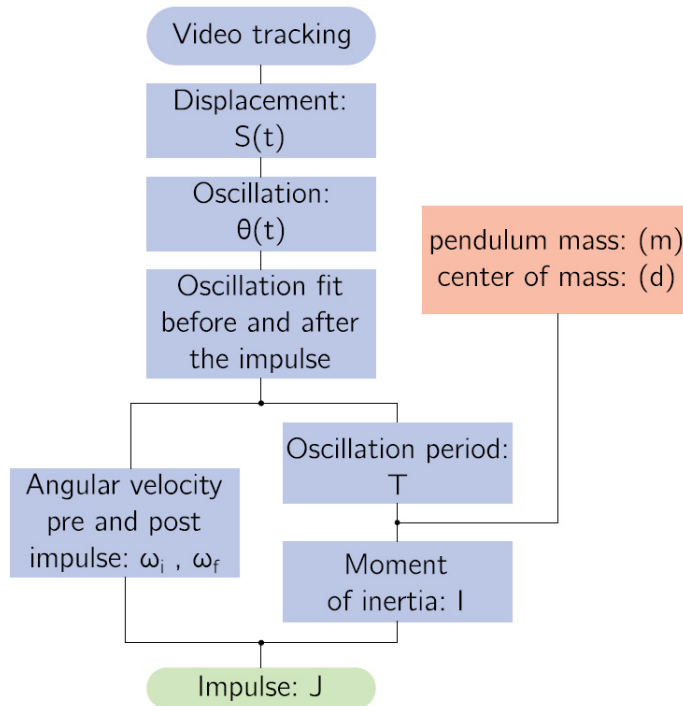


Figure 3.8: Flowchart of the analysis.

that the reflected spot moves on an uniform background and can be easily tracked. A complication is however introduced by the fact that the probe laser passes through a hole in the scale, so that diffraction rings appear in the reflected spot, as visible in Figure(3.9,b). These rings clearly increase the diameter of the reflected spot, affecting the tracking operation, therefore four lights are added around the scale so that only the more intense central spot is visible. As a consequence the intensity of the white background is not constant throughout all the scale, making it impossible to locate the black lines on it by simply using a threshold on the intensity of the pixels. In order to extract the scale from the frames of the video a different procedure was therefore developed. Its main steps are summarized in Table(3.1).

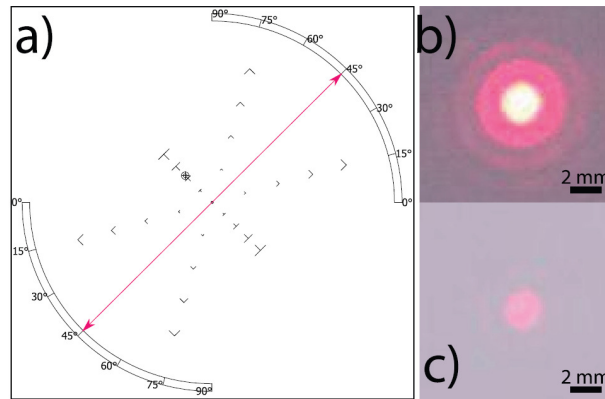


Figure 3.9: **a)** Graduated scale in which the reflected probe laser spot moves; **b)** Reflected probe laser without external illumination, diffraction rings are visible; **c)** adding an external illumination diffraction rings are no more visible.

Description	Result
<p>Initial intensity distribution of a single frame, obtained when averaging intensities of red, green and blue. The non uniform intensity of the white background is clearly visible, as well as the probe laser peaks.</p>	<p>A 3D surface plot showing the intensity distribution. The vertical axis is labeled 'intensity' and ranges from 0 to 250. The horizontal axes are labeled 'pixel' and range from 0 to 2000. A color bar at the top indicates intensity values from 40 to 220. The surface shows a central peak and a surrounding region of lower intensity, with some noise visible.</p>
<p>A running intensity threshold moves from the maximum to the minimum intensity of the white background. For each threshold a boolean picture is obtained like the one on the right, for an intermediate threshold. Note that a single large white region is present.</p>	<p>A binary (boolean) image showing the result of a thresholding operation. The image is mostly white, with a few small black regions. The white region is roughly circular and contains some internal structure, including a small black spot at the bottom center.</p>

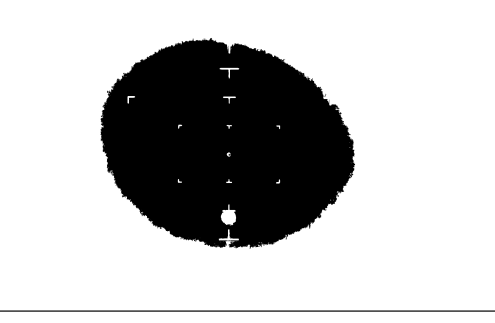
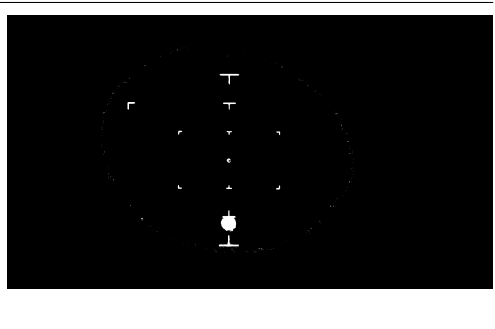
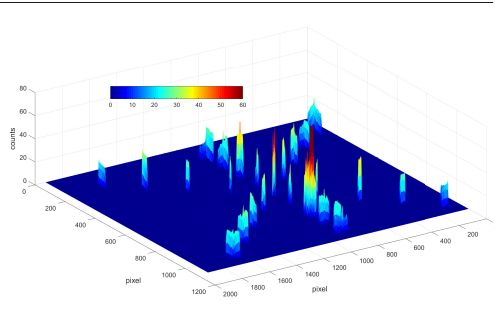
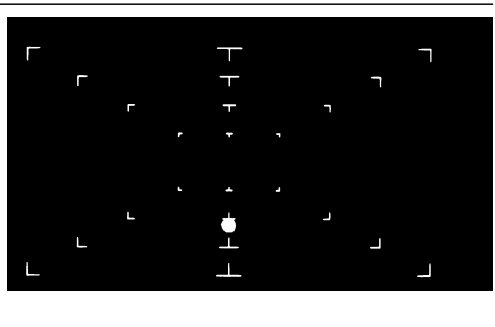
<p>The negation of the previous image gives returns the lines of the scale that are visible as separated regions, and also large white region on the borders is obtained. Using only a single intensity threshold would give a similar result in scale extraction.</p>	
<p>The large white region on the borders is removed.</p>	
<p>Boolean images like the previous one, obtained for each intensity threshold, are summed so that an histogram in which each peak represents a black line is obtained. Here a threshold can be easily applied on the counts.</p>	
<p>A boolean image of the scale is finally obtained. Distances on the scale are then calibrated by counting the number of pixels between two lines at known distance.</p>	

Table 3.1: Procedure for scale extraction from a frame of the recorded video.

As clear from Table(3.1) a single threshold allows to extract only a part of the scale lines, excluding in particular those farther from each other that allow to reduce uncertainty on the calibration. Moreover using a single threshold value makes calibration sensitive to variation in illumination of the graduated scale that depends also on other light in the laboratory and nearby windows, other than the four light positioned there on purpose. Light coming from the windows in particular is variable, so that white intensity on the scale may change during the day and depending on the external weather, so that the effect of a single intensity threshold would change, from a measure to another. The procedure presented here instead exploits a moving threshold, whose maximum and minimum value depend on the overall white intensity distribution of the frame, so that variations are taken into account.

Once the distances on the scale are calibrated, the motion of the reflected probe laser spot can be easily tracked by using an intensity threshold, since intensity of both incoming and reflected beams is much higher than the white background. Figure(3.10) shows an example of the tracked motion of the reflected spot. The displacement of the reflected spot is always measured with respect to the central incoming beam, by considering the center of mass of the regions identified by the threshold. As visible no damping is observed for the recorded time of free pendulum oscillation both before and after impulse, that lasts roughly 2 s, and also the impulse instant is clearly visible.

Before concluding this discussion on tracking the uncertainty in the obtained displacement of the reflected spot has to be considered. Sources of error in this case comes from the measure of the distance in meters between the lines of the scale, the fluctuation in their distance in pixel measured during the calibration process and the fluctuation in the size in pixel of the incoming and reflected probe beams as measured during tracking. The overall effect of all these uncertainty sources leads to an error of ~ 1 mm on the measured displacement of the reflected spot.

3.3.2 From displacement to pendulum motion

Pendulum motion is related to the displacement of the reflected probe laser through the geometry of the experiment. The probe laser hits the pendulum coming from the vertical direction, being aligned by means of a plumb line, then it is reflected back on the scale in a position that depends on the

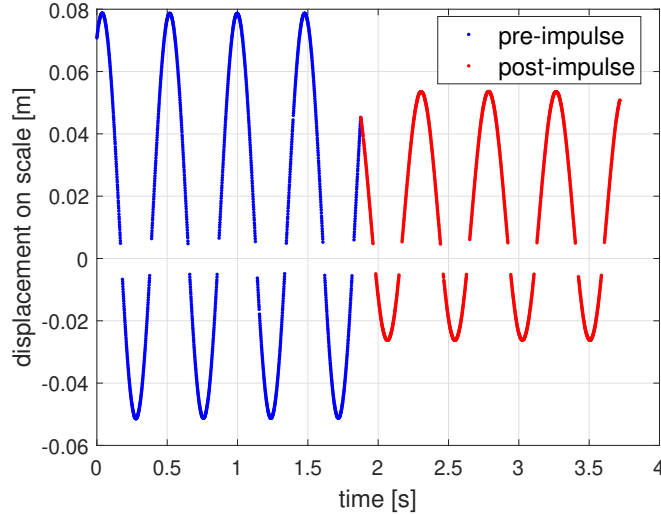


Figure 3.10: Tracked motion of the reflected probe laser spot in time. Different motion before and after impulse are clearly visible, while the region around zero displacement is due to the superposition of the incoming and reflected probe beams.

position of the mirror. As can be observed in Figure(3.4) the mirror is positioned above the fulcrum tips by a distance l , so that the rotation axis of the pendulum doesn't pass through it. Moreover the probe laser not always hit the mirror vertically above the fulcrum, but a displacement Δx may be present.

The description of the optical path of the probe laser is therefore more complex, as presented in Figure(3.11,a) considering also a deflection of the incoming probe laser by an angle δ from the vertical. Following the optical path of Figure(3.11,a) the displacement of the reflected spot is related to the

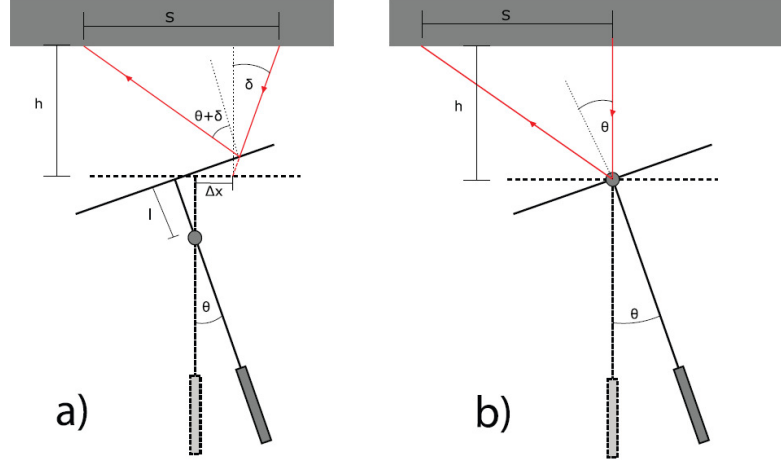


Figure 3.11: **a)**realistic geometry of the experiment; **b)**approximated geometry of the experiment.

oscillation angle θ of the pendulum by the following relation

$$S = h \tan(2\theta + \delta) - L \left[\sin\left(\frac{\pi}{2} - \delta\right) \tan(2\theta + \delta) + \cos\left(\frac{\pi}{2} - \delta\right) \right] + h \tan \delta \quad (3.7)$$

$$L = \left[\left(l \sin\left(\frac{\theta}{2}\right) \right) + \left(\Delta x + 2l \sin\left(\frac{\theta}{2}\right) \right) \tan \theta \right] \left[\cos \delta + \frac{\sin \delta}{\tan\left(\frac{\pi}{2} - \theta - \delta\right)} \right] \quad (3.8)$$

However the realistic situation of Figure(3.11,a) can be approximated considering $l, \Delta x, \delta = 0$ obtaining the situation in Figure(3.11,b), because of the small oscillations of the pendulum, usually smaller than 1° . In this case displacement of the reflected spot is related to θ by

$$S = h \tan(2\theta) \quad (3.9)$$

The validity of this approximation can be verified by assuming some upper limits for $l, \Delta x, \delta$ and comparing $S(\theta)$ obtained with equation (3.8) and (3.9). Using $l = 10 \text{ mm}$, $\Delta x = 1 \text{ mm}$, $\delta = 0.1^\circ$ a difference in reflected probe displacement of $\sim 10^{-1} \text{ mm}$ is obtained considering the same oscillation angle:

a value smaller than the uncertainty on displacement previously estimated.

Equation (3.9) can therefore be used to compute the oscillation angle of the pendulum from the displacement of the reflected probe laser, presenting also the additional advantage of being analytically invertible, while equation (3.8) is not.

3.3.3 Analysis of pendulum motion

After using equation (3.9) pendulum oscillations in time are known, as visible from Figure(3.12). The next step consists then in analysing this motion in

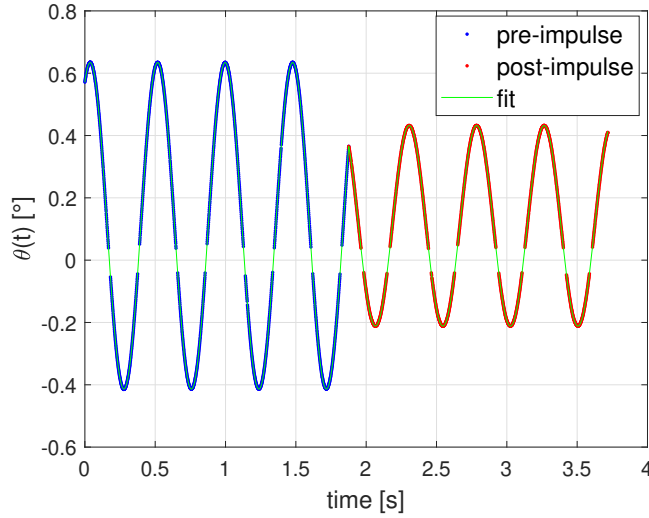


Figure 3.12: Oscillations of pendulum in time, as computed from displacement in Figure(3.10). As visible these oscillations are very well fitted by equation (3.10).

order to obtain the exact instant of impulse generation, t_{imp} , angular velocity of the pendulum before and after impulse, and its period. This motion is described by

$$\begin{cases} \theta_i(t) &= \theta_{0,i} \sin(\Omega_i t + \phi_i) + \text{offset}_i & \text{for } t < t_{imp} \\ \theta_f(t) &= \theta_{0,f} \sin(\Omega_f t + \phi_f) + \text{offset}_f & \text{for } t > t_{imp} \end{cases} \quad (3.10)$$

Angular velocity and period can be easily obtained by fitting the oscillations, however the variation in angular velocity caused by the impulse requires the knowledge of t_{imp} : the first step of the analysis is then to estimate it. By the synchronization of the camera with the shutter t_{imp} is known to be in a wide time interval of about 0.5 s around the central part of the video; a fit of the pendulum motion before and after it can be made anyway excluding this interval. A new narrower time interval in which impulse occurred is then estimated by looking at the difference of the sampled motion with the two fits before and after t_{imp} . In this way the new extremes t_{min} and t_{max} of the interval are defined when the difference between fit and sampled motion overcomes a threshold. A fine measurement of t_{imp} can then be made by solving the following equation

$$\theta_f(t) - \theta_i(t) = 0 \quad t_{min} < t < t_{max} \quad (3.11)$$

The uncertainty on t_{imp} obtained with this procedure can be estimated by errors on fit parameters and is usually ~ 1 ms, comparable with time separation of two consecutive frames of the recorded video. It is worth noting however that, thanks to the optimal reduction of damping of the pendulum and of all other external vibrations, its motion is almost ideal so it is extremely well fitted by equation (3.10) with very small uncertainties. For this reason error on t_{imp} is often of a few hundreds of μ s, or even less.

Once t_{imp} and all the other fitting parameters are known, angular velocity of the pendulum before ($\omega_{pre}(t)$) and after ($\omega_{post}(t)$), can be easily obtained by deriving equation (3.10). Then the variation in angular velocity caused by the impulse is given by $\Delta\omega = |\omega_{post}(t_{imp}) - \omega_{pre}(t_{imp})|$, with the absolute value considered because the pendulum can be hit either in phase or counter phase.

To obtain impulse now moment of inertia and distance of irradiated spot from rotation axis have to be measured, as required by equation (3.4). The measurement of these parameters is described in the next section.

3.4 Measurement of mass parameters of the pendulum

As discussed at the beginning of this chapter, a physical pendulum oscillates with a period given by (eq. 3.1)

$$T = \frac{2\pi}{\Omega} = 2\pi \sqrt{\frac{I}{mgd}} \quad (3.12)$$

In order to measure moment of inertia I , as required to obtain the generated mechanical impulse, equation (3.12) can be exploited once oscillation period T , the distance of center of mass from rotation axis d and mass m of the pendulum are known. Given the complex geometry of the pendulum, the different materials that compose it and the different mass of the target material used for every measurement, a calculation of the center of mass of the pendulum would be difficult. An additional obstacle on this approach comes from the fact that the exact mass distribution of the 3D printed PLA frame is not known, because some unwanted voids may appear on the inside during the printing process.

The best approach is then to measure the position of the center of mass. This can be done by exploiting the fact that when an object is suspended on a point and is free to oscillate, in its equilibrium position its center of mass lies on the vertical direction passing through the suspension point. Considering then two different suspension points, the intersection of the two vertical lines passing through these points when the object is in each of these equilibrium positions gives the location of its center of mass. This procedure was employed for the pendulum as presented in Figure(3.13). A blade edge is used as suspension point and two random parts of the plastic frame of the pendulum are chosen to suspend it. Image analysis is then used to track the vertical directions in the two different equilibrium position and to intersect them: this requires to acquire a picture of the suspended pendulum in each equilibrium position, an example is visible in Figure(3.14). In order to reduce parallax effects the picture is acquired from a distance of more than 2 m, and is made so that details of pendulum, the suspension point and the vertical direction given by a plumb line are well visible. These two pictures are analysed separately to track the vertical direction passing through the suspension point, distances are also calibrated using a known length of the pendulum. The two images are then "superimposed" in order to find the intersection of the

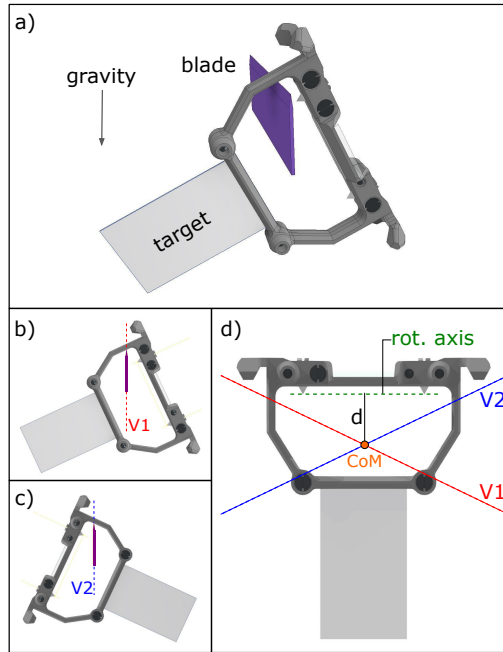


Figure 3.13: Procedure for the measurement of the position of the center of mass (CoM) of the pendulum.

two vertical directions, that is the center of mass position, and its distance from the rotation axis is measured. It is important to note here that in doing this operation it is crucial to consider that different calibration of distances may be present in the two pictures, since the pendulum is moved to change suspension point.

Depending on the pendulum and on the target fixed on it, the distance of center of mass from the rotation axis d is in the range $6 \div 10$ mm. An uncertainty on this value can be estimated by simply repeating the measurement for the same pendulum, in this way an error in the order of $10 \mu\text{m}$ is obtained: a value surprisingly small for such a simple measurement.

As visible from Figure(3.14) laser spots are clearly visible on the picture acquired for the measurement of center of mass position. It is therefore easy to measure from these pictures also the distance of irradiated spot from the rotation axis r , needed for calculation of generated impulse.

The moment of inertia of the pendulum can be estimated at this point

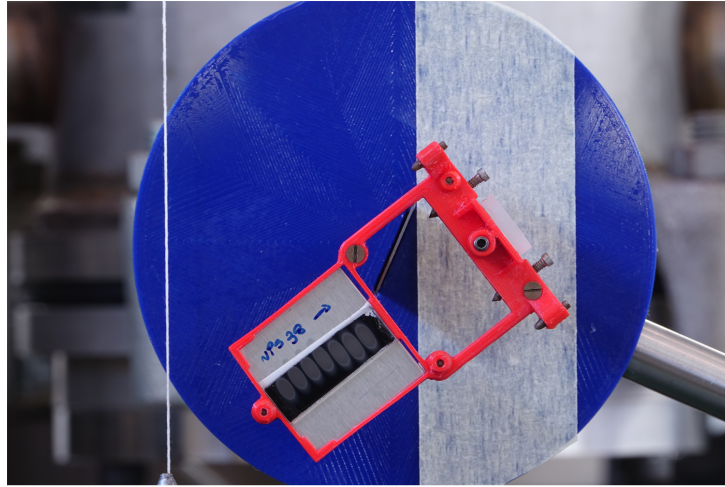


Figure 3.14: Picture used for image analysis to measure the position of center of mass of the pendulum.

by exploiting equation (3.12), where the total mass m is measured with a scale with 10^{-4} g resolution. Commonly obtained values obviously depend on the pendulum and are $\sim 3 \text{ kgmm}^2$ for the heavy one and $\sim 0.4 \text{ kgmm}^2$ for the light one, in both cases uncertainty is of the order of 10^{-2} kgmm^2 .

3.5 Test of the performances of the apparatus

To conclude the description of this apparatus for laser generated impulse measurement, a test on its performances is presented and compared with literature data.

3.5.1 Damping

Before moving to impulse measurement, damping of the pendulum must be checked. This is done by generating on the pendulum the highest possible impulse, in order to obtain the maximum amplitude of oscillation. The motion of the pendulum is then recorded until oscillations become sufficiently small, and amplitude in time is considered as presented in Figure(3.15). Damping of oscillations is explained by two different friction mechanisms. For wide

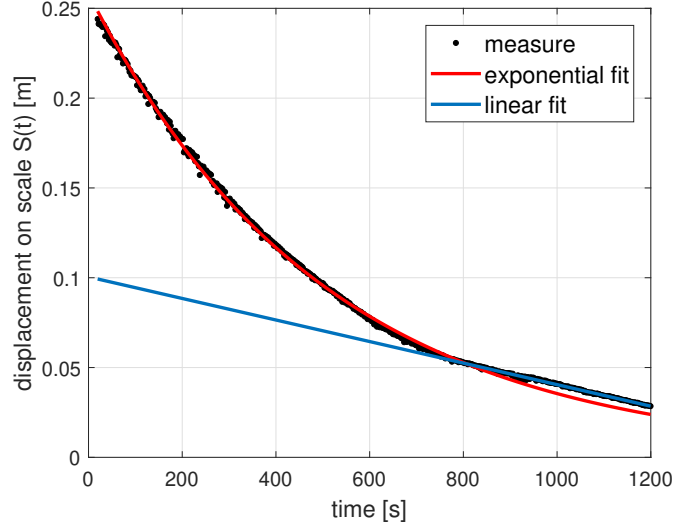


Figure 3.15: Damping of oscillations in time. Red and blue lines represent respectively the exponential and linear fit.

oscillations higher angular velocities are present, so that viscous damping is present; when amplitude becomes sufficiently small dry damping[17] due to the mechanical friction of the fulcrum tips appears instead. As visible, while viscous damping gives an exponential decay of amplitude, linear decreasing is caused by dry damping. The damping curve is therefore fitted according to equation

$$\begin{cases} S_{max}(t) = S_0^{exp} \exp\left(-\frac{t}{\tau}\right) & S_{max} > 5 \text{ cm} \\ S_{max}(t) = S_0^{lin} - ct & S_{max} < 5 \text{ cm} \end{cases} \quad (3.13)$$

Exponential fit	Linear fit
$S_0^{exp} = 0.26 \text{ m}$	$S_0^{lin} = 0.1 \text{ m}$
$\tau = 504 \text{ s}$	$c = 6 \times 10^{-5} \text{ m s}^{-1}$

Table 3.2: Fitting parameters of oscillation damping.

Fitting parameters, presented in Table(3.2), show that typical damping times are much longer than the expected duration of free oscillation of the pendulum in a measurement, which is of about 2 s. This allows to treat the

pendulum as non damped during data analysis, as presented previously.

3.5.2 Impulse measurement

To test the performances in impulse measurement Aluminum was chosen as a standard material, to have a better comparison with literature. Moreover coupling coefficient C_m is considered instead of impulse, since it is the most commonly measured parameter and is independent of other experimental parameters, like laser spot area for instance.

To test the uncertainty on impulse (and consequently C_m) measurement a series of repeated measurements was made by keeping constant the laser output energy at a value of $490 \pm 10\text{mJ}$. The obtained results are visible in Figure(3.16). The average value of C_m is $20.6 \pm 0.3 \mu\text{N s J}^{-1}$, with the

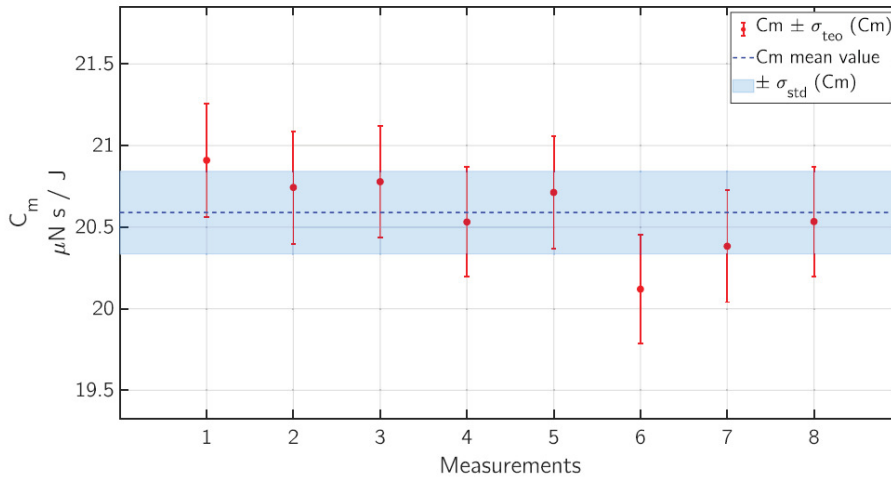


Figure 3.16: C_m values obtained from a repeated measurement on aluminum. Error bars as computed by propagating errors are presented in red, while standard deviation is presented as light blue region.

uncertainty obtained from the standard deviation of the measurements, a value that is also comparable to that obtained by error propagation. The reproducibility of this measurement shows that even if the exact instant of the impulse generation can not be chosen, so that the pendulum can be hit both in phase or counter phase and with any angular velocity, this is all taken

into account by the analysis.

A precise comparison of this result with similar measurements in literature is difficult, because even if the same material is considered different laser wavelengths, pulse duration and pressure are employed. Nevertheless, it is possible to say that C_m obtained here is in good agreement with other works in literature[14, 10, 6].

A comparison with the uncertainties presented for other apparatus in literature allows to assess the performance of this apparatus in terms of reproducibility of the results. In general, uncertainty in C_m for other apparatus is reported to be around 10% [11] while in this case an uncertainty of 1% is obtained. This result can be mainly attributed to the specifically designed pendulum, to the reduction of damping and to the system and analysis for the detection of pendulum motion.

3.5.3 Ablated mass measurement

The final test is on the measurement of the ablated mass. As previously described this measurement can be made exploiting the automated motion of a large target in the chamber, while the laser irradiates it at a given frequency. In this measurement the same laser parameters of C_m measurement are used, and the target is irradiated with a repetition rate of 3 Hz, that allow to irradiate a region different than that ablated with the previous pulse. The mass of the target is measured before irradiation and after a sufficiently large number of pulses, with a scale with 10^{-5} g resolution, so that the ablated mass per pulse can be obtained.

In this case the target was irradiated with 12616 pulses, causing a total mass loss of 9.60 ± 0.02 mg, that correspond to 0.761 ± 0.002 μ g/pulse. Since laser fluence is the same than that used for impulse measurements also a specific impulse $I_{sp} = 930 \pm 8$ s can be computed, and can be compared with other literature results on the same material. Due to the difficulty in obtain a measure of ablated mass, usually I_{sp} is through the velocity of ejected products; this approach however generally results in too large values[18]. With respect to other works[4, 18] I_{sp} obtained here is roughly a factor of 2 smaller, but again there are many differences in the experimental conditions. Uncertainty obtained here on the other hand is about one order of magnitude smaller than that reported in these works, mainly due to the reduced error in impulse measurement and to the possibility to use a large number of pulses while moving the target.

To conclude this discussion a final remark on the estimation of laser fluence is needed. In order to test performances of this apparatus the main interest was only to keep it as constant as possible in order to be able to repeat the measurements: this only requires to keep laser output energy constant and not to change optics.

An accurate measurement of laser fluence however requires much more care, in particular the spatial distribution of laser intensity can have drastic effects in ablation and lead to errors in fluence estimation. This will be described in detail the next chapter.

Bibliography

- [1] Claude Phipps, Mitat Birkan, Willy Bohn, Hans-Albert Eckel, Hideyuki Horisawa, Thomas Lippert, Max Michaelis, Yuri Rezunkov, Akihiro Sasoh, Wolfgang Schall, Stefan Scharring, and John Sinko. Review: Laser-ablation propulsion. *Journal of Propulsion and Power*, 26(4):609–637, 2010. doi: 10.2514/1.43733.
- [2] Claude R. Phipps. *Laser Ablation Propulsion and Its Applications in Space*, pages 217–246. Springer International Publishing, Cham, 2018. ISBN 978-3-319-96845-2. doi: 10.1007/978-3-319-96845-2_8.
- [3] Andrew J. Jamison, Andrew D. Ketsdever, and E. P. Muntz. Gas dynamic calibration of a nano-newton thrust stand. *Review of Scientific Instruments*, 73(10):3629–3637, 2002. doi: 10.1063/1.1505096.
- [4] Andrew V. Pakhomov, M. Shane Thompson, Wesley Swift, and Don A. Gregory. Ablative laser propulsion: Specific impulse and thrust derived from force measurements. *AIAA Journal*, 40(11):2305–2311, 2002. doi: 10.2514/2.1567.
- [5] B V Lakatosh, D B Abramenko, V V Ivanov, V V Medvedev, V M Krivtsun, K N Koshelev, and A M Yakunin. Propulsion of a flat tin target with pulsed co2 laser radiation: measurements using a ballistic pendulum. *Laser Physics Letters*, 15(1):016003, dec 2017. doi: 10.1088/1612-202x/aa94ea. URL <https://doi.org/10.1088/1612-202x/aa94ea>.

- [6] Soojin Choi, Tae-hee Han, Ardian B Gojani, and Jack J Yoh. Thrust enhancement via gel-type liquid confinement of laser ablation of solid metal propellant. *Applied Physics A*, 98(1):147–151, 2010.
- [7] C. R. Phipps, M. Boustie, J.-M. Chevalier, S. Baton, E. Brambrink, L. Berthe, M. Schneider, L. Videau, S. A. E. Boyer, and S. Scharring. Laser impulse coupling measurements at 400 fs and 80 ps using the luli facility at 1057nm wavelength. *Journal of Applied Physics*, 122(19):193103, 2017. doi: 10.1063/1.4997196.
- [8] Matej Senegačnik, Matija Jezeršek, and Peter Gregorčič. Propulsion effects after laser ablation in water, confined by different geometries. *Applied Physics A*, 126(2):1–12, 2020.
- [9] Pietro Battocchio, Jacopo Terragni, Nicola Bazzanella, Claudio Cestari, Michele Orlandi, William Jerome Burger, Roberto Battiston, and Antonio Miotello. Ballistic measurements of laser ablation generated impulse. *Measurement Science and Technology*, aug 2021. doi: 10.1088/1361-6501/abace6.
- [10] Brian D’Souza and Andrew Ketsdever. *Direct Impulse Measurements of Ablation Processes from Laser-Surface Interactions*. 2005. doi: 10.2514/6.2005-5172.
- [11] Claude Phipps and James Luke. Diode laser-driven microthrusters: A new departure for micropropulsion. *AIAA Journal*, 40(2):310–318, 2002. doi: 10.2514/2.1647.
- [12] Joshua B. Sloane and Raymond J. Sedwick. Direct force measurement of pulsed laser ablation of asteroid simulants. *Journal of Propulsion and Power*, 36(4):551–559, 2020. doi: 10.2514/1.B37566.
- [13] Kevin Kremeyer, John Lapeyre, and Steven Hamann. Compact and robust laser impulse measurement device, with ultrashort pulse laser ablation results. *AIP Conference Proceedings*, 997(1):147–158, 2008. doi: 10.1063/1.2931886.
- [14] DucThuan Tran, Akifumi Yogo, Hiroaki Nishimura, and Koichi Mori. Impulse and mass removal rate of aluminum target by nanosecond laser ablation in a wide range of ambient pressure. *Journal of Applied Physics*, 122(23):233304, 2017. doi: 10.1063/1.5005584.

- [15] J.M. Fishburn, M.J. Withford, D.W. Coutts, and J.A. Piper. Study of the fluence dependent interplay between laser induced material removal mechanisms in metals: Vaporization, melt displacement and melt ejection. *Applied Surface Science*, 252(14):5182–5188, 2006. ISSN 0169-4332. doi: <https://doi.org/10.1016/j.apsusc.2005.07.053>. URL <https://www.sciencedirect.com/science/article/pii/S0169433205010536>.
- [16] Pietro Battocchio, Jacopo Terragni, Vito Cristino, Nicola Bazzanella, Riccardo Checchetto, Michele Orlandi, Stefano Caramori, and Antonio Miotello. Poly (vinyl chloride) coupling with uv laser radiation: Comparison between polymer absorbers and nanoparticles to increase efficiency for laser ablation propulsion. *The Journal of Physical Chemistry C*, 125(51):28088–28099, 2021. doi: <https://doi.org/10.1021/acs.jpcc.1c08175>.
- [17] L F C Zonetti, A S S Camargo, J Sartori, D F de Sousa, and L A O Nunes. A demonstration of dry and viscous damping of an oscillating pendulum. *European Journal of Physics*, 20(2):85–88, jan 1999. doi: 10.1088/0143-0807/20/2/004. URL <https://doi.org/10.1088/0143-0807/20/2/004>.
- [18] Andrew V. Pakhomov, M. Shane Thompson, and Don A. Gregory. Ablative laser propulsion: A study of specific impulse, thrust and efficiency. *AIP Conference Proceedings*, 664(1):194–205, 2003. doi: 10.1063/1.1582108.

Chapter 4

Role of beam homogeneity and laser fluence estimation

The discussion on laser ablation given in Chapter 2 highlighted how laser fluence plays a major role in determining the thermodynamic conditions reached in the irradiated region and the involved ablation mechanisms. This in turn affects the quantity of ejected mass and crater depth and, ultimately, impulse generation.

Fluence is therefore the parameter that is changed in order to study any property related to laser ablation, also in applications like propulsion and material synthesis. When comparing experiments with models, however, it must be considered that laser energy may not be deposited uniformly throughout the irradiated region, so that fluence estimation may not be straightforward.

4.1 Problems related to laser fluence

Laser fluence represents the surface energy density irradiated on the target material, as defined by relation (2.1). Experimentally it is then measured by dividing the energy of the laser pulse by the irradiated area. This procedure, despite being extremely simple, hides some issues that must be addressed to avoid critical behaviours in the results of the measurements, like those described in the following of the chapter.

Assuming that the energy of the laser pulse is well known, as it is easily the case by using a power or energy meter, the main problems are related to the

spatial distribution of this energy inside the irradiated area, and also to how this area is measured. The spatial distribution of intensity at the output of a laser is rarely uniform, but it can be described in the majority of the cases as a gaussian[1] or, in the case of older excimer lasers, with not-so-well defined shapes[2, 3, 4, 5]. This fact is strictly related to the strategy employed to measure the area of the irradiated region, which is often done by measuring the area of the region modified by the laser pulse.

Considering now that laser-induced surface modification is a threshold process, it is easy to understand that if the laser pulse is not uniform but presents some tails, the modified region will become dependent both by the employed material, and by the pulse energy. As an example, if for a given material and pulse energy an area A_0 is obtained, increasing pulse energy or lowering surface modification threshold (by changing material), will result in $A_1 > A_0$. In other words measuring the irradiated area by looking at the traces left by the laser pulse on a given material corresponds to taking a slice of the laser pulse spatial distribution at a given energy, defined by the material itself. The irradiated area is therefore not uniquely defined.

The positive side of these facts is that, if spatial distribution of laser pulse energy is well known, surface modification threshold can be measured with a single pulse by measuring the irradiated area[1]. Moreover strategies have been explored to somehow alleviate this problem, consisting in irradiating many times the same region or by measuring the modified region for increasing pulse energy until it saturates to an almost constant value[6].

Even after the definition of an irradiate region some other difficulties appear: energy distribution inside this area may in fact not be uniform, so that different ablation mechanisms can be present simultaneously. The fluence measured in this way can be described then as average of the local fluence $\Phi(x, y)$ inside the irradiated area A , that can be written as

$$F = \frac{E}{A} = \frac{1}{A} \int_A \Phi(x, y) dx dy \quad (4.1)$$

where E is the measured laser pulse energy. In some parts of the irradiated region the measured value F can be much different than the actual value $\Phi(x, y)$, so that it is not representative of the physical situation. This means that even if a value of F below the expected threshold is measured, in some part of the irradiated region, reasonably the central one, this threshold may be overcome so that ablation occurs.

Moving further in this direction, the difference between the measured fluence

F and $\Phi(x, y)$ leads also to discrepancies when the same F is obtained using different combinations of pulse energy and irradiated area. In fact, while the measured F is the same, local fluence $\Phi(x, y)$ may be very different from one case to another so that different mechanisms are observed. Since, when looking at some observed behaviour as function of fluence the average value F is considered, discrepancies appear in the measure.

Impulse measurements are particularly sensitive to this problem, as will be described in detail in this chapter. In an ideal situation, where the same fluence is present in all the irradiated region and $F = \Phi(x, y)$ for all x, y , the same ablation mechanisms and exhaust velocities can be expected at any point. If in this condition an impulse J_0 is measured by irradiating an area A_0 , changing the irradiated area to A_1 by keeping the same fluence will result in an impulse J_1 such that $\frac{J_1}{J_0} = \frac{A_1}{A_0}$. In other words, the generated impulse per unit area remains the same.

If this ideal condition is not met a change in irradiated area without changing the measured fluence F will result in discrepancies in the measurement of impulse per unit area and, consequently also on C_m .

It appears clearly now that a spatial energy distribution as uniform as possible is a fundamental requirement for the study of propulsion performances of materials, both to have coherent measurement and to have an accurate knowledge of the physical conditions of the material during irradiation.

4.2 Non-uniform beam energy distribution

In the case of excimer lasers non-uniform distributions are present with a wide area of few cm^2 .

To measure the energy distribution in the output beam the knife-edge method was employed: a slit at the output of the laser was gradually open in both in the horizontal and vertical direction with steps of 1 mm, and for each step pulse energy was measured. To measure pulse energy a power meter was used, with the laser operating with a pulse repetition rate of 10 Hz. Given the initial instability of laser output energy, the measure started once a stable readout was observed, and consisted average power over 20 s. The obtained result is presented in Figure(4.1). The energy distribution in the laser beam presents some evident tails and can be considered constant only in a very

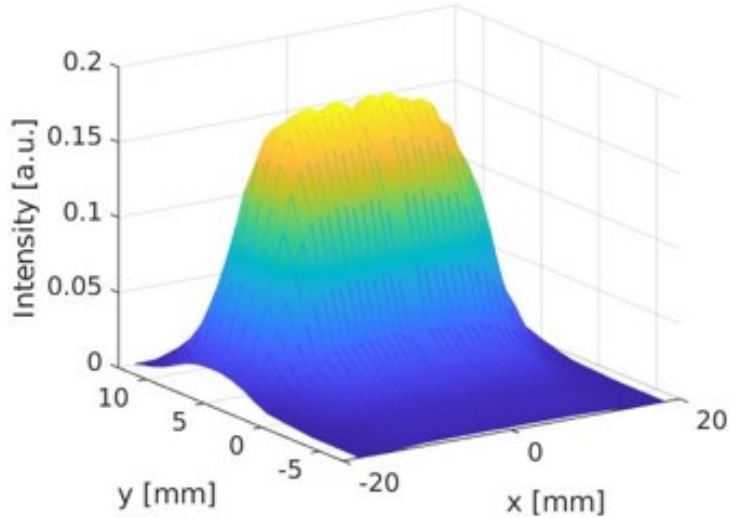


Figure 4.1: Beam intensity profile at laser output.

narrow region at the maximum of the distribution.

4.2.1 Measurement of energy deposited on target

The optical path of the laser initially considered included a set of slits positioned at the output in order to cut the tails in the external part of the beam, and to restrict it to an area of roughly $3 \times 1 \text{ cm}^2$. The beam is then turned by 90° by a mirror and directed toward the chamber, passing through a plano-convex lens and a window, both made by fused silica.

All these elements reduce the laser energy that is deposited on the target material, so that it can be considerably different from that measured at the output. Losses due to the optical path of the laser are then obtained by measuring pulse energy both at the laser output and after all optical elements. Again pulse energy is obtained from the average power measured with the laser operating with a repetition rate of 10 Hz. Energy losses are constant in the range of possible output energies of the laser, between 200 and 600 mJ. These values constitute then a calibration for laser energy reaching the target, that in this way can be measured from energy at output, an operation that do not require to move lenses and windows and is therefore more reliable. Moreover the energy that effectively reaches the target, E_{eff} is the

one that is used in equation (1.7) to compute C_m .

4.2.2 Measurement of the irradiated area

While measurement of energy losses is straightforward, this is not the case for the estimation of the irradiated area. As previously mentioned, this measurement is made by looking at the modifications left on a clean surface, but the area of this region may depend both on the material and on pulse energy. Here aluminum is used as a material both for impulse measurement and to estimate the irradiated area, being a common material in space applications. To estimate the irradiated area a different number of consecutive pulses was irradiated at a fixed energy and the generated craters were successively examined with SEM. The same procedure was repeated for different energies. Figure(4.2) shows an example of the obtained craters with an energy on tar-

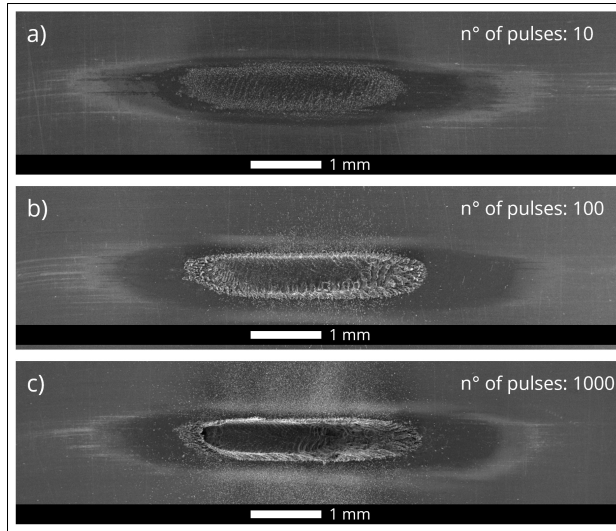


Figure 4.2: Laser spots obtained with an increasing number of consecutive pulses at a repetition rate of 10 Hz, and a deposited energy of about 250 mJ/pulse.

get $E_{eff} \simeq 300$ mJ, with the target tilted by 45° with respect to the laser direction and positioned at a distance of 230 mm from a lens with 250 mm focal length. Some features are clearly evident: first of all it is not possible to identify a sharp border that separates the modified and the clean region,

this may be a consequence of both the presence of tails in the laser pulse or of heat diffusion, and doesn't allow to define a clear maximum value for the irradiated area. Moreover, it is possible to find three differently modified regions inside the crater, whose separation becomes better defined by increasing the number of laser pulses. Starting from the already mentioned external part, this can be attributed to the effects of high temperature reached in that region, that is however not sufficient to reach melting. All the inner part of the crater on the other hand shows signs of melting, but it is possible in any case to identify in it other two regions: one in which signs of melt displacements are visible, and the central one in which a real crater is present, due to phase explosion.

The presence of different concentric laser-modified regions clearly indicates the presence of tails in the laser beam intensity and do not allow the unique definition of an irradiated area. One possible choice consists in considering the region that most probably contains the majority of the pulse energy, in other words, exclude the effect of tails. This is obviously a non rigorous procedure, but at least gives a rule to coherently measure spot area for different distances of the target from the focus of the lens.

4.2.3 Impulse measurement

Impulse generation must depend on the rate of mass ejection during laser ablation. Since laser ablation is a fluence dependent phenomenon, when laser pulse energy is not uniformly distributed, a different fluence is present in different parts of the irradiated area. This of course leads to different ablation mechanisms and different ablation rates occurring simultaneously, all of them contributing to impulse generation.

A first experiment to investigate this behaviour was conducted considering different irradiated areas, obtained by changing the distance of the target from the lens from 250 mm (focus) to 210 mm, and changing the pulse energy at the output of the laser from 200 to 600 mJ. The target is always kept tilted by 45° with respect to beam direction. Fluence is therefore changed here both by changing laser energy and spot area.

Figure(4.3) shows mechanical impulse generated for the different considered spot areas as a function of the effective energy on target. As expected, for a fixed area, impulse grows for increasing E_{eff} since fluence is increased. For a fixed E_{eff} fluence is increased also by reducing the irradiated area, as indicated, but in this case the fact that generated impulse grows by reducing

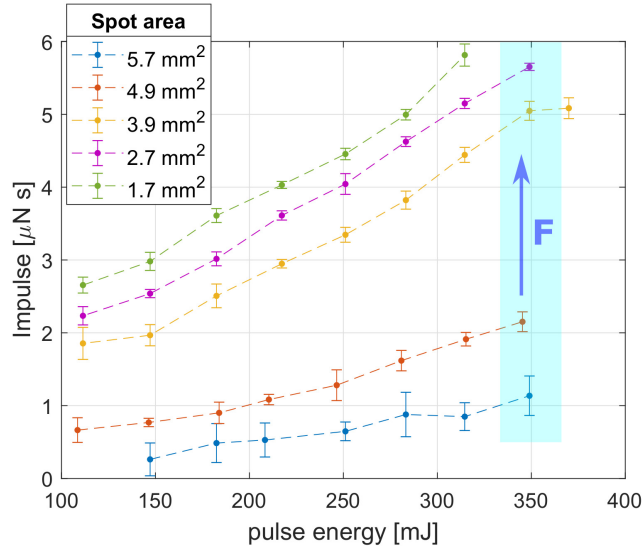


Figure 4.3: Impulse generated as a function of laser energy on target for different spot areas.

spot area requires more discussion. In this case in fact there are two opposite effects related to the reduction of the spot area: on one side fluence is increased, so that impulse should increase as previously discussed, on the other side the area from which mass is ejected is smaller, resulting in a reduced impulse generation. The measured mechanical impulse is therefore a trade off between these two opposite trends. As clear from Figure(4.3) the effect of increased fluence appears to be predominant with respect to the reduced emission area, since for a fixed E_{eff} impulse grows by reducing spot area.

The effect of the non uniformity of the beam becomes evident when considering more in detail the effect of irradiated area on impulse generation. Figure(4.4) shows generated impulse per unit area as a function of fluence, where discrepancies are visible between curves corresponding to different spot areas. A step-like behaviour appears, showing that for the same laser fluence a higher impulse per unit area is measured when the irradiated area is smaller. This suggests that, due to the non-uniformity of beam, its central part becomes much more intense than the external one with focusing, so that ablation becomes more efficient in it. Since the measured fluence represents the average energy density deposited on the irradiated area, this value can be much more different than both the intense central part and the external tails,

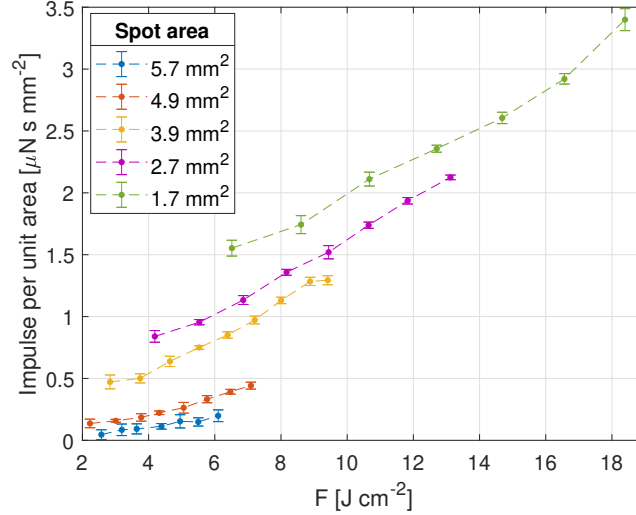


Figure 4.4: Generated impulse normalized by the irradiated area as a function of measured laser fluence.

becoming non representative of the real physical situation. As an additional effect, laser fluence in the central part of the spot may become sufficiently high to overcome phase explosion threshold, so that mass ejection increase and consequently also generated impulse. This possibility is confirmed by observing the low fluence part of Figure(4.4) where three different areas can be compared for the same estimated fluences: a general agreement is observed in the case of the two larger areas, where also in the central part of the beam fluence is reasonably not sufficient to reach phase explosion; on the other hand by focusing more the laser beam measured impulse becomes higher, due to the onset of phase explosion in the central part of the beam. From this observation it may appear that the onset of phase explosion results in a step in impulse generation. However, it is worth noting that this step in the generated impulse per unit area must be related also to the fraction of the area in which this occurs, since it is visible for all the smaller areas in which reasonably phase explosion covers a larger fraction. A similar behaviour is obviously obtained by computing the coupling coefficient C_m from the previous measurement, as visible in Figure(4.5). Here the fact that, for a fixed fluence, focusing laser beam into a smaller area results in an higher C_m , suggests that energy efficiency in impulse generation increase by reduc-

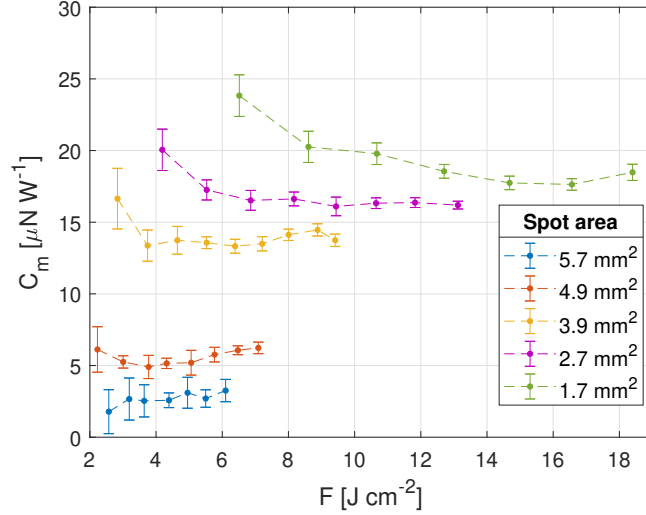


Figure 4.5: C_m as a function of measured laser fluence.

ing the irradiated area. This observation can be explained recalling again that laser ablation, and in particular phase explosion, is a threshold process. Defocusing the laser beam in a larger area an increasing part of pulse energy is distributed in the tails of beam, where fluence is lower than the ablation threshold, so that this part of energy is somewhat wasted in a temperature increase that does not lead to ablation.

It is clear at this point that if laser pulse energy is not uniformly distributed in the irradiated area C_m is not uniquely defined by fluence, but it also has some dependence on the way the beam is focused. To proceed further in this discussion it is now worth considering what happens when fluence is changed by keeping a fixed focusing distance, but changing the irradiated area by tilting the target with respect to the direction defined by the incoming laser beam. In this way the energy distribution in the laser pulse is never changed, but is projected on the target at different angles.

Figure(4.6) shows impulse measurements made at fixed pulse energies and distance of the target from the lens, as a function of the tilting angle with respect to the laser beam direction. Here $\theta = 0^\circ$ means that laser beam irradiates normally to target surface. Calling A_0 the irradiated area at $\theta = 0$

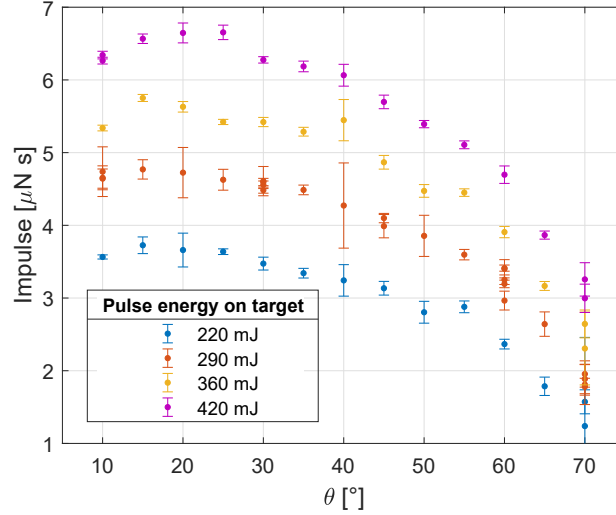


Figure 4.6: Impulse generated as a function of tilting angle of the target, for different laser pulse energies on target.

°, the area of the projected beam will increase with tilting angle as

$$A(\theta) = \frac{A_0}{\cos \theta} \quad (4.2)$$

therefore for constant pulse energy fluence will be reduced and consequently also generated impulse, as visible. It can be also noted however that generated impulse does not reach a maximum when $\theta = 0^\circ$ and fluence is maximum, but it decreases for $\theta < 20^\circ$. This is a consequence of a well known effect called *plasma shielding*, that consists in the partial absorption of the incoming laser beam by the generated plasma plume, that becomes more evident for incidence angles close to normal because of the longer optical path of the laser in the plume.

Also in this case measured impulse can be observed as a function of laser fluence, where irradiated area is estimated according to equation (4.2). Again, since spot area changes for each point, impulse must be normalized for it, as shown in Figure (4.7)

Impulse per unit area, as expected, shows the same discrepancies observed in Figure(4.4) since in this case the n-th point of each curve corresponding to a different energy (different colour), has the same irradiated area. Another feature to note in this case is that, due to plasma shielding effect, the high

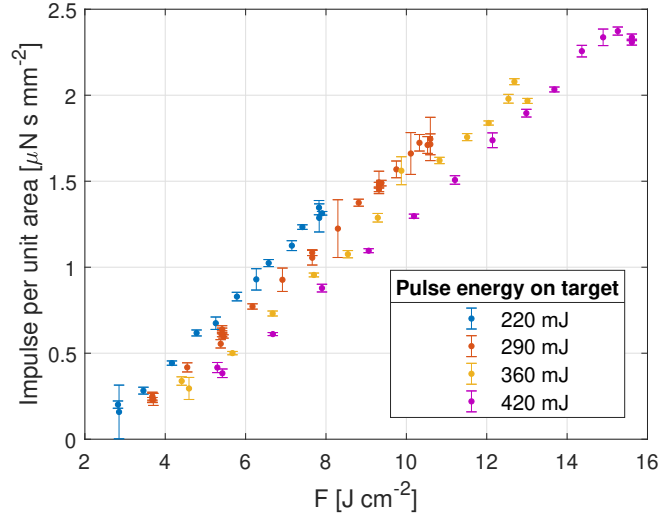


Figure 4.7: Impulse per unit area as a function of laser fluence, when area is changed by tilting the target with respect to the laser beam.

fluence part of each curve shows a decrease in generated impulse.

A non-uniform spatial distribution of energy deposited in the irradiated area then does not allow to assign a unique generated impulse value to a given fluence. This mostly depends, as mentioned, by the fact that the measured fluence is an average value of the energy density inside the irradiated area, but in case of non uniform distributions may be much different from the actual local fluence value. Moreover also the area over which this average is computed is often not well defined, so measured fluence may be in a sense dependent on how ablation craters are interpreted. It is therefore advisable to consider an intensity distribution that is as close as possible to being uniform, in order to confirm that the discrepancies here observed are effectively due to a non uniform irradiation.

4.3 Uniform energy distribution

An interesting possibility to shape intensity distribution of a laser beam is given by the use of a diffractive optical element (DOE), also called beam homogenizer[7]. These optical devices take advantage of computer optimiza-

tion and microfabrications techniques available nowadays to obtain a desired intensity profile. In general, once the final intensity distribution is chosen, the pattern that has to be fabricated on the DOE is computed through some optimization algorithms[8, 9] so that in principle it is possible to obtain almost any intensity distribution.

The most common applications of these optical elements consists in generating a flat-top intensity profile. The same is done in this work, starting from the intensity profile presented in Figure(4.1) and obtaining a circular spot with an almost constant intensity profile, as presented in Figure(4.8).

Differently from the non uniform intensity distribution previously consid-

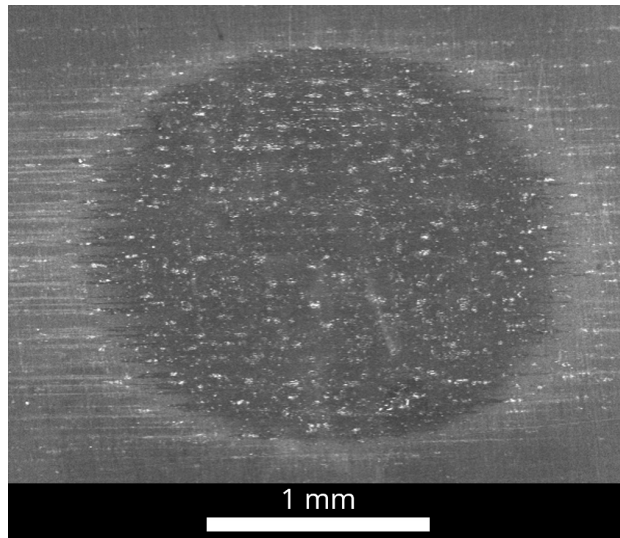


Figure 4.8: Laser spot obtained after 10 consecutive pulses at 10 Hz.

ered, the introduction of the beam homogenizer requires that the target is always positioned in the focus of the used lens, because the uniform intensity profile is obtained only in this position. The area of the circular spot depends on the focal length of the optical system, so that a longer focal length gives a larger irradiated area and vice versa. In order to investigate the role of the irradiated area in impulse generation two different lenses are therefore used, with 200 mm and 300 mm focal length, that produce respectively spots of area 5.8 mm^2 and 14.2 mm^2 . Figure(4.9) shows impulse per unit area generated in this configuration and the corresponding coupling coefficient.

The step-like behaviour visible in Figure(4.4) and Figure(4.7) is now elim-

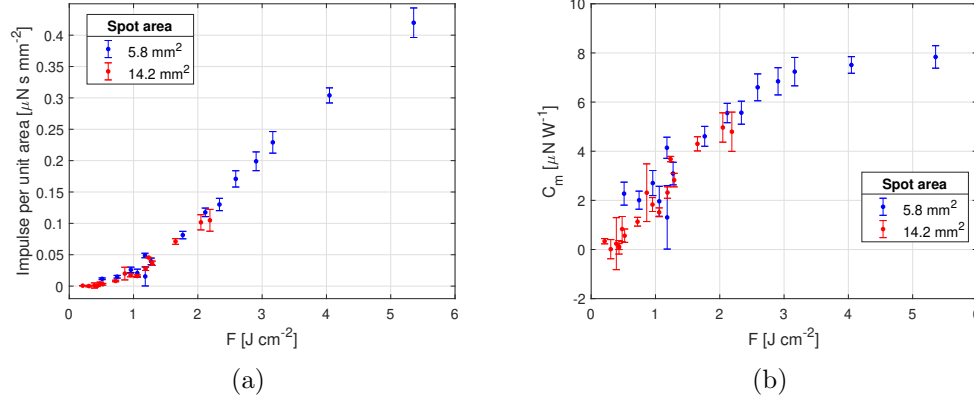


Figure 4.9: a) Impulse per unit area as a function of fluence; b) C_m as a function of fluence.

inated, proving that this problem is related to the non-uniformity of the beam intensity profile. The same behaviour is obviously reflected in C_m , presented in Figure(4.9,b), that reaches a plateau at about 5 J/cm^2 . It is interesting to note here that, despite the effect of the uniformity of the spot has been proven with these measurements, the C_m values obtained with a non-uniform intensity distribution are higher and in better agreement with literature[10, 11, 12]. This again suggests that non-uniform intensities distributions are used in this kind of measurements and is also confirmed by observing in Figure(4.5) that C_m obtained with larger areas, that have more uniform intensity distribution, is similar to that obtained in this case.

4.4 Optimal configuration for systematic measurements on materials

Once uniformity of beam energy distribution has been proven to be fundamental in order to investigate material properties related to impulse generation, it is important to point out what is the best strategy to change laser fluence during the measurement.

Even if fluence can be changed by exploiting different combinations of pulse energy and irradiated areas, in order to reduce the number of parameters the best practice is to keep constant one of them. As said, when using a

beam homogenizer a different lens is needed each time spot area has to be changed, becoming quite limiting. Pulse energy on the other hand can be easily changed in fine steps. Moreover in general an accurate measurement of pulse energy is easier than the measurements of the spot area, due to the previously discussed issues. For these reasons for the measurements presented in the following chapters spot area is kept constant and only pulse energy is changed.

Pulse energy at the output can be changed in the range $200 \div 600$ mJ, but this interval can be easily extended towards lower energies by using some filters. As often done for excimer lasers a set of metallic meshes was employed to reduce the energy deposited on the target, as presented in figure(4.10).

These metallic meshes are positioned at the output of the laser and act as

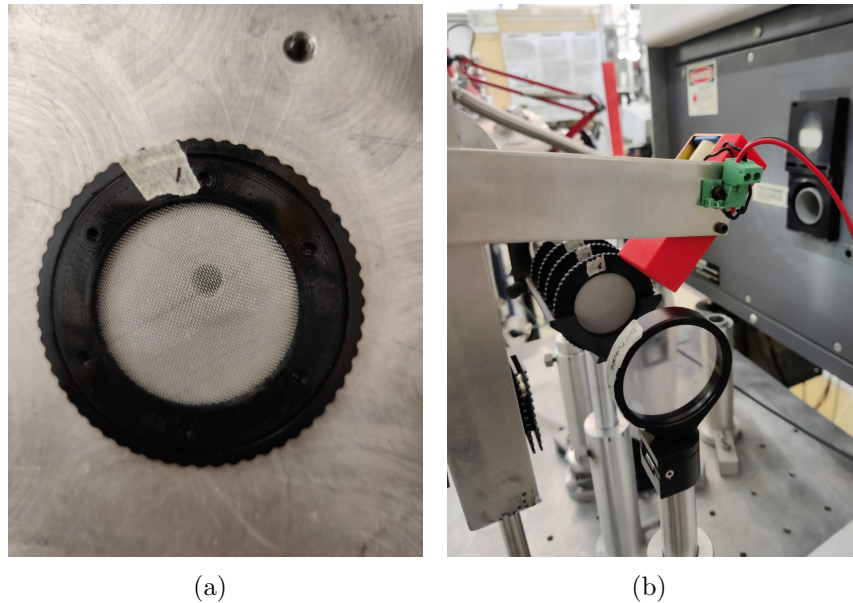


Figure 4.10: a)Picture of a metallic mesh filter; b)Picture showing the set of four metallic mesh filters and the beam homogenizer.

mask for the beam. Meshes with two different fractions of covered areas are used, roughly 50% and 30% of free area. It is important to note that in all cases both apertures of the meshes or their wires have typical dimensions of hundreds of μm , so that no interference is observed. A total of four filters is used, so that energy on the target can be changed from about 10 mJ up

to about 350 mJ (without filters, only losses due to optics). To know the exact energy on target a calibration is needed, and is done for each different combination of filters by measuring energy at the output of the laser and after all the optical path, as previously described.

Bibliography

- [1] Rusty W. Conner and Dana D. Dlott. Time-resolved spectroscopy of initiation and ignition of flash-heated nanoparticle energetic materials. *The Journal of Physical Chemistry C*, 116(28):14737–14747, 2012. doi: 10.1021/jp303077f.
- [2] P. Parvin, B. Jaleh, H.R. Zangeneh, Z. Zamanipour, and Gh.R. Davoud-Abadi. Excimer laser beam profile recording based on electrochemical etched polycarbonate. *Radiation Measurements*, 43:S617–S622, 2008. ISSN 1350-4487. doi: <https://doi.org/10.1016/j.radmeas.2008.03.046>. Proceedings of the 23rd International Conference on Nuclear Tracks in Solids.
- [3] Klaus R. Mann, A. Hopfmueller, P. Gorzellik, R. Schild, Werner Stoffler, Hans H. Wagner, and Gerhard E. Wolbold. Monitoring and shaping of excimer laser beam profiles. In James M. Darchuk, editor, *Laser Energy Distribution Profiles: Measurement and Applications*, volume 1834, pages 184 – 194. International Society for Optics and Photonics, SPIE, 1993. doi: 10.1117/12.143853. URL <https://doi.org/10.1117/12.143853>.
- [4] Yuhua Jin, Ali Hassan, and Yijian Jiang. Freeform microlens array homogenizer for excimer laser beam shaping. *Opt. Express*, 24(22):24846–24858, Oct 2016. doi: 10.1364/OE.24.024846.
- [5] Jacopo Terragni, Pietro Battocchio, Nicola Bazzanella, Michele Orlandi, William J. Burger, Roberto Battiston, and Antonio Miotello. Evaluation of the role of beam homogeneity on the mechanical coupling of laser-ablation-generated impulse. *Appl. Opt.*, 60(31):H37–H44, Nov 2021. doi: 10.1364/AO.432991.
- [6] Hisashi Tsuruta, Oskar Dondelowski, Yusuke Katagiri, Bin Wang, and Akihiro Sasoh. Ablation spot area and impulse characteristics of poly-

- mers induced by burst irradiation of 1 μ m laser pulses. *Acta Astronautica*, 136:46–54, 2017. ISSN 0094-5765. doi: <https://doi.org/10.1016/j.actaastro.2017.03.006>.
- [7] HoloHor Website, 2022. URL <https://www.holoor.co.il/product/diffusers/>.
- [8] Weidong Qu, Huarong Gu, Qiaofeng Tan, and Guofan Jin. Precise design of two-dimensional diffractive optical elements for beam shaping. *Appl. Opt.*, 54(21):6521–6525, Jul 2015. doi: 10.1364/AO.54.006521.
- [9] Nikolay L. Kazanskiy, Victor V. Kotlyar, and Victor A. Soifer. Computer-aided design of diffractive optical elements. *Optical Engineering*, 33(10):3156 – 3166, 1994. doi: 10.1117/12.178898.
- [10] Hisashi TSURUTA, Bin WANG, Zhogyuan WANG, and Akihiro SASOH. Influence of microscopic crater formation on impulse generated with repetitive pulsed laser ablation. *TRANSACTIONS OF THE JAPAN SOCIETY FOR AERONAUTICAL AND SPACE SCIENCES, AEROSPACE TECHNOLOGY JAPAN*, 13:33–36, 2015. doi: 10.2322/tastj.13.33.
- [11] Katsuhiko Tsuno, Satoshi Wada, Takayo Ogawa, Toshikazu Ebisuzaki, Tadanori Fukushima, Daisuke Hirata, Jun Yamada, and Yuki Itaya. Impulse measurement of laser induced ablation in a vacuum. *Opt. Express*, 28(18):25723–25729, Aug 2020. doi: 10.1364/OE.399119.
- [12] Chenghao Yu, Weijing Zhou, Hao Chang, and Yifu Chen. Experimental research on impulse coupling characteristics and plasma plume dynamics of a nanosecond pulsed laser irradiated aluminum target. *IEEE Access*, 8:205272–205281, 2020. doi: 10.1109/ACCESS.2020.3037302.

Chapter 5

Impulse generation by PVC: comparison between carbon nanoparticles and polymers as absorbers.

Laser ablation of polymers is characterized by a wide variety of possible ejected products, due to the very different structures and decomposition paths possible for these materials. Compared to metals, polymers that have high absorption in specific wavelength ranges show much lower ablation thresholds, moreover since ablation proceeds by decomposition heavier products are ejected.

From the point of view of propulsion, these features make polymers good candidates to obtain high energetic efficiency (C_m) in the impulse generation process. Another feature that make polymers a category of materials attracting for LAP is their low thermal conductivity, that allows to reach conditions for impulse generation even with very long pulses up to ms[1], that can be obtained by very small diode lasers[2, 3, 4].

Polymers tested for impulse generation are generally chosen either because they are easy to purchase, like for example PVC, PVN, PVA[5, 4], or because they show an intense exothermic decomposition like GAP. Other experiments have been performed also on specifically designed photopolymers[5]. Among commercial polymers PVC proved promising performances in terms of higher C_m and I_{sp} [5, 2], becoming a sort of benchmark material for these kind of measurements. PVC shows very low optical absorption for wavelengths

longer than 200 nm, so commonly carbon nanoparticles (CNPs) are introduced to increase its interaction with the laser. While in the case of PVC optical absorption is increased by using CNPs, a most common strategy to enhance laser ablation of polymers exploits the use of dye molecules or another polymer that act as chromophore[6, 7, 8, 9, 10]. Using a dye, the same absorption is present in all the sample; on the other side, using nanoparticles localized absorption centers are created, while the surrounding polymer matrix remains transparent.

It is therefore of interest to investigate the differences of these two different absorption mechanisms in impulse generation. In particular, since polymers are attractive in LAP for the high C_m , the energetic efficiency in the impulse generation process obtained with these two absorption mechanisms must be discussed.

This gives useful information about relevant material properties for LAP, pointing at strategies for the development of new, specifically designed materials.

In the following of this Chapter, PVC containing CNPs (PVC+CNPs), which is a common LAP material, will be compared with PVC mixed with poly(styrene sulfonate) (PVC:PSS) in order to clarify the role of localized or uniform absorption in the impulse generation process. The comparison will be made from the energetic point view, considering the thermodynamical parameters that play a role in laser ablation and the impulse generated by these materials.

5.1 Sample preparation

5.1.1 Materials

For this experiment commercial PVC precursor(Sigma-Aldrich, powder, average $M_w \sim 43000$, average $M_n \sim 22,000$) and CNPs (carbon black, Sigma-Aldrich, nanopowder, particle size < 500 nm, purity $> 99.95\%$) are used, as well as cyclohexanone, a good solvent for PVC. On the other hand PSS was prepared in order to make it soluble in cyclohexanone too. PSS monomer has negative charge, so a counter ion is needed in the material to have neutrality, the preparation then started with commercial NaPSS (poly(sodium 4-styrene-sulfonate), $M_w \sim 7000$, Sigma-Aldrich) that is non-soluble in cy-

clohexanone because of the Na^+ ion. This ion is therefore substituted with tetrabutylammonium (TBA^+) to obtain solubility. To do this HPSS is initially obtained by precipitation of NaPSS in strongly acidic conditions by adding HCl dropwise until complete precipitation was observed, then HPSS is collected on a filter and thoroughly washed with water. This polymer is then suspended in water and TBAOH is added until neutral pH is obtained and TBAPSS is dissolved. Finally TBAPSS is obtained after complete drying. For simplicity TBAPSS will be called PSS in the following.

5.1.2 Preparation procedure

Samples for impulse measurements on polymers are films, that must be thick enough to resist the ablation process without breaking and with a uniform surface structure, so that reproducible measurements are possible. The easiest way to obtain a polymer film containing CNPs is to start from a polymer solution and deposit it on a substrate. Although this method, called *solution casting*, easily allows to produce thick films, its main drawback is that non uniform surfaces are obtained. Moreover, due to the very long evaporation times, if also nanoparticles are present in the solution they may precipitate so that also a non uniform dispersion is present.

To solve this problems the *spin coating* technique was used instead. This technique consists in dropping the solution on a rotating substrate, so that it is uniformly dispersed in a layer whose thickness depends on spinning velocity and viscosity of solution. This method is usually employed for the production of thin films, but it has the main advantages to generate uniform surfaces and require short evaporation times. A multilayer procedure was therefore developed to obtain thick films by spin coating having uniform surface and good CNPs dispersion, as described in the following.

To prepare the solutions of PVC+CNP, PVC is dissolved in cyclohexanone. The solution is prepared by adding the polymer to the solvent, then stirring for a few hours and successively leaving it in a ultrasonic bath for another few hours. The concentration of PVC in cyclohexanone determines the viscosity of the solution, which is a fundamental parameter for the film fabrication by spin coating. Since the goal is to produce thick films, a viscous solution containing 20 wt% PVC in cyclohexanone is used. The desired quantity of CNPs is added to the PVC solution once the polymer is completely dissolved and it appears as a transparent fluid.

The solution of PVC:PSS is obtained in a slightly different way, due to the difficulty of disperse PSS in the viscous PVC solution. In this case a given amount of PSS is initially dissolved in cyclohexanone by a few minutes ultrasonic bath, then PVC is added in order to obtain 20 wt% concentration and is dissolved as described above. Table(5.1) lists the prepared solutions.

absorber [g]	concentration [wt%]	sample name
0	0	PVC
0.04	1	PVC+1wt%CNPs
0.20	5	PVC+5wt%CNPs
2.06	34	PVC:PSS(66:34)
1.25	23	PVC:PSS(77:23)
0.69	15	PVC:PSS(85:15)

Table 5.1: Quantity of absorbers contained in 4 g of PVC, corresponding concentration and name of the samples.

In order to obtain thick films by spin coating a multilayer procedure was developed, as presented in Figure(5.1). This procedure allows to obtain thick films with uniform surface and with short evaporation times, so that no precipitation of CNPs occurs, and is based on the successive deposition of spin coated layers. Each layer is deposited through a two steps process. In the first step the solution is deposited either on the substrate or on the previously deposited layer, and then rotation starts at 300 RPM for 480 s. During this time, which is longer than usual duration for a spin coating procedure, the polymer solution is uniformly dispersed in a thick layer because both of its high viscosity and low spin velocity. At the end of the first step the central part of the film is partially dried, but some solution gathers on the borders and in particular on the corners of the substrate, so that a non uniform, wet region is present around the center. To solve this problem a second spin coating step starting immediately after the first is employed, lasting 60 s with spinning velocity of 1000 RPM, that removes the still wet solution on the borders of the film, reducing the non uniform region.

In order to be able to deposit the following layer, the deposited polymer film must be sufficiently dry so that the successive rotations doesn't remove it, therefore after each deposition the film is partially dried for 30 min at 40 °C. One fundamental feature of this procedure is that it allows to obtain thick

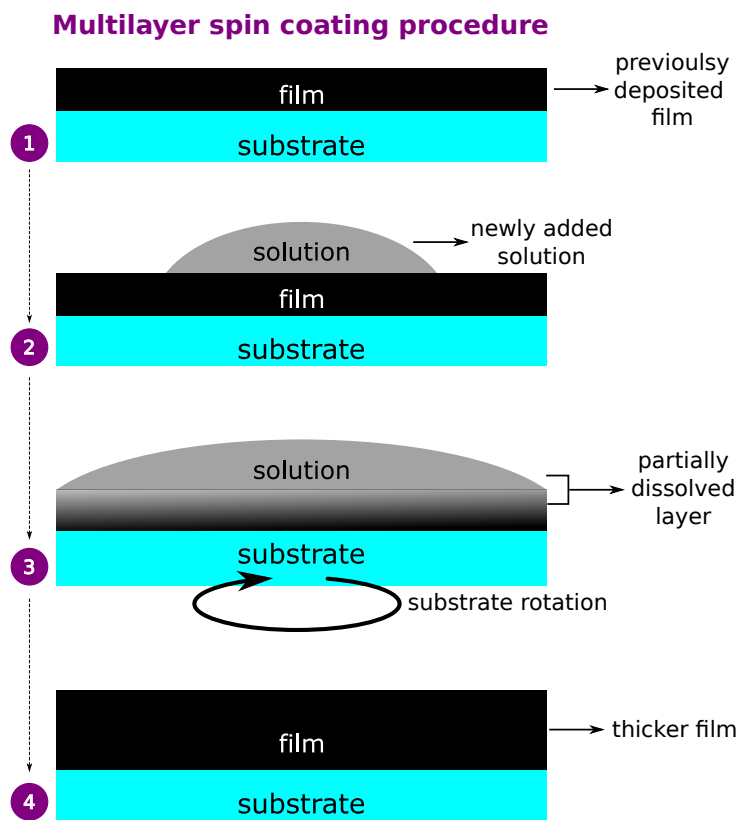


Figure 5.1: Scheme of the employed multilayer spin coating procedure.

films by superimposing successive layers that are mixed through the dissolution of the interface so that single bulky layer is obtained. This happens because when new solution is dropped on a previously deposited polymer layer it is partially dissolved so that at the end of the two spinning steps a single thicker layer is obtained, as depicted in Figure(5.1). Of course an important requirement for this procedure is that the previous layer must be sufficiently thick, in order to avoid its total dissolution. Another feature of this procedure is that the thickness of the film does not grow linearly with the number of layers, probably because flowing of the new solution over an already deposited layer is more difficult, since a very viscous solution is present at the interface where the previous layer is dissolving.

Once the desired number of layers has been deposited, the film is dried for 3 h at 80 °C. As discussed more in detail later, this drying procedure still leaves

some solvent traces in the samples, but these don't affect impulse generation. A different number of layers is used depending on the measurement: a film with a single layer, with a thickness of about 10 μm is used for optical absorption measurements, while a more robust film made with three layers and a thickness of about 50 μm is used for impulse measurement.

5.2 Characterization

5.2.1 Sample structure

The structure of the prepared polymer films is studied by means of Scanning Electron Microscopy (SEM), observing in particular their cross section. This allows to check the presence and dispersion of CNPs in the polymer matrix and also the absence of interfaces between the spin coated layers. To obtain a clear cross section of the films, they are cut inside liquid nitrogen, in order to obtain a fragile fracture without deformations.

Figure(5.2) presents images of cross sections obtained on different samples, and with different numbers of layers. Figure(5.2,a) shows the cross section of a neat PVC film, composed by five superimposed layers, where it clearly appears that no interfaces are visible and also uniform surfaces are present, at least on this scale. The same observations hold also in case of Figure(5.2,b,d) where three layers are deposited and CNPs and PSS are respectively included in the sample. A sample containing CNPs is presented in Figure(5.2,b,c), here CNPs of typical size ~ 500 nm are clearly visible as embedded in the PVC matrix and uniformly dispersed throughout all the thickness. Moreover no cluster are observed, confirming the goodness of the procedure of solution preparation and film deposition. Finally Figure(5.2,d) shows a sample of PVC:PSS, where no different regions corresponding either to PVC or PSS are observed, suggesting that the two polymers are homogeneously mixed.

5.2.2 Differential Scanning Calorimetry (DSC)

Differential Scanning Calorimetry (DSC) is a commonly used characterization technique for polymers, in particular to define the temperature of glass transition (T_g), melting (when present) and thermal decomposition. The idea at the base of this technique is to measure the difference in power to give to a reference furnace and to a furnace containing the sample needed

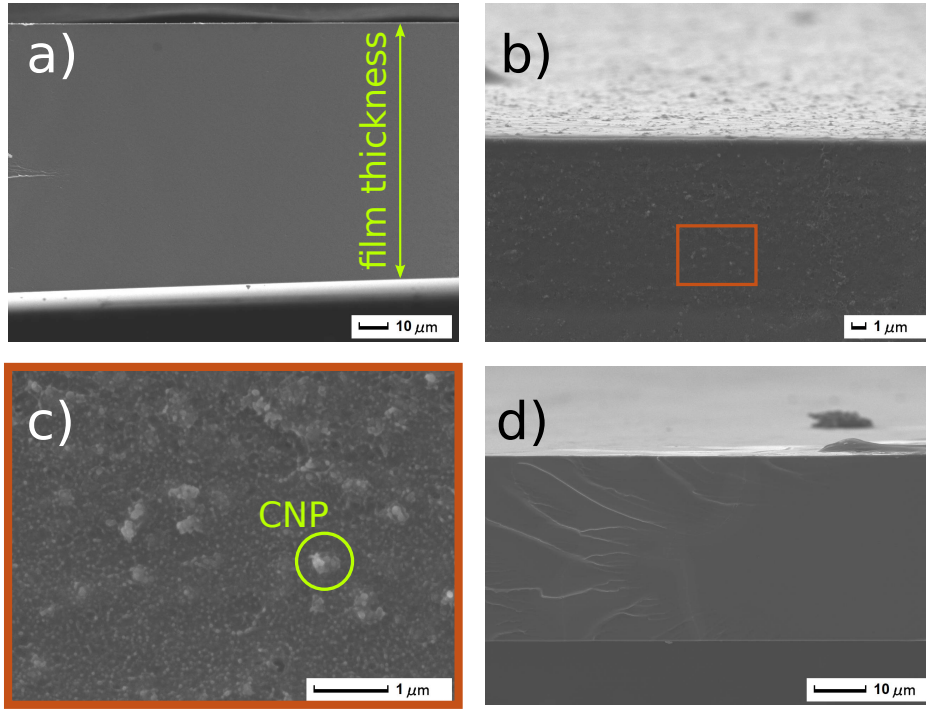


Figure 5.2: SEM images of cross section of the prepared polymer films. **a)** neat PVC film made successive deposition of five layers; **b),c)** three layer PVC+5wt%CNPs film; **c)** Three layer PVC:PSS film.

to make the same temperature ramp on both. For this reason, paying particular care at the measurement procedure, DSC is also a good technique to measure specific heat C_p . In fact C_p can be written as a function of the DSC output signal, which is an heat flow (HF), measured in W, the heating rate (HR) measured in K s^{-1} and the mass of the sample m . This is expressed by equation (5.1)

$$C_p = \frac{HF}{mHR} \left[\frac{\text{W}}{\text{gK s}^{-1}} \right] \quad (5.1)$$

Here DSC is exploited in particular to measure the C_p of the studied materials. Even if in principle C_p can be obtained from equation (5.1), particular care is needed to evaluate all the factors that may affect the measured heat flow. In particular it is found that the power difference measured to keep both reference and sample at the same constant temperature, changes with temperature because of the different importance of thermal losses.

A particular procedure called *two curve method* must then be used to keep this into account[11]. Each curve is acquired by keeping reference and sample at a constant initial temperature for a few minutes, then their temperature is increased at a given heating rate and finally they are kept at the final temperature for few minutes. The first of the two curves is a baseline, which is acquired by measuring the reference and the empty sample pan, the second curve is acquired with the reference and the sample.

When measurements are made on polymers, another good practice is to repeat the temperature ramp twice, separated by a controlled cooling step. This allows to release stresses created in the thermal treatment of sample preparation during the first run so that a clean measure is obtained in the second one.

Figure(5.3) shows the C_p as a function of temperature for the prepared sam-

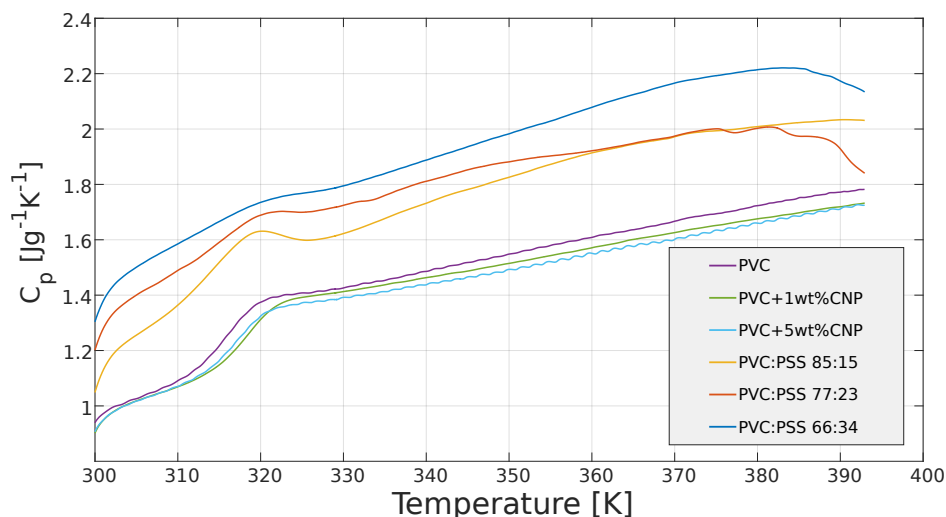


Figure 5.3: DSC measurement of specific heat of all the polymer samples.

ples, computed from equation (5.1) and using an heating rate of 5 K min^{-1} . PVC and all the samples of PVC+CNPs have the same C_p , since the mass fraction of CNPs in PVC is very small. In these curves it is also possible to see a step in C_p , corresponding to the glass transition of the polymer, at a temperature $T_g \simeq 315 \text{ K}$. This value is considerably lower than the expected one for PVC, which is about 355 K [12], due to the presence of solvent residues that act as plasticizer so that polymer chain can move more easily with respect to each other. Except for the position of the glass transition, the

obtained C_p is in good agreement with literature data[12]. In order to confirm that T_g reduction is due to sample preparation procedure, a DSC measure on the as received PVC powder is made, as presented in Figure(5.4), where the glass transition at the expected temperature is visible.

Higher C_p is instead observed in the case of PVC:PSS samples. Here it is pos-

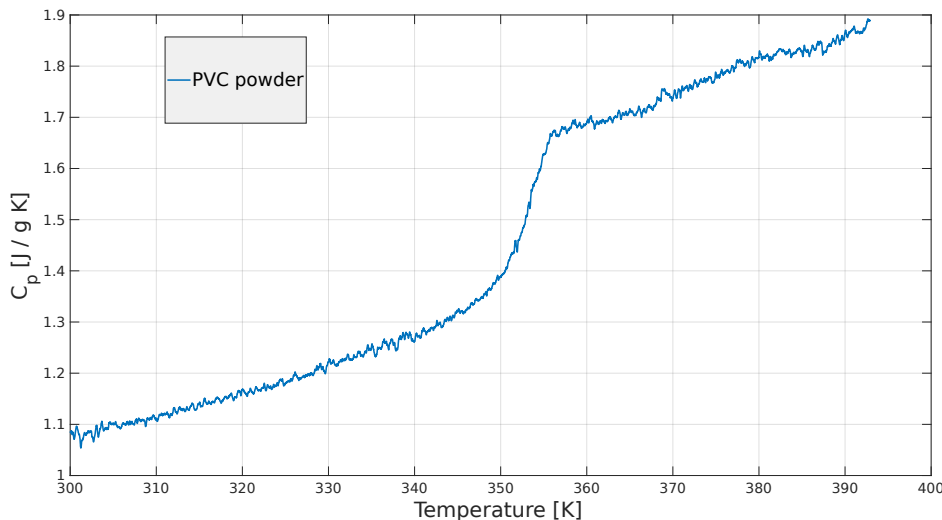


Figure 5.4: DSC measurement on the as received PVC powder, showing glass transition at the expected temperature.

sible to note that C_p grows with increasing PSS concentration and that again a step-like behaviour is observed at the same temperature of measured PVC glass transition. Another important observation about the measurements on PVC:PSS is that C_p starts to decrease at about 375 K. This suggests the initiation of an exothermic thermal decomposition of these materials, as confirmed also by thermal desorption spectroscopy measurements in the following. Since thermal decomposition of these polymers occurs during the measurements, the first DSC run is showed for PVC:PSS samples.

An additional DSC measurement is also made in order to confirm the presence of solvent residues in the samples and its effect as plasticizer, as presented on Figure(5.5). Another series of PVC+1wt%CNPs samples is prepared and dried at different temperatures ranging from 40 °C to 160 °C for 3 h. In this case heat flow is measured instead of C_p , since the interest is on the position of the glass transition. As clear from Figure(5.5) increas-

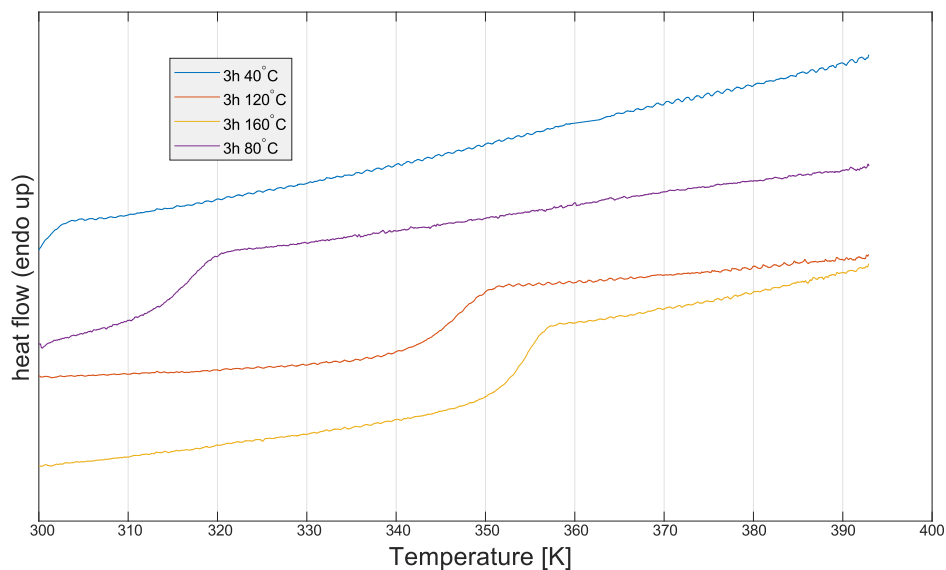


Figure 5.5: DSC measurement on PVC+1wt% dried at different temperatures.

ing drying temperature moves the position of the glass transition up to the expected value for PVC, since solvent residues are progressively released. No variations in glass transition temperature are instead observed when the sample is dried at the same temperature (80 °C) for times as long as one week, suggesting that solvent release is not a matter of diffusion in the sample but is a thermally activated process. An additional confirmation of these points comes also from thermal desorption measurements, giving also other information on the solvent release process.

5.2.3 Thermal Desorption Spectroscopy (TDS)

In thermal desorption spectroscopy (TDS) the sample undergoes a controlled increasing temperature ramp, while mass spectroscopy of the desorbed products is made. This kind of measurement allow then to observe the temperature at which a given molecule leaves the sample. In this case then it can be used to observe the possible solvent release and thermal decomposition of the polymer samples. In the case of PVC, the first step of its thermal decomposition is expected to occur at about 500 K[13]. Measurements here presented are performed using an heating rate of 0.4 K min^{-1} going from room

temperature up to temperatures slightly above the beginning of thermal decomposition, where the massive ejection of HCl saturates the spectrometer and might also damage the instrument.

Figure(5.6) shows TDS spectra for cyclohexanone and HCl. It is possible

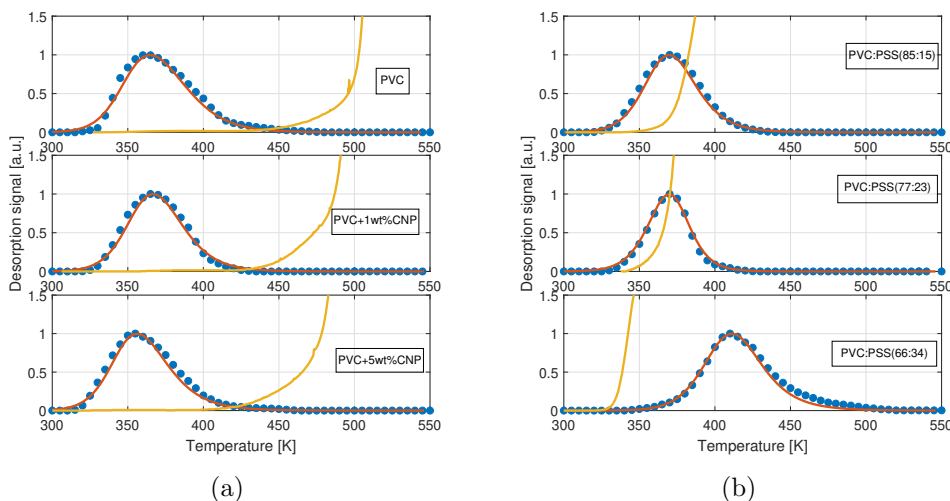


Figure 5.6: TDS measurements on all the samples. Dots indicate measurement on cyclohexanone desorption, red lines the corresponding computed desorption curve and yellow line the measurement on HCl release.

to see that a peak related to solvent released is observed for all the samples, roughly at the same temperature of 370 K and at slightly higher temperatures in the case of PVC:PSS(66:34). This of course confirms the presence of solvent residues inside the samples, even if it is not possible to make an estimation of the quantity. HCl release occurs at ~ 450 K for the neat PVC sample and for all the samples containing CNPs, showing again that this kind of absorbers doesn't affect thermal properties of the material. A different behaviour is instead observed in the case of PVC:PSS samples, where decomposition temperature is in general lower than that observed for neat PVC and also decreases with increasing concentration. This is particularly evident in the case of the most concentrated sample PVC:PSS(66:34), where HCl release starts before solvent release. This fact is in good agreement with the exothermic reaction observed in DSC measurements, and is due to the fact that TBA acts as a catalyst for PVC dehydrochlorination[14]. This fact will help in the comparison of the investigated materials from the point of

view of energy needed for thermal decomposition, as discussed further in this chapter.

From a more quantitative point of view, it is possible to fit the peak observed for cyclohexanone release, in order to give a description of the desorption process. Thermal desorption of cyclohexanone is in principle controlled by three processes: the release from the polymer sites where they are trapped, their migration to the film surface, and finally their desorption. Solvent release during the measurement can be therefore described as a diffusion problem, where its concentration $c(x, t)$ changes in time and along the thickness of the material according to [15, 16]

$$\begin{aligned}\frac{\partial c(x, t)}{\partial t} &= D(T) \frac{\partial^2 c(x, t)}{\partial x^2} + N_0 p(T) \theta(x, t) \\ \frac{\partial \theta(x, t)}{\partial t} &= -p \theta^n(x, t)\end{aligned}\tag{5.2}$$

Where N_0 is the density of solvent sites in the polymer, $x \in [0, h]$ is the direction of solvent diffusion, with $x = 0$ and $x = h$ the two opposite surfaces of the film and $\theta(x, t) \in [0, 1]$ is the fractional occupancy, so that $\theta(x, t) = 0$ means that all the sites are empty while $\theta(x, t) = 1$ means that all the sites are full. $D(T)$ is the diffusion coefficient for cyclohexanone in PVC and $p(T)$ is the probability for a solvent molecule to be released from its site and n is the desorption order. Temperature dependence of D and p follows an Arrhenius type behaviour so that it can be written as $D(T) = D_0 \exp\left(\frac{E_d}{k_B T}\right)$ and $p(T) = \nu_0 \exp\left(\frac{E_k}{k_B T}\right)$. A solvent molecule must overcome an energy barrier E_k in order to leave its site in the molecule, this energy comes from thermal fluctuations so that the pre-exponential term ν_0 can be seen as the frequency at which this energy barrier is confronted by the molecule and can be written as $\nu_0 = k_B T / h \sim 10^{12} - 10^{13} \text{ s}^{-1}$, where h is the Plank constant. The diffusion problem can therefore be solved and the solvent desorption flux measured by the spectrometer can be eventually computed as

$$j(t) = -D \left(\frac{\partial c(x, t)}{\partial x} \right)_{x=0} - D \left(\frac{\partial c(x, t)}{\partial x} \right)_{x=h}\tag{5.3}$$

By following this approach, starting from literature parameters [17] it is possible to reproduce the temperature corresponding to the maximum of solvent

desorption, however computed peaks are much larger than measured one. This suggests that solvent diffusion is a rate limiting process, so that solvent desorption was assumed to be controlled only by the release of solvent molecules from their sites and the desorption flux is therefore proportional to

$$j(t) \propto -\frac{\partial\theta(x,t)}{\partial t} = p\theta^n(x,t) \quad (5.4)$$

In this way solvent desorption curves fitting the measured peaks are obtained, as shown in Figure(5.6). This is a further confirmation that cyclohexanone release from PVC is a thermally activated process, so that it is not possible to eliminate it by drying the sample for longer times at lower temperature, as also observed experimentally.

5.2.4 UV-visible spectroscopy

To characterize the investigated materials from the optical point of view films with thickness of about 10 μm are used, deposited on a quartz substrate as a single layer of the spin coating procedure previously described. Quartz was used as substrate instead of glass because of its low absorption in the UV part of the spectrum, where samples need to be characterized because laser used for impulse generation emits at 248 nm wavelength.

The aim of optical characterization in this case is to quantify how much of laser radiation is absorbed by the sample, and therefore can contribute to ablation. This is done by measuring optical absorbance, defined as

$$A(\lambda) = -\log_{10} \left(\frac{I_T}{I_0} \right) = \epsilon(\lambda)ch \quad (5.5)$$

where I_T and I_0 are respectively the transmitted and incoming intensities. From this measurement is then useful to compute the penetration depth of laser radiation in the sample, which is in principle related to the Lambert-Beer law

$$I_T = I_0 \exp -\alpha(\lambda)d \quad (5.6)$$

In order to use equation(5.6), however, a fundamental requirement is that absorbance must grow linearly with concentration, as expressed in equation(5.5) with $\epsilon(\lambda)$ called the molar extinction coefficient, c the concentration of the absorber and h the path of the radiation in the sample, that in case of a film is its thickness.

Even if the same spin coating procedure and the same concentration of PVC in cyclohexanone are used to prepare films for this measurement, slightly different thicknesses can be obtained for different samples, due to the high viscosity of the solutions and to the presence of CNPs or PSS. Film thickness is therefore measured for each material by using a mechanical stylus profilometer (Dectak IIA), by simply cutting half of the film and measuring the height of the step when stylus moves from the substrate up to the film. Film thickness typically show 10% variations for the different samples, so the linearity of absorbance with concentration of absorber is verified by dividing it for film thickness, as presented in Figure(5.7) where linearity with concentration is clearly confirmed.

It is now possible to define an absorption coefficient $\alpha(\lambda)$ according to

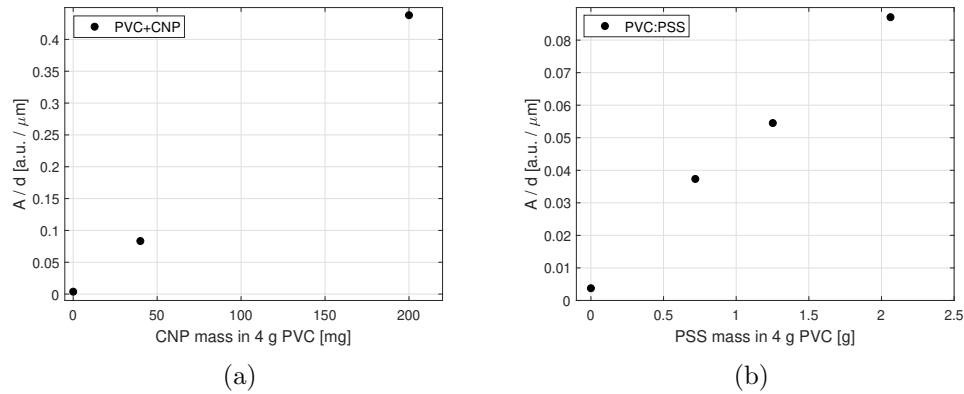


Figure 5.7: Measured absorbance normalized for film thickness as a function of absorber concentration. Note the much fast increase in absorbance given by the addition of CNPs with respect to PSS. Typical uncertainty in this measurement is 1%, mainly coming from uncertainty in thickness measurement.

equation(5.6). Figure(5.8) shows α as a function of wavelength in the range between 200 nm and 300 nm, and a line corresponding to laser wavelength, 248 nm. Neat PVC shows very low optical absorption at laser wavelength, while the introduction of absorbers clearly increases it. In particular it is possible to note that the addition of CNPs leads to a much faster increase in absorption compared to PSS as clear from Figure(5.7). Moreover optical absorption at 248 nm for PVC+1 wt% CNPs is almost equal to that obtained in

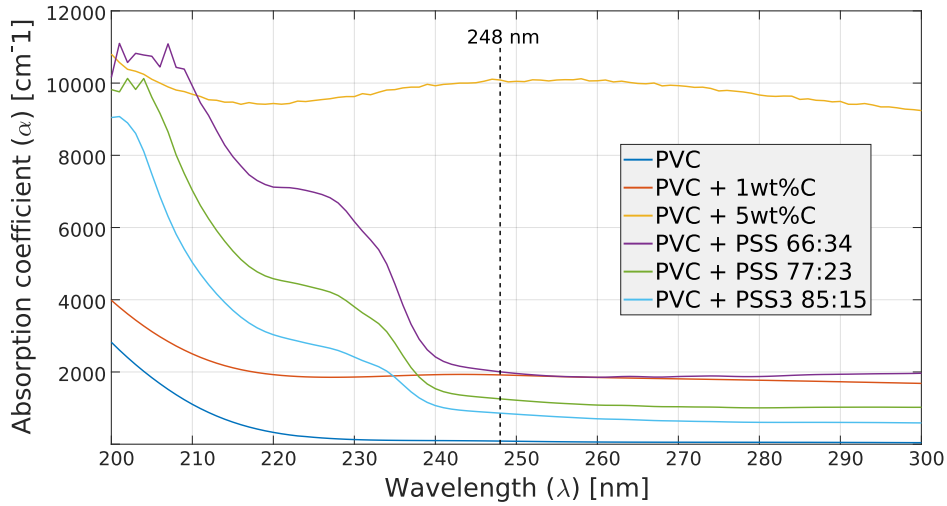


Figure 5.8: Absorption coefficient in the UV spectrum for all the considered samples. Dotted vertical line indicates laser wavelength.

the case of PVC:PSS(66:34), allowing to compare the ablation properties of two materials that have very similar interaction volumes with laser radiation.

It must be considered eventually that absorbance is in principle due to both absorption and scattering. This clearly requires particular attention in the case of samples containing CNPs, since they have ~ 500 nm size, which is comparable to laser wavelength. Scattering and absorption for this kind of nanoparticles is well described by Mie theory[18] even if their shape is not spherical. Nevertheless, the validity of Mie theory for this kind of CNPs is confirmed in literature[19, 20]. Computing scattering and absorption cross sections[21] comparable values are obtained, meaning that both the phenomena occur.

It is also possible to observe the angular distribution of the scattered radiation, as presented by Figure(5.9), where it can be noted that it is strongly peaked in the forward direction. Since absorbance measurements are performed by measuring the transmitted intensity in the same direction of incoming light, it is then reasonable to assume that also the scattered radiation is collected by the detector as transmitted. Multiple scattering events, moreover, are not present due to the linearity of absorbance with concentration, and in any case would result in even more forward peaked distributions[22].

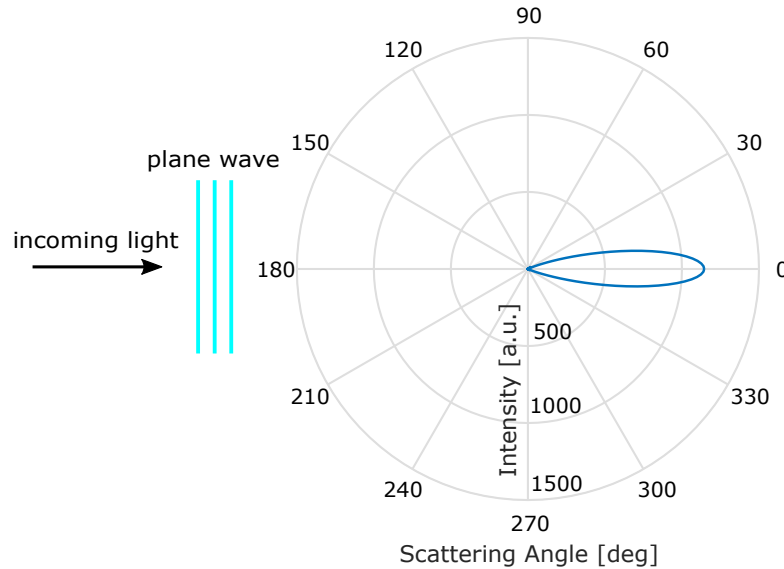


Figure 5.9: Angular distribution of the radiation scattered by a CNP with 300 nm size as computed using Mie theory. Strong peaking of scattered light in the forward direction is visible.

Measured absorbance can be considered therefore as mainly due to absorption. This assumption will be confirmed experimentally in the next chapter, where effects of scattering and absorption are measured separately.

5.2.5 Impulse measurements

Mechanical impulse generated by laser ablation of the investigated materials is measured using the experimental apparatus presented in Chapter 3 and using the uniform beam intensity distribution presented in Chapter 4.

Figure(5.10,a,b) show results obtained on PVC, PVC+CNP and PVC:PSS for fluences up to 3 J/cm^2 . First of all an experimental observation is possible: to complete a curve for a given material several different samples are needed, and reproducible results falling on the same curve are obtained. To have a sufficient number of targets the preparation procedure was repeated a few times; moreover each different target fixed on the pendulum changes its center of mass and moment of inertia. The fact that a single curve for

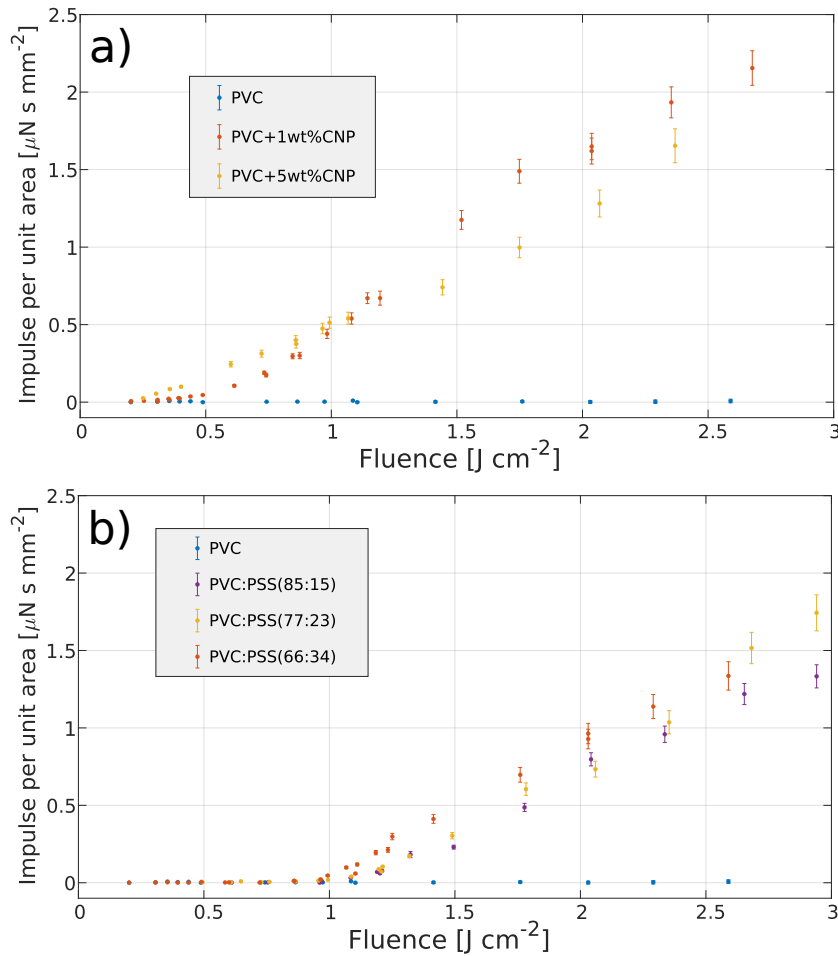


Figure 5.10: Impulse measured on the prepared polymer samples.

each material is obtained confirms both the reproducibility of the preparation procedure and the coherence of the measurement of geometric and mass properties of the pendulum presented in Chapter 3, as well as the validity of all impulse measurement procedure.

From Figure(5.10,a) it clearly appears that no impulse is observed in the case of neat PVC, while the introduction of absorbers enables impulse generation, as observed for all the other samples. In all cases impulse grows linearly with laser fluence, above a threshold value. The curves obtained for the different materials under investigation can therefore be compared by

looking at the impulse generation threshold (F_{th}) and the rate of impulse increase with fluence.

Starting from this second parameter, obtained results show that impulse grows at the same rate with fluence for all the considered samples, except for the PVC+5wt%CNPs case that show a slight difference. As visible from

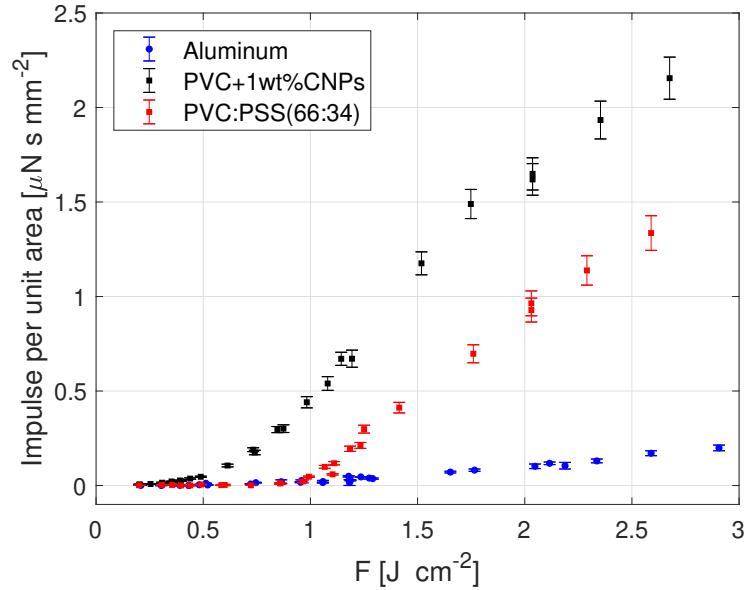


Figure 5.11: Comparison between impulse generated by PVC samples and aluminum. Different rate of impulse increasing with fluence is visible for the different materials

Figure(5.11), if impulse curves obtained for these samples are compared with impulse generated by a different material, like aluminum, different slopes are clearly visible, suggesting that this feature is material-dependent. This means that, in the case of polymer samples here considered, impulse generation is due to ablation of the same material, that is, PVC. In other words, this observation suggests that PSS or CNPs ejection during ablation plays a minor role in impulse generation. Differences observed in the case of PVC+5wt%CNPs can be explained instead by the fact that the higher CNPs concentration leads to fractures in the material during ablation, resulting probably in the ejection of slow, heavy solid fragments.

Moving to impulse generation threshold, this parameter can be estimated

smaple	F_{th}
PVC+1wt%CNP	0.5
PVC+5wt%CNP	0.2
PVC:PSS(85:15)	1.0
PVC:PSS(77:23)	1.1
PVC:PSS(66:34)	1.0

Table 5.2: Impulse generation threshold F_{th} . Error on the estimated F_{th} value is 0.1 J/cm^2

by fitting the linear part of impulse curve and computing fluence corresponding to $J = 0$. In this case differences exist between PVC+CNP and PVC:PSS, as better visible in Figure(5.11). In the case of PVC+CNP a value $F_{th,5wt\%} = 0.2 \text{ J/cm}^2$ is observed for the sample containing 5 wt% CNPs while $F_{th,1wt\%} = 0.5 \text{ J/cm}^2$ is obtained in the case of 1 wt% CNPs. In the case of 1 wt% CNPs concentration a quite long tail is present, so that non zero impulses are detectable also at fluences lower than $F_{th,1wt\%}$ and close to $F_{th,5wt\%}$. However, by looking at optical microscope images of abla-

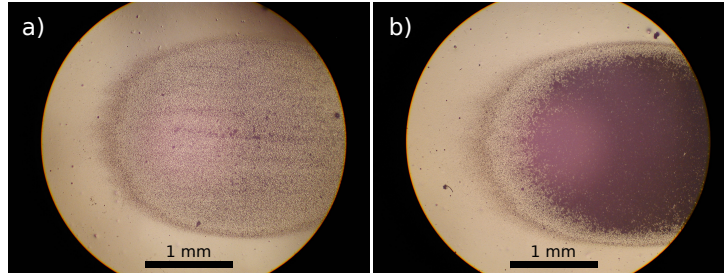


Figure 5.12: Optical images of ablation craters on PVC+1wt%CNP obtained at 0.49 J/cm^2 (a) and 0.62 J/cm^2 (b)

tion craters on the PVC+1wt%CNP sample it is possible to observe a clear variation in surface morphology when fluence overcomes $F_{th,1wt\%}$, so that this threshold definition sound reasonable. Such change in surface morphology is visible also by stylus profilometry and SEM, and will be discussed in detail in the Chapter 6, along with its relation to the mass ejection mechanism. Considerably higher F_{th} values are observed for PVC:PSS samples, as visible in Figure(5.10,b). In this case the same threshold is observed for all the samples, even if they have different optical absorption. On the other hand,

comparing PVC+1wt%CNP and PVC:PSS(66:34) samples, much different values of F_{th} are obtained, even if they have very similar optical absorption. This leads to interesting considerations when discussing optical coupling of these materials with laser radiation from the energetic point of view, as presented in the next section.

In order to discuss energetic efficiency in the impulse generation process

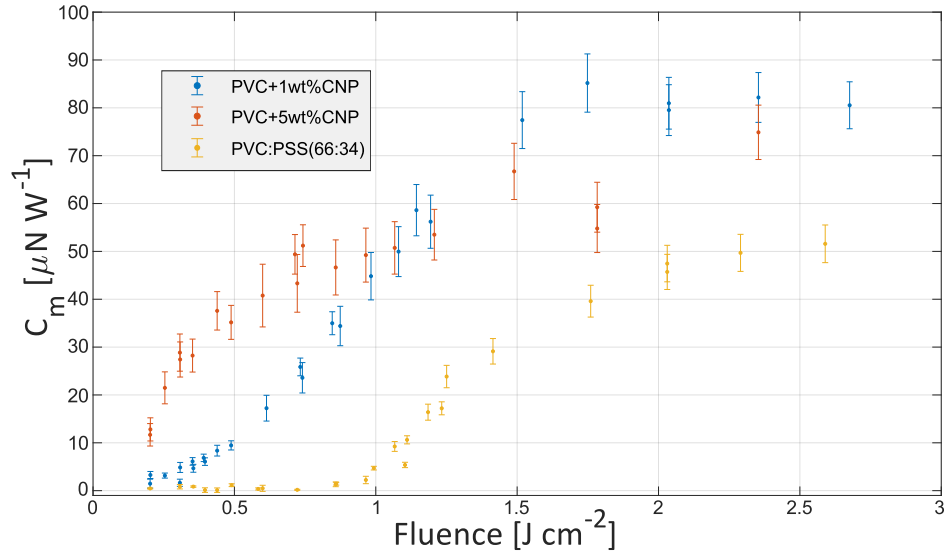


Figure 5.13: Obtained C_m curves for PVC+CNP samples and PVC:PSS(66:34). Other PVC:PSS curves are not shown because are equal to the showed one.

and to compare obtained results with literature coupling coefficient C_m is computed, as presented in Figure(5.13). Only one curve is presented for the PVC:PSS samples since they show very similar behaviour. Consequences of lowering F_{th} are clearly visible by comparing curves corresponding to PVC+1wt%CNP and PVC:PSS(66:34). Being C_m inversely proportional to the laser pulse energy, clearly a lower F_{th} brings to an increase in the energetic efficiency of the process, moreover the maximum of C_m curve seems to occur at lower fluences in the case of PVC+1wt%CNP. A similar effect is visible for PVC+5wt%CNP: here the fact that impulse increasing rate is lower than the other samples results in a maximum C_m lower than that observed for PVC+1wt%CNP.

Results obtained on PVC+CNP are also surprisingly similar to other mea-

measurements on the same material under very different experimental conditions, using IR wavelength and much longer pulse duration ranging from 100 μs [2] to hundreds of ms[1].

Some final considerations on impulse measurements concern the role of solvent traces in the sample. As previously observed, solvent traces can be removed by increasing the drying temperature as clear from DSC curves in Figure(5.5). Impulse measurements are therefore made on PVC+1wt%CNP samples dried at 40 °C, 80 °C, 120 °C, 160 °C, as presented in Figure(5.14).

No differences are visible in the obtained impulse curves, confirming that

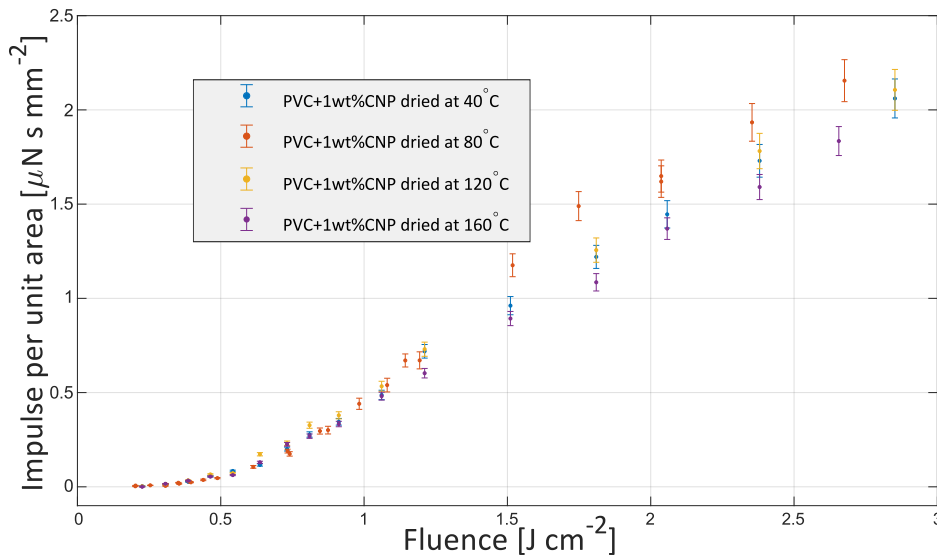


Figure 5.14: Impulse measured on PVC+1wt%CNP samples dried at different temperatures. All the curves agree with each other, confirming that solvent does not affect impulse generation.

solvent traces do not affect impulse generation. Moreover, the presence of different amounts of solvent in these samples also change their mechanical properties, since it act as plasticizer. The fact that no differences are observed in impulse generation suggests also that mechanical properties play a minor role in this process.

5.3 Discussion

Thermal decomposition of the investigated materials observed by TDS shows that the addition of PSS leads to a consistent reduction of decomposition temperature T_{dec} with respect to neat PVC or PVC+CNPs. These measurements also confirmed that thermal decomposition of all the samples proceed in the same way, with the ejection of HCl. Moreover DSC measurements gave other important thermodynamic information about the specific heat $C_p(T)$ of the samples, showing that it is not affected by CNPs, but it increases with the addition of PSS.

It is possible then to compare PVC+CNPs and PVC:PSS by estimating the energy needed to achieve thermal decomposition of the materials, given by

$$E_{dec} = \int_{T_0}^{T_{dec}} \rho C_p(T) dT \quad (5.7)$$

where T_0 is room temperature and $\rho = 1.4 \text{ g/cm}^3$ is PVC mass density assumed to the same for all samples. From equation(5.7) it results that $E_{dec,PVC:PSS} < E_{dec,PVC}$, because, even if PVC:PSS has a higher C_p , thermal decomposition occurs at much lower temperature. As an example it is possible to compare $E_{dec,PVC:PSS(66:34)}$ (the sample with higher C_p) with neat $E_{dec,PVC}$, which is identical to PVC+CNPs samples. By using in equation(5.7) $T_0 = 298 \text{ K}$, $T_{dec,PVC} = 500 \text{ K}$ and $T_{dec,PVC:PSS} = 350 \text{ K}$ it is obtained $E_{dec,PVC} = 587 \text{ J/cm}^3$ and $E_{dec,PVC:PSS} = 125 \text{ J/cm}^3$.

Moving to laser ablation, this also proceeds by thermal decomposition of the samples with HCl ejection, as commonly accepted in literature[1] and proved experimentally in the next Chapter. In this case an opposite behaviour is observed with respect to TDS measurements: a lower value of F_{th} is observed for PVC+CNPs. This means that, when thermal decomposition is reached by means of laser irradiation, a lower amount of energy is required when using CNPs as absorbers with respect to PSS.

When thermal decomposition is reached by simply heating the material, like in TDS or DSC, the same temperature is present at any point of the sample at any time. On the other hand during laser irradiation temperature increase of the samples occurs differently in PVC+CNPs than PVC:PSS, because of the different distribution of optical absorption sites in the material as presented in Figure(5.15). As clear from SEM images, CNPs act as iso-

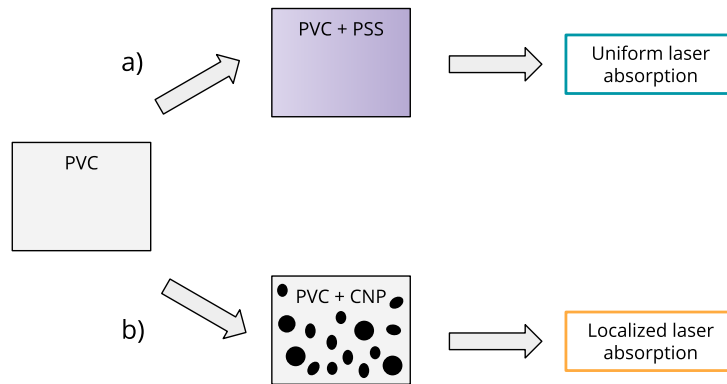


Figure 5.15: Scheme of the different distribution of absorbers in the synthesized materials.

lated localized absorbers for laser radiation, while PSS is homogeneously distributed throughout all the sample. The fact that a lower F_{th} is observed for PVC+CNPs, even if less energy is needed to bring PVC:PSS to thermal decomposition, shows that localized absorption obtained with nanoparticles is a more energetically efficient way to absorb and exploit laser radiation. Considering the case in which laser-material interaction volume is similar, as happens for example comparing PVC+1wt%CNPs and PVC:PSS(66:34), the observed difference in F_{th} shows that laser radiation is exploited differently. As discussed more in detail in the following chapter, in PVC+CNPs laser radiation is absorbed by CNPs so that their temperature increases. Successively heat diffuses towards PVC matrix causing the thermal decomposition of a shell surrounding the CNP. In other words hot-spots at high temperature are generated in the material during laser irradiation, while interstitial regions remain cold and are heated on longer times because of heat diffusion. A very different situation is present in the case of PVC:PSS, where a uniform temperature increase occurs. If the same energy is absorbed in the same volume of these two materials, of course temperatures sufficiently high for PVC decomposition will be reached at lower laser energies when absorption is localized in hot-spots.

These results investigations allow then to point at localized optical absorption of laser radiation as a more efficient coupling strategy to enable laser ablation an impulse generation of PVC. This in turn represents an indication for the development of specifically designed materials to be used for LAP applications.

Bibliography

- [1] Hiroyuki KOIZUMI, Takayoshi INOUE, Kimiya KOMURASAKI, and Yoshihiro ARAKAWA. Fundamental characteristics of a laser ablation microthruster. *TRANSACTIONS OF THE JAPAN SOCIETY FOR AERONAUTICAL AND SPACE SCIENCES*, 50(167):70–76, 2007. doi: 10.2322/tjsass.50.70.
- [2] Claude Phipps and James Luke. Diode laser-driven microthrusters: A new departure for micropropulsion. *AIAA Journal*, 40(2):310–318, 2002. doi: 10.2514/2.1647.
- [3] C. Phipps, J. Luke, T. Lippert, M. Hauer, and A. Wokaun. Micropropulsion using a laser ablation jet. *Journal of Propulsion and Power*, 20(6):1000–1011, 2004. doi: 10.2514/1.2710.
- [4] Lukas Urech, Marc Hauer, Thomas Lippert, Claude R. Phipps, Esther Schmid, Alexander Wokaun, and Ingrid Wysong. Designed polymers for laser-based microthrusters: correlation of thrust with material, plasma, and shockwave properties (Plenary Paper). In Claude R. Phipps, editor, *High-Power Laser Ablation V*, volume 5448, pages 52 – 64. International Society for Optics and Photonics, SPIE, 2004. doi: 10.1117/12.544771.
- [5] L. Urech, T. Lippert, C.R. Phipps, and A. Wokaun. Polymer ablation: From fundamentals of polymer design to laser plasma thruster. *Applied Surface Science*, 253(15):6409–6415, 2007. ISSN 0169-4332. doi: <https://doi.org/10.1016/j.apsusc.2007.01.026>. Proceedings of the Fifth International Conference on Photo-Excited Processes and Applications.
- [6] Pietro Battocchio, Jacopo Terragni, Vito Cristino, Nicola Bazzanella, Riccardo Checchetto, Michele Orlandi, Stefano Caramori, and Antonio Miotello. Poly(vinyl chloride) coupling with uv laser radiation: Comparison between polymer absorbers and nanoparticles to increase efficiency for laser ablation propulsion. *The Journal of Physical Chemistry C*, 125(51):28088–28099, 2021. doi: 10.1021/acs.jpcc.1c08175.
- [7] Thomas Lippert, Akira Yabe, and Alexander Wokaun. Laser ablation of doped polymer systems. *Advanced Materials*, 9(2):105–119, 1997. doi: <https://doi.org/10.1002/adma.19970090203>.

- [8] Hiroshi Fukumura and Hiroshi Masuhara. The mechanism of dopant-induced laser ablation. possibility of cyclic multiphotonic absorption in excited states. *Chemical Physics Letters*, 221(5):373–378, 1994. ISSN 0009-2614. doi: [https://doi.org/10.1016/0009-2614\(94\)00277-0](https://doi.org/10.1016/0009-2614(94)00277-0).
- [9] Juergen Ihlemann, Matthias Bolle, Klaus Luther, and Juergen Troe. Near-UV laser ablation of doped polymers. In Manijeh Razeghi, editor, *Physical Concepts of Materials for Novel Optoelectronic Device Applications I: Materials Growth and Characterization*, volume 1361, pages 1011 – 1019. International Society for Optics and Photonics, SPIE, 1991. doi: 10.1117/12.24328.
- [10] R. Srinivasan, B. Braren, R. W. Dreyfus, L. Hadel, and D. E. Seeger. Mechanism of the ultraviolet laser ablation of polymethyl methacrylate at 193 and 248 nm: laser-induced fluorescence analysis, chemical analysis, and doping studies. *J. Opt. Soc. Am. B*, 3(5):785–791, May 1986. doi: 10.1364/JOSAB.3.000785.
- [11] M. J. O’Neill. Measurement of specific heat functions by differential scanning calorimetry. *Analytical Chemistry*, 38(10):1331–1336, 1966. doi: 10.1021/ac60242a011.
- [12] Shu-Sing Chang. Heat capacity and thermodynamic properties of poly(vinyl chloride). *Journal of Research of the National Bureau of Standards*, 82(1):9, 1977.
- [13] A. Jiménez, V. Berenguer, J. López, and A. Sánchez. Thermal degradation study of poly(vinyl chloride): Kinetic analysis of thermogravimetric data. *Journal of Applied Polymer Science*, 50(9):1565–1573, 1993. doi: <https://doi.org/10.1002/app.1993.070500910>.
- [14] Hideo Kise. Dehydrochlorination of poly(vinyl chloride) by aqueous sodium hydroxide solution under two-phase conditions. *Journal of Polymer Science: Polymer Chemistry Edition*, 20(11):3189–3197, 1982. doi: <https://doi.org/10.1002/pol.1982.170201114>.
- [15] Riccardo Checchetto, Daniele Rigotti, Alessandro Pegoretti, and Antonio Miotello. Chloroform desorption from poly(lactic acid) nanocomposites: a thermal desorption spectroscopy study. *Pure and Applied Chemistry*, 92(3):391–398, 2020. doi: doi:10.1515/pac-2018-1216.

- [16] D. Rigotti, A. Pegoretti, A. Miotello, and R. Checchetto. Interfaces in biopolymer nanocomposites: Their role in the gas barrier properties and kinetics of residual solvent desorption. *Applied Surface Science*, 507: 145066, 2020. ISSN 0169-4332. doi: <https://doi.org/10.1016/j.apsusc.2019.145066>.
- [17] A.R. Berens and H.B. Hopfenberg. Diffusion of organic vapors at low concentrations in glassy pvc, polystyrene, and pmma. *Journal of Membrane Science*, 10(2):283–303, 1982. ISSN 0376-7388. doi: [https://doi.org/10.1016/S0376-7388\(00\)81415-5](https://doi.org/10.1016/S0376-7388(00)81415-5).
- [18] *Absorption and Scattering by a Sphere*, chapter 4, pages 82–129. John Wiley & Sons, Ltd, 1998. ISBN 9783527618156. doi: <https://doi.org/10.1002/9783527618156.ch4>.
- [19] Kamjou Mansour, M. J. Soileau, and E. W. Van Stryland. Nonlinear optical properties of carbon-black suspensions (ink). *J. Opt. Soc. Am. B*, 9(7):1100–1109, Jul 1992. doi: 10.1364/JOSAB.9.001100.
- [20] Ghassan Taha, Gail P. Box, David D. Cohen, and Ed Stelcer. Black carbon measurement using laser integrating plate method. *Aerosol Science and Technology*, 41(3):266–276, 2007. doi: 10.1080/02786820601156224.
- [21] Christian Matzler. Matlab functions for mie scattering and absorption. *IAP Res Rep*, 8, 07 2002.
- [22] Yu Guo, Adrian Jarabo, and Shuang Zhao. Beyond mie theory: Systematic computation of bulk scattering parameters based on microphysical wave optics. *ACM Trans. Graph.*, 40(6), dec 2021. ISSN 0730-0301. doi: 10.1145/3478513.3480543.

Chapter 6

Role of carbon nanoparticles size and number concentration as absorbers in PVC for impulse generation

In Chapter 5 localized laser absorption obtained by embedding CNPs in PVC proved to be more energetically efficient in impulse generation, compared to uniform absorption. To move further in this direction, in order establish relevant material properties for LAP, an interesting possibility is now to investigate the role of CNPs size, morphology and concentration in this process. As previously discussed, PVC+CNPs is considered a sort of benchmark material for LAP experiments, and impulse measurements can be found in different works[1, 2, 3, 4]. Particular features of employed CNPs however are not clarified, as well as their connection with ablation of PVC and impulse generation. Ablation of PVC+CNPs is expected to proceed with laser absorption by CNPs, followed by their temperature increase and heat diffusion towards PVC matrix, that eventually decompose causing mass ejection. It is then reasonable to expect that differences in CNPs size, morphology and concentration may in some way affect propulsion performances, since they play a role in optical absorption of laser radiation and in heat distribution in the PVC matrix.

An experimental investigation on the role of CNPs in laser ablation of PVC is presented in this Chapter. Both commercial and synthesised carbon

nanoparticles with different sizes and morphology are embedded in PVC, samples are then characterized in order to understand the role of differences in structure, in optical interaction with laser and impulse generation. An additional structural and compositional analysis is then conducted on ablation craters, confirming experimentally the mechanism of ablation. Moreover, impulse measurements on graphite are also performed in order to check the possibility to have ablation of embedded CNPs.

Differences in CNPs are observed to affect mainly optical absorption of the sample, which in turn affects the fluence threshold for impulse generation F_{th} . The most important parameter related to CNPs size and concentration is their number density, that when increased results in a reduction of F_{th} . A lower limit for F_{th} is found, that can be explained by considering again CNPs as isolated absorbers.

6.1 Sample preparation

6.1.1 Materials

As made in Chapter 5, PVC (Sigma-Aldrich, powder, average $M_w \sim 43000$ g mol⁻¹, average $M_n \sim 22000$ g mol⁻¹) is used by dissolving it in cyclohexanone (Sigma-Aldrich).

Two different commercial (Sigma-Aldrich) carbon nanoparticles with nominal size < 100 nm and < 500 nm are used. Additionally other carbon nanoparticles with size $\sim 1\mu\text{m}$ and $\sim 250\text{nm}$ are synthesised by hydrothermal carbonization (HTC)[5].

6.1.2 Preparation procedure

The same procedure for polymer dissolution and spin coating described in Chapter 5 is used here to prepare polymer films. However following this procedure the presence of large clusters ($\sim 10 \mu\text{m}$) is observed when using commercial CNPs with nominal size < 100 nm and HTC particles with size ~ 250 nm, so a slightly different procedure is used to remove them. Instead of adding CNPs after the complete dissolution of PVC, they are first put in cyclohexanone and left in ultrasonic bath for ~ 3 h. As confirmed by SEM analysis, this allows to remove clusters in the case of < 100 nm CNPs but not in the case of ~ 250 nm ones: in this second case it was not possible to remove

clusters. Successively PVC is added to cyclohexanone containing CNPs, by adding 25% of the final PVC mass every 24h: this allows to dissolve the polymer in a less viscous solution, so that CNPs are more easily dispersed. For the purpose of this investigation on the role of CNPs size in impulse generation, clusters can also be considered as very large particles, so samples containing them can also be included in the experiment. All the considered samples are listed in table(6.1).

Sample name	CNPs size	CNPs [wt%]	Clusters
PVC+1wt%CNPs(1 μ m)	1 μ m	1	no
PVC+0.5wt%CNPs(500 nm)	500 nm	0.5	no
PVC+1wt%CNPs(500 nm)	500 nm	1	no
PVC+2wt%CNPs(500 nm)	500 nm	2	no
PVC+1wt%CNPs(100 nm)	100 nm	1	no
PVC+1wt%CNPs*(100 nm)	100 nm	1	yes
PVC+1wt%CNPs*(250 nm)	250 nm	1	yes

Table 6.1: Fabricated samples. The symbol * indicates samples containing clusters.

6.2 SEM analysis of samples

SEM gives useful information both on the structure and actual size of CNPs and on the structure of the prepared polymer films.

Information on CNPs is obtained by scanning transmission electron microscopy (STEM). For this kind of analysis a very diluted colloidal suspension of CNPs in cyclohexanone is prepared and left in ultrasonic bath. Then a single droplet is deposited on a TEM grid and let evaporate leaving CNPs on it. Figure(6.1) presents CNPs and clusters considered for sample preparation. HTC particles with typical size $\sim 1\mu$ m in Figure(6.1,a) show a well defined spherical shape and also similar sizes. On the other hand commercial CNPs(500 nm) are composed by grains with size of some tens of nm that are fused together so that very different shapes are observed. In any case typical sizes are ~ 500 nm and no clusters are observed.

A different situation is instead observed when CNPs(100 nm) are considered. If only a few minutes in ultrasonic bath are used to prepare the colloidal

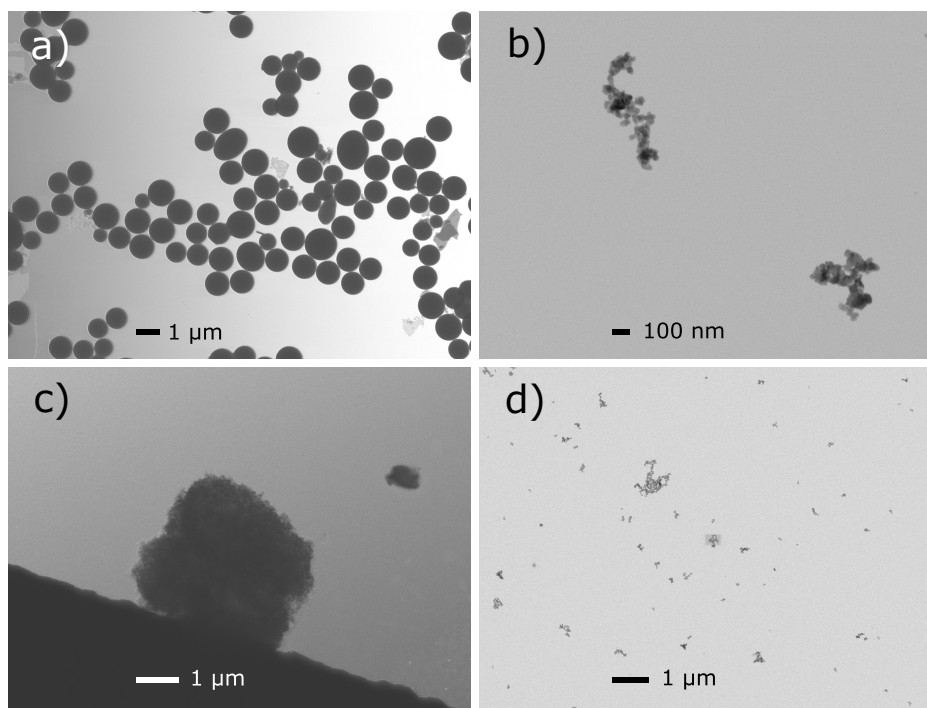


Figure 6.1: STEM images of used CNPs. **a)** CNPs synthesised by HTC; **b)** commercial CNPs with nominal size < 500 nm; **c)** cluster formed by commercial CNPs with nominal size < 100 nm after few minutes in ultrasonic bath; **d)** commercial CNPs with nominal size < 100 nm obtained after few hours ultrasonic bath.

suspension, large clusters are observed, as visible in Figure(6.1,c). If on the other hand the suspension is left in the ultrasonic bath for ~ 3 h clusters are removed, as presented in Figure(6.1,d). In this case also a few larger particles with size ~ 1 μm are visible, however to a closer inspection they appear flat and composed by many smaller particles, suggesting that some agglomeration occurs on the TEM grid while the droplet is drying, but no clusters are present in the colloidal dispersion.

Very large clusters are instead obtained in the case of HTC CNPs(~ 250 nm), as clearly visible in Figure(6.2,a). In this case SEM images are presented instead of STEM. Also in this case single CNPs are spherical, with typical size ~ 250 nm, but they look as stuck together as clear from Figure(6.2,b). Even with very long times in ultrasonic bath it was not possible to break

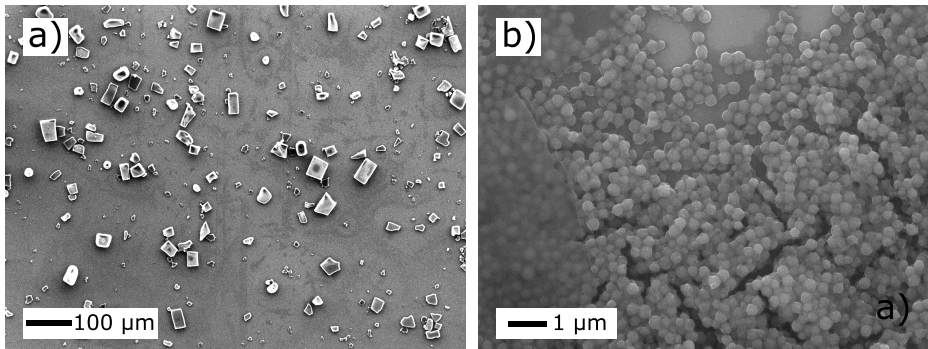


Figure 6.2: **a)** large clusters formed by HTC synthesised CNPs with typical size ~ 250 nm; **b)** higher magnification image on a cluster showing the single CNPs.

these clusters, suggesting that they arise directly from HTC preparation.

The presence of clusters is confirmed also by looking at the surfaces of polymer films. Figure(6.3) compares the surface of PVC+1wt%CNPs(500 nm) with that of PVC+1wt%CNPs*(100 nm), that contains clusters like the one shown in Figure(6.1,c). Clusters in PVC+1wt%CNPs*(100 nm) case appear as large defects on the surface, that are not visible in PVC+1wt%CNPs (500 nm).

Figure(6.4) presents two examples of cross sections of the prepared polymer films, for CNPs(1 μm) and CNPs(100 nm) samples. The presence of CNPs is clearly visible in Figure(6.4,a), thanks to their spherical shape that allows to easily find them or the holes they leave during cutting. The irregular shape of commercial CNPs makes instead their identification much more difficult, as clear from Figure(6.4,b).

Figure(6.4,a) allows to confirm the uniform dispersion of CNPs in the film, that can be assumed to hold also for all the other cases, since the same film deposition procedure is used. It is also worth noting here that the spherical shape of CNPs prepared by HTC represents an extremely useful situation for the study of these materials. In fact they are, as said, easily found in the samples and may also allow to define a size distribution, useful for possible quantitative analysis.

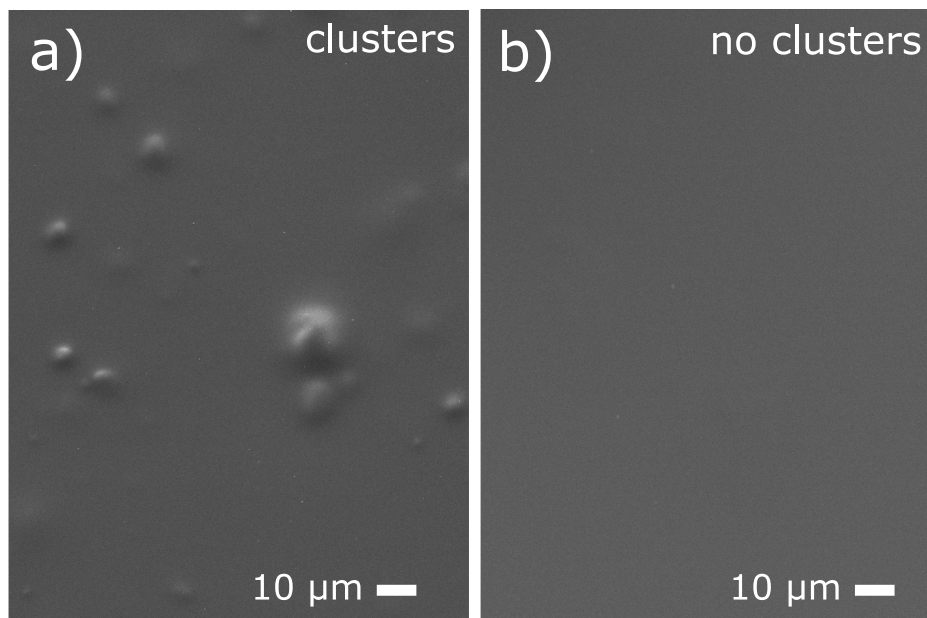


Figure 6.3: SEM images of surfaces of prepared polymer films. **a)** PVC+1wt%CNPs*(100 nm); **b)** PVC+1wt%CNPs(500 nm);

6.3 Optical characterization

Optical characterization of the prepared samples is performed in order to look at possible effects of CNPs properties in the interaction with laser radiation. The final goal, to discuss laser ablation, is to measure the quantity of incoming radiation that is absorbed by the material.

In this kind of measurement, scattering may play a significant role, since all the samples contain isolated particles that in most of the cases have size comparable with wavelengths used for optical characterization. To keep scattered radiation into account, an integrating sphere is used, allowing to measure all the radiation transmitted or reflected at all angles. The measurement then takes place by acquiring the fraction of incoming energy reflected at all angles, $\%R$, and the transmitted fraction at all angles, $\%T$, that are obtained from two independent measurements. The fraction of incoming radiation absorbed in the material is therefore given by

$$\%A = 100 - \%T - \%R \quad (6.1)$$

An example of the obtained spectra in the case of the PVC+1wt%CNPs

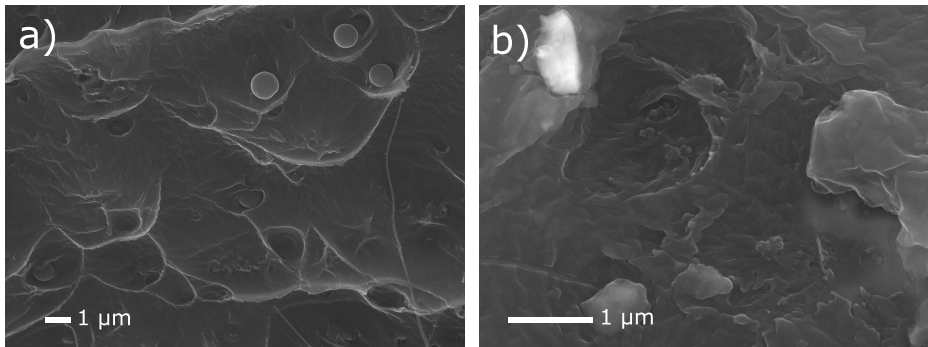


Figure 6.4: SEM images of films cross sections. **a)**PVC+1wt%CNPs(1 μm); **b)**PVC+1wt%CNPs(500 nm);

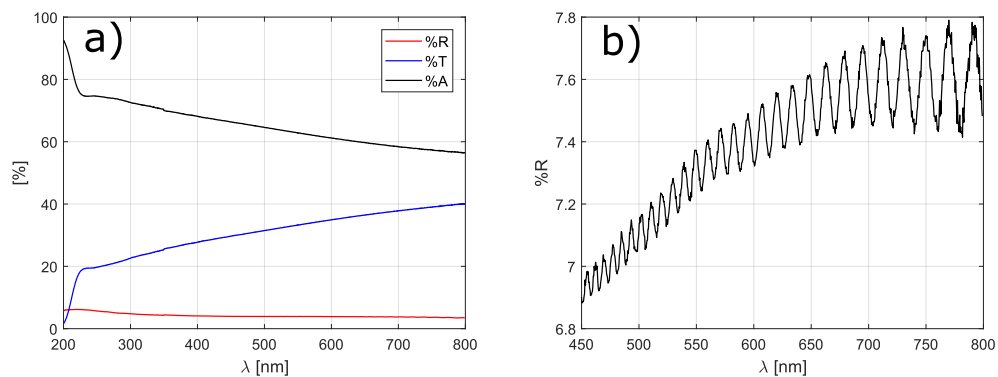


Figure 6.5: **a)**Measured curves of $\%R$ and $\%T$ and computed $\%A$ through equation 6.1; **b)**Oscillations observed in specular reflection.

(500 nm) sample is shown in Figure(6.5,a), where it can be seen that $\%R$ is very low, as observed also for all other samples, so that the main contribution to $\%A$ comes from $\%T$.

Obtained $\%A$ values can not be compared directly, since polymer films may have different thicknesses, due to slight variation in solution viscosity. Film thickness therefore must be measured in order to compare light absorption by these materials. This can be done by exploiting the fact that interference occurs due to multiple reflections between the two surfaces of the film, so that specular reflection (that accounts for almost all of the reflected light) shows an oscillating behaviour, presented in Figure(6.5,b). The wavelength

of the maxima λ_p , their separation $\Delta\lambda$ and the refraction index can be then related to the thickness of the film through the relation[6]

$$h = \lambda_p \frac{\lambda_p + \Delta\lambda}{2n\Delta\lambda} \quad (6.2)$$

The thickness of polymer films is therefore estimated through equation(6.2) by considering the maxima in the wavelength range between 500 and 800 nm, where the refractive index of PVC $n = 1.54$ can be considered constant[7]. Obtained values of h are listed in table(6.2).

Optical absorption of these films can be compared by considering the absorption coefficient α defined by Lambert-Beer law

$$\frac{I}{I_0} = \frac{100 - \%A}{100} = \exp(-\alpha h) \quad (6.3)$$

To use equation(6.3) a fundamental requirement is that α must grow linearly with concentration of absorber, meaning that no multiple scattering occurs when the number of scatterers increase[8]. Absorption coefficient α is therefore computed for samples containing CNPs(500 nm) at different concentrations, as presented in Figure(6.6,a), where its linear increase with concentration is clearly confirmed.

Equation(6.3) is then used for all the samples, obtaining α as shown in

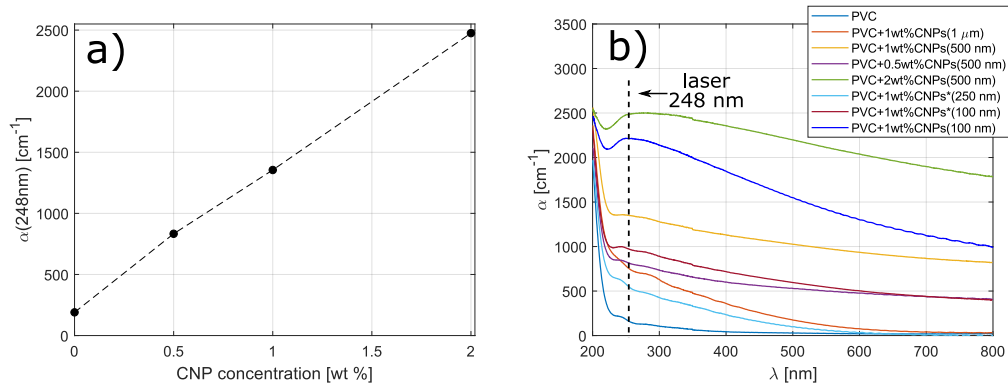


Figure 6.6: **a)** linear increase in absorption coefficient with concentration of CNPs(500 nm); **b)** absorption spectra obtained for all the samples, the curves indicated in the legend by * contain clusters.

Figure(6.6,b) for all the prepared samples, and values of $\alpha(248\text{ nm})$ are listed

in table(6.2).

From Figure(6.6,b) it is possible to see that PVC is almost transparent for

Sample name	h [μm]	α [cm^{-1}]
PVC	9.3 ± 0.4	190
PVC+1wt%CNPs(1 μm)	9.4 ± 0.7	796
PVC+0.5wt%CNPs(500 nm)	9.2 ± 0.4	833
PVC+1wt%CNPs(500 nm)	10.1 ± 0.9	1355
PVC+2wt%CNPs(500 nm)	9.4 ± 0.8	2475
PVC+1wt%CNPs(100 nm)	9.4 ± 0.5	2214
PVC+1wt%CNPs*(100 nm)	9.7 ± 0.8	992
PVC+1wt%CNPs*(250 nm)	9.7 ± 0.5	843

Table 6.2: Thickness h and absorption coefficient α obtained from optical characterization of the samples.

wavelengths longer than 200 nm, and that in all cases the addition of CNPs causes a consistent increase in optical absorption, as already observed in Chapter 5. Considerable differences in absorption among samples containing the same concentration of CNPs (1 wt%) are observed. In particular it can be noted that the presence of clusters reduces absorption, as visible comparing α obtained on samples containing CNPs(100 nm). This observation, together with the fact that α increases with concentration of CNPs, leads to the conclusion that the parameter that tunes optical absorption in the material is the number density of localized absorbers. From the point of view of size of CNPs it is possible to conclude that, for a given total mass of CNPs in the sample (fixed wt% concentration), a higher absorption coefficient will be obtained if CNPs are smaller.

6.4 Impulse measurement

Figure(6.7,a) shows two of the impulse curves obtained for the prepared samples, corresponding to samples with low and high α . The curves obtained for the other materials are not shown for clarity, being all very similar to the presented ones.

As already discussed in Chapter 5, these curves can be compared by looking at the fluence threshold for impulse generation (F_{th}) and to the rate of impulse increase with fluence. As visible, the slope of impulse curves is the

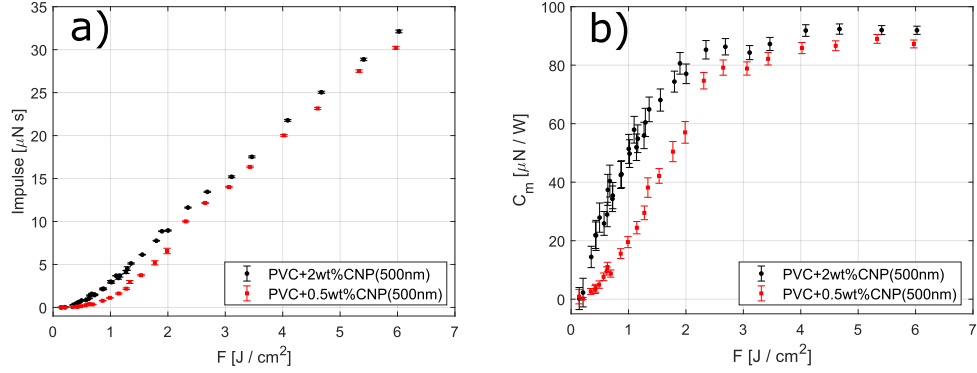


Figure 6.7: a) Impulse measured for high and low absorption samples; b) corresponding C_m curve.

same for all the considered PVC+CNPs samples, suggesting that ablation and impulse generation proceeds in the same way for all the samples, as confirmed also in the following by SEM analysis of ablation craters. The value of F_{th} on the other hand changes for the different samples, as visible in Figure(6.7,a) and listed in Table(6.3).

Figure(6.7,b) shows C_m corresponding to the curves presented in Fig-

Sample	F_{th} J/cm ²
PVC+1wt%CNPs(1 μm)	0.57 ± 0.07
PVC+0.5wt%CNPs(500 nm)	0.83 ± 0.06
PVC+1wt%CNPs(500 nm)	0.48 ± 0.07
PVC+2wt%CNPs(500 nm)	0.50 ± 0.03
PVC+1wt%CNPs(100 nm)	0.51 ± 0.03
PVC+1wt%CNPs*(100 nm)	0.87 ± 0.08
PVC+1wt%CNPs*(250 nm)	1.02 ± 0.06

Table 6.3: Measured values of F_{th} for all the samples.

ure(6.7,a). Of course a reduction in F_{th} results in an increase of C_m , expressing a higher energetic efficiency in the impulse generation process. With respect to Chapter 5, here impulse measurements are performed in a wider range of fluences, but surprisingly still no decreasing behaviour of C_m is observed. The decreasing part of C_m curve should be associated to the screening of laser pulse by the plume: this suggests that no screen by plume is present

in this case.

Some additional information can be acquired by comparing impulse gener-

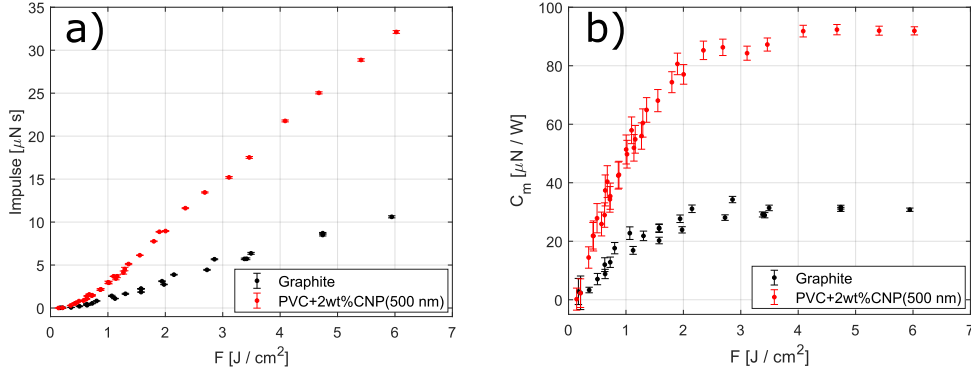


Figure 6.8: **a)** Impulse measured for graphite compared with the most absorbing PVC+CNPs sample; **b)** corresponding C_m curve.

ated by PVC+CNPs with that obtained ablating a graphite target, where only carbon is present. This is presented in Figure(6.8,a). In this case two different materials are compared, so that slope of impulse curve is different between the two materials, showing that it grows faster in the case of PVC+CNPs with respect of graphite. This fact is then reflected in C_m , as clear from Figure(6.8,b).

It is then of interest to compare F_{th} for the case of PVC+CNPs and graphite. In the case of graphite $F_{th} = 0.4 \pm 0.1$ J/cm² is obtained, a value compatible with those observed in the case of the most absorbing PVC+CNPs samples. This suggests a second possible mechanism for ablation, that may be initiated also by direct ablation of CNPs, other than PVC thermal decomposition, which is confirmed in the following.

6.5 Analysis of ablation craters

Figure(6.9) shows surface morphology of ablation craters on PVC+1wt%CNPs (500 nm) for three different fluences, crossing $F_{th} = 0.48$ J/cm². Some surface modifications are visible also at fluences lower than F_{th} , showing the appearance of bubble-like structures that become larger increasing laser fluence. Overcoming F_{th} a clear change in surface morphology appears, suggesting

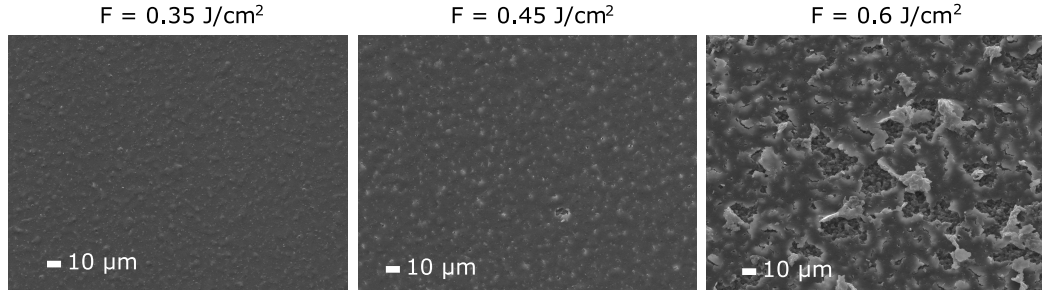


Figure 6.9: SEM images of surface morphology of ablation craters on PVC+1wt%CNPs(500 nm) for increasing fluences

that the formed bubbles break-up, ejecting decomposition products. Similar observations are made also for other samples, indicating that thermal decomposition of PVC occurs, as expected[3], in a shell surrounding each CNP sufficiently close to surface to reach polymer decomposition temperature.

Thermal decomposition of PVC is usually observed to proceed in two steps at different temperatures[9]: in the first step, at around 300 °C, HCl is released leaving carbon rich polyene chains. In the second step, occurring at around 450 °C, also these polyene chains decompose completing the total decomposition of PVC.

In order to confirm the expected ablation mechanism for PVC+CNPs, Energy Dispersion X-ray Spectroscopy (EDXS) is used to perform a compositional analysis on a representative ablation crater obtained above F_{th} for a PVC+1wt%CNPs (500 nm) sample.

Figure(6.10) shows concentration of Chlorine and Carbon inside the crater. As visible, ablation results in a reduction of Chlorine concentration, that corresponds to an increase of Carbon concentration with respect to the untreated region. Only a slight reduction in Chlorine concentration is observed; moreover, craters are not dug into the polymer but are just surface modifications. This shows that PVC thermal decomposition stops at an initial stage, so that not all Chlorine is ejected and only a carbon rich region fills the ablation crater.

A further step in the discussion can be made considering the dispersion of CNPs in the polymer matrix. From sample preparation and SEM observations on film cross sections in Figure(6.4), it is possible to assume that CNPs

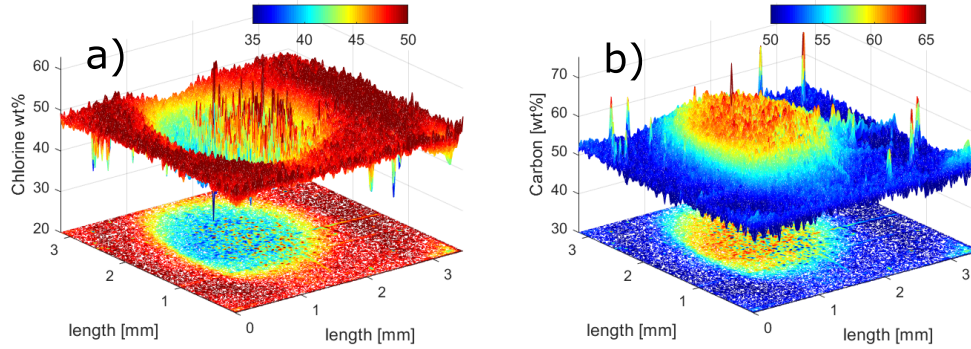


Figure 6.10: EDXS maps of an ablation crater obtained at fluence just above F_{th} on PVC+1wt%CNPs(500 nm). **a)**Chlorine concentration; **b)**Carbon concentration.

are uniformly dispersed in PVC. This allows to say that, for a fixed total mass of CNPs in the sample, if their size is reduced their number density increase, so that they become closer with each other and to the surface. Under the assumption of uniform dispersion of CNPs, it is also possible to say that, on average, the distance between two close CNPs will be equal to the distance between the surface and the first CNPs, as presented in Figure(6.11). Since from Figure(6.9) it appears that ablation proceeds by breaking bubbles containing PVC decomposition products and ejecting them, if a larger number of CNPs is closer to the surface then ablation occurs more efficiently.

6.6 Correlation between CNPs size and generated mechanical impulse

When CNPs size is reduced, an increase in absorption coefficient is observed, if the same total mass of CNPs is included in the sample. It is important to note that this results takes into account also possible scattering effects, since absorbed radiation is measured considering transmitted and reflected intensities at all angles.

Also in the case of generated impulse, differences are observed by changing CNPs size and concentration. In particular different F_{th} values are observed,

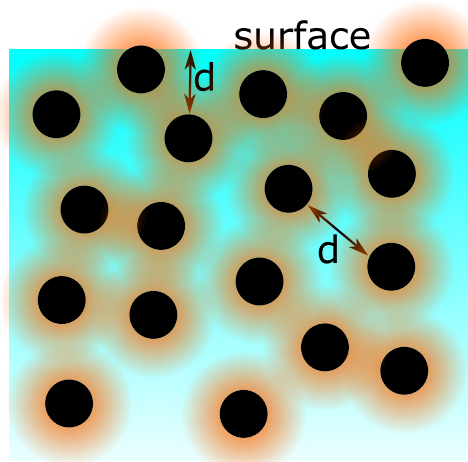


Figure 6.11: Scheme of CNPs (black dots) embedded in PVC (light blue background).

as listed in Table(6.3), while impulse grows at the same rate with fluence for all the observed samples.

SEM and EDXS analysis of ablation craters confirmed that mass ejection proceeds in all cases with thermal decomposition of PVC, suggesting that this process is not affected by the different properties of the included CNPs. This is confirmed also by looking at thermal desorption spectroscopy measurements[10] presented in Chapter 5, where thermal decomposition of PVC is compared to PVC containing 1 wt% CNPs(500 nm) and 5 wt% CNPs(500 nm), and no differences are observed.

The variations observed in impulse generation must be therefore related to the interaction of these materials with the laser and to heat diffusion in PVC, but not to differences in the thermal decomposition path.

Figure(6.12) presents measured values of F_{th} as a function of absorption coefficient α for all the considered materials. F_{th} decreases for low values of α , until it reaches a limiting value and remains constant for higher α . This effect can be expected considering that CNPs are isolated absorbers that heat up by absorbing laser radiation: there must be therefore a limiting fluence below which a sufficient temperature for PVC thermal decomposition is not reached. Impulse measurements on graphite then also show a value

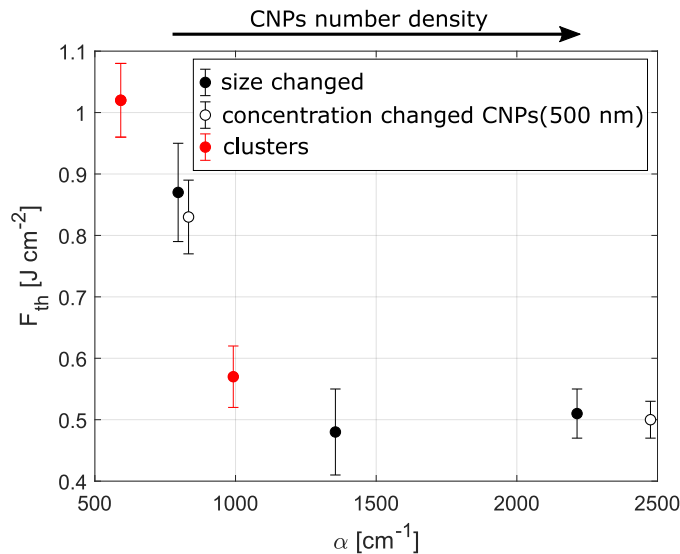


Figure 6.12: Impulse generation threshold F_{th} as a function of absorption coefficient α .

of F_{th} compatible with the values observed for the most absorbing polymer samples, suggesting that also ablation of CNPs may start, initiating mass ejection of PVC.

Bibliography

- [1] Muddassir M. S. Gualini, Shakeel A. Khan, and Salman Iqbal. Comparative study of plastics as propellants for laser ablation plasma thrusters. *Journal of Propulsion and Power*, 25(5):1138–1140, 2009. doi: 10.2514/1.40318.
- [2] Dian Kai Wang and Yan Ji Hong. Interaction of high power laser with carbon doped pvc. In *Applied Mechanics and Mechanical Engineering III*, volume 249 of *Applied Mechanics and Materials*, pages 983–986. Trans Tech Publications Ltd, 2 2013. doi: 10.4028/www.scientific.net/AMM.249-250.983.
- [3] Hiroyuki Koizumi, Takayoshi Inoue, Kohei Kojima, Koichi Mori, Kimiya Komurasaki, and Yoshihiro Arakawa. *Microthruster Experiment Using a Diode Laser*. 2003.

- [4] L. Urech, T. Lippert, C.R. Phipps, and A. Wokaun. Polymer ablation: From fundamentals of polymer design to laser plasma thruster. *Applied Surface Science*, 253(15):6409–6415, 2007. ISSN 0169-4332. doi: <https://doi.org/10.1016/j.apsusc.2007.01.026>. URL <https://www.sciencedirect.com/science/article/pii/S0169433207000761>. Proceedings of the Fifth International Conference on Photo-Excited Processes and Applications.
- [5] G. Ischia, M. Cuttillo, G. Guella, N. Bazzanella, M. Cazzanelli, M. Orlandi, A. Miotello, and L. Fiori. Hydrothermal carbonization of glucose: Secondary char properties, reaction pathways, and kinetics. *Chemical Engineering Journal*, 449:137827, 2022. ISSN 1385-8947. doi: <https://doi.org/10.1016/j.cej.2022.137827>.
- [6] *Electromagnetic Theory*, chapter 2, pages 12–56. John Wiley & Sons, Ltd, 1998. ISBN 9783527618156. doi: <https://doi.org/10.1002/9783527618156.ch2>.
- [7] Xiaoning Zhang, Jun Qiu, Xingcan Li, Junming Zhao, and Linhua Liu. Complex refractive indices measurements of polymers in visible and near-infrared bands. *Appl. Opt.*, 59(8):2337–2344, Mar 2020. doi: [10.1364/AO.383831](https://doi.org/10.1364/AO.383831).
- [8] Werner Mäntele and Erhan Deniz. Uv–vis absorption spectroscopy: Lambert-beer reloaded. *Spectrochimica Acta Part A: Molecular and Biomolecular Spectroscopy*, 173:965–968, 2017. ISSN 1386-1425. doi: <https://doi.org/10.1016/j.saa.2016.09.037>.
- [9] A. Jiménez, V. Berenguer, J. López, and A. Sánchez. Thermal degradation study of poly(vinyl chloride): Kinetic analysis of thermogravimetric data. *Journal of Applied Polymer Science*, 50(9):1565–1573, 1993. doi: <https://doi.org/10.1002/app.1993.070500910>.
- [10] Pietro Battocchio, Jacopo Terragni, Vito Cristino, Nicola Bazzanella, Riccardo Checchetto, Michele Orlandi, Stefano Caramori, and Antonio Miotello. Poly(vinyl chloride) coupling with uv laser radiation: Comparison between polymer absorbers and nanoparticles to increase efficiency for laser ablation propulsion. *The Journal of Physical Chemistry C*, 125(51):28088–28099, 2021. doi: [10.1021/acs.jpcc.1c08175](https://doi.org/10.1021/acs.jpcc.1c08175).

Chapter 7

Open problems and future works

When moving toward experimental conditions closer to those encountered in real applications of LAP, some open problems arise. Some difficulties already appear when measuring I_{sp} , a fundamental parameter to characterize a space propulsion system. In the case of LAP, problems are present in particular in metals, because of the extremely small mass ejected during ablation, so that a very high number of pulses is needed to obtain a measurable mass loss.

Furthermore, considering debris removal or nanosatellite propulsion, it is reasonable to assume that multiple pulses will irradiate the same region of the target material. This means that impulse generated by multiple irradiations must be measured, and observed variations from the first pulse discussed. This is one of the main open problems under investigation for LAP[1] and considerable differences are observed between metals and polymers, as discussed in the following.

Another interesting possibility that is recently attracting attention is confined laser ablation[2]. As briefly discussed in Chapter 2, when the expansion of ablation products is confined by a medium, a considerable increase in generated impulse is observed[3, 4, 5]. It may be of interest then to develop materials that can exploit this phenomenon to increase the efficiency of the impulse generation process.

This chapter presents some experiments related to I_{sp} measurement, to impulse generated by multiple pulses on the same region and to confined laser ablation. All these results concern topics in which further work is still

needed, but they are promising future developments for the research activity related to LAP.

7.1 Impulse generated by multiple laser pulses

Real applications of LAP will probably include multiple irradiation of the same region of the target material. It is then of interest to consider how generated impulse is related to the number of successive laser pulses, since surface modifications and changes in chemical composition may occur. This problem is in turn related to specific impulse measurements, as discussed in the following.

A reduction in generated impulse appears during the first laser pulses in

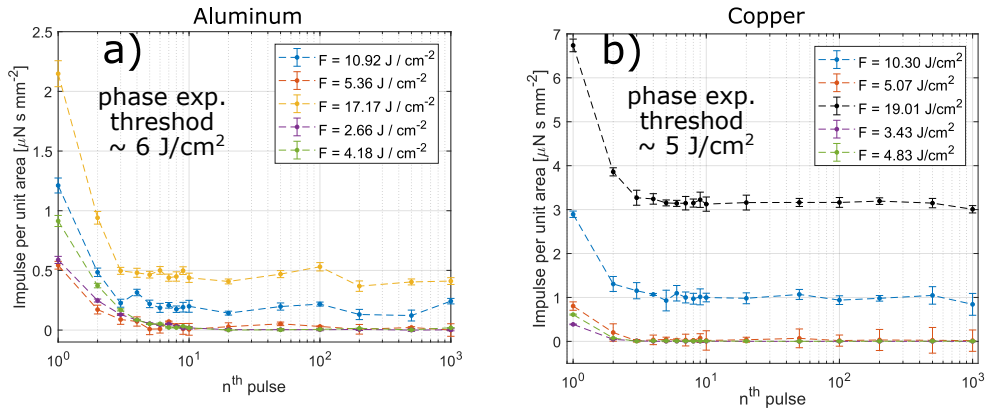


Figure 7.1: Impulse measured for increasing number of pulses in the same region. **a)**Aluminum; **b)**Copper. The indicated phase explosion thresholds are estimated from ablated mass measurements in Figure (7.4)

the case of metals, as presented in Figure(7.1). A possible explanation is related to the presence of an oxide layer at the surface of the target, that is progressively removed by the first pulses generating a higher impulse than the following ones. This layer easily forms by simply keeping the target in air, but targets are always polished before measurements and put in vacuum conditions. Additionally, once in vacuum, the target is irradiated before the measurements with pulses at low fluences, in order to further clean the surface. This hypothesis may explain impulse behaviour observed at low fluences, where oxide layer may be only partially removed by the first pulses.

However it does not explain the observations above phase explosion threshold, since the oxide layer is certainly removed after the first pulse, so that a constant impulse is expected from the second pulse on. As it appears from this discussion, further experiments and investigations are needed to clarify these observations on metals. These results, however, are important for the estimation of I_{sp} in the case of metals, where the extremely low ablated mass requires a large number of pulses that lead to the multiple irradiation of the same region.

A completely opposite situation is instead observed in the case of polymers.

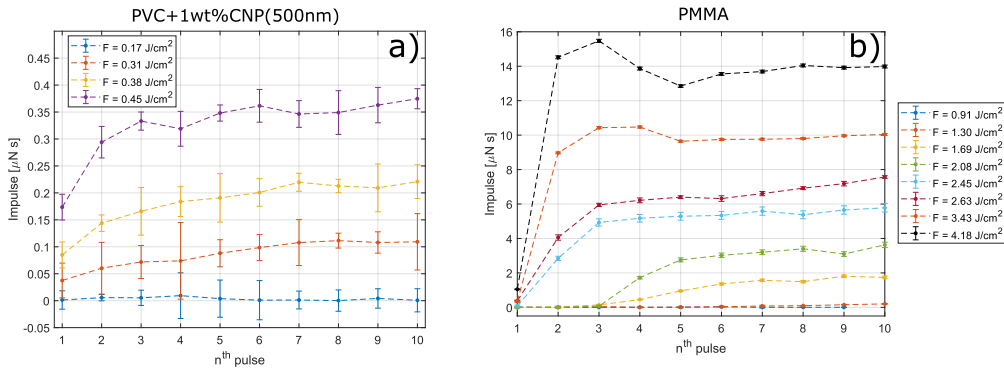


Figure 7.2: Impulse measured for increasing number of pulses in the same region. **a)**PVC+1wt%CNPs(500 nm); **b)**PMMA. Note that presented measurements are made on different fluence ranges.

Figure(7.2) presents impulse generated by successive pulses on PVC+1wt% CNP(500 nm) and on poly(methyl methacrylate) (PMMA). As visible impulse grows for increasing number of pulses, until a constant value is reached. In the case PVC+CNPs, variations are observed only at low fluences, shown in Figure(7.2,a). Moreover, as observed for PMMA in Figure(7.2,b), at low fluences impulse starts to be generated after some pulses. This is reasonably due to an incubation process, as also described in literature for similar experimental conditions[6]. The same explanation holds also at higher fluences, but is also interesting to note that a maximum in impulse generation is observed during the first pulses. This is not expected when considering incubation from the point of view of ablated mass or crater depth, since they only show an increasing behaviour with the number of pulses in the same region.

This observed increase in impulse generation is a interesting result when con-

sidering polymers as candidates for LAP fuel materials, since multiple pulses allow to increase C_m . This holds in particular if they are compared to the opposite behaviour observed for metals. On the other hand, material properties are well known only at the first pulse, so that it is easier in this case to relate them to impulse generation.

7.2 Measurements of specific impulse

Specific impulse defines the mass consumption efficiency in the impulse generation process and is a common parameter to assess the performances of a space propulsion system. Recalling the definition given in Chapter 1 (equation (1.6)) it is defined by

$$I_{sp} = \frac{\text{generated impulse}}{\text{expelled weight}} = \frac{m_e v_e}{m_e g} \quad (7.1)$$

Once mechanical impulse is measured, the most straightforward way to obtain I_{sp} requires then to measure the mass ejected during impulse generation (m_e). It is worth mentioning, that from equation (7.1) it can be written as $I_{sp} = v_e/g$, so that a measurement of v_e is sometimes performed to obtain I_{sp} [7]. I_{sp} values obtained by measuring m_e or v_e are in general different, and this second strategy is also the most problematic one, since measurement is made far from the ablated region and v_e changes during expansion in vacuum[8]. A measurement of m_e is then preferable.

The main problem related to ablated mass measurement is that, being m_e extremely small, a large number of pulses is required to obtain a measurable mass loss. As presented in Chapter 3, the experimental apparatus allows to move the target while laser irradiates it at a given frequency, so that similar surface conditions are almost guaranteed.

Two different problems arise when considering m_e measurements on metals and polymers. In the case of metals, for fluences below phase explosion threshold, $m_e \sim 10^{-1}$ ng, so that about 10^5 pulses are in principle needed to detect a mass variation with a balance having 10^{-5} g resolution. This means that, even if the target is continuously moving during irradiation, the same region will be ablated some tens of times during the measurement. Consequently, as previously discussed, also variations in impulse generated by multiple irradiations of the same region must be considered. In the case of

polymers, on the other hand, ablation proceeds with the chemical modification of the irradiated region: the material then changes at every pulse and multiple irradiation in the same place is not possible. Despite this problem, there is the advantage with respect of metals that much higher $m_e \sim \mu\text{g}$ are commonly observed, so that reliable measurements are possible with about one hundred pulses.

Ablated mass per pulse and I_{sp} for a PVC+1wt%CNPs(500 nm) is presented

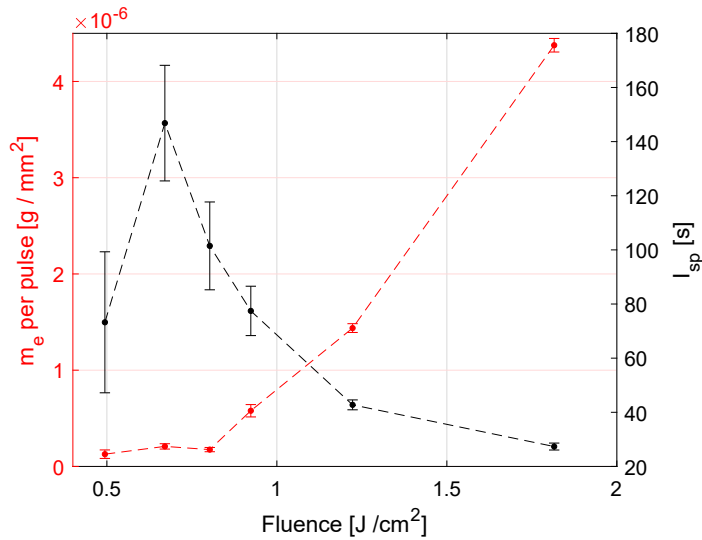


Figure 7.3: Specific impulse measured for a sample of PVC+1wt%CNPs(500 nm)

in Figure(7.3). Mass ejected during laser ablation of polymers is considerably higher than that removed from metals, therefore even if also a higher impulse is observed for polymers, the net effect is that a lower I_{sp} is obtained. Ablated mass shows a roughly constant part at low fluences and successively starts to grow linearly. The change in behaviour of ablated mass is probably related to the onset of fractures and possible ejection of some solid products during ablation, but this is still not clear.

Figure(7.4) presents ablated mass and respective computed I_{sp} as a function of laser fluence for Aluminum and Copper. Looking at ablated mass it appears that it grows increasingly faster with fluence, due to onset of phase explosion. However at low fluences m_e can be hardly measured, even with more than 10^5 pulses. As said, increasing the number of pulses causes the

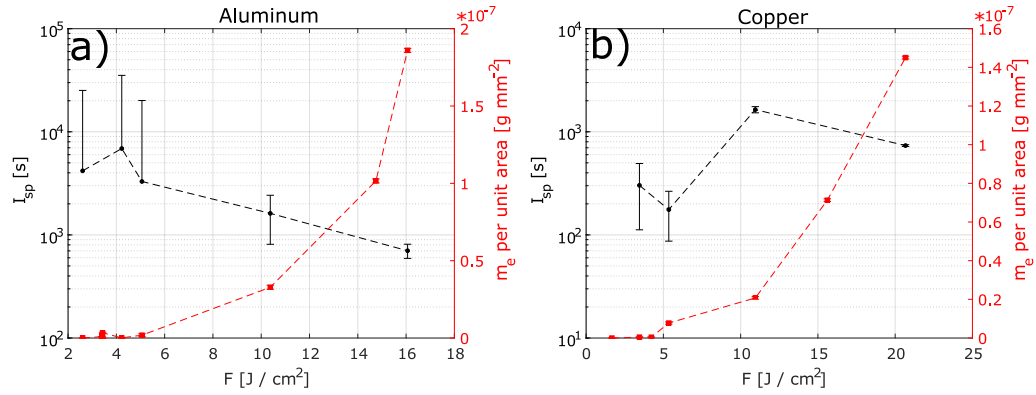


Figure 7.4: Specific impulse measured for metals. **a)**Aluminum, at low fluences the lower limit of the error bar is not shown because it is below 0 s; **b)**Copper.

multiple irradiation of the same region of the target, therefore the fact that generated impulse changes with successive irradiation must be taken into account. Considering in particular the low fluence measurements, the same region is ablated for about 50 times, while impulse reaches a constant value after roughly 3 pulses, as shown in Figure(7.1). It is then reasonable to compute I_{sp} using as impulse the constant value reached after some pulses and the estimated value of m_e . As clear from Figure(7.4) this approach gives results of the same order of magnitude of those presented in literature [9, 7, 10, 11] but very large uncertainties appear at low fluences, because measured impulse is compatible with zero.

I_{sp} in a low fluence regime, is the most attractive parameter to assess propulsion performances of metals. This is because extremely small values of m_e may result in a very high I_{sp} , that can be promising for applications in long missions.

Surprisingly, the problems in I_{sp} measurements here presented are mainly related to impulse measurement rather than to the estimation of m_e . Possible future works then might be useful to further reduce errorbars and understand if this impulse generated after some pulses at low fluences is really zero or not, so that more reliable I_{sp} values can be obtained. Another open question is instead more closely related to ablated mass: while generated impulse changes for successive pulses, it is still not clear if this happens also for ablated mass. This is also problematic from an experimental point of

view, since it would require to measure m_e avoiding multiple irradiation of the same region, but this would also drastically reduce the possible number of pulses on the same target and total removed mass would not be sufficient to be detected.

7.3 Confined ablation

Confining the expansion of the ablation products results in a considerable increase in the generated impulse. This strategy recently attracted some interest, and experiments were conducted mainly using water as confining medium[4]. Moreover, since generated impulse is related to momentum conservation, the ejection of the heavy confinement agent also contribute to this phenomenon.

An experiment is therefore conducted to test this possibility on polymer targets. PVC+1wt%CNPs(500 nm) is again chosen as reference material, since its impulse curve is well known. To add a confinement agent and to ensure a good contact between it and the surface of the material, the multilayer spin coating procedure developed in Chapter 5 is exploited by adding a layer of blank PVC on top of the PVC+CNPs film. Due to the dissolution of the interface between the two successive layers, there is not a net separation between the material to ablate and the confining medium, but rather a sharp gradient in absorption coefficient. This is confirmed by SEM analysis on the

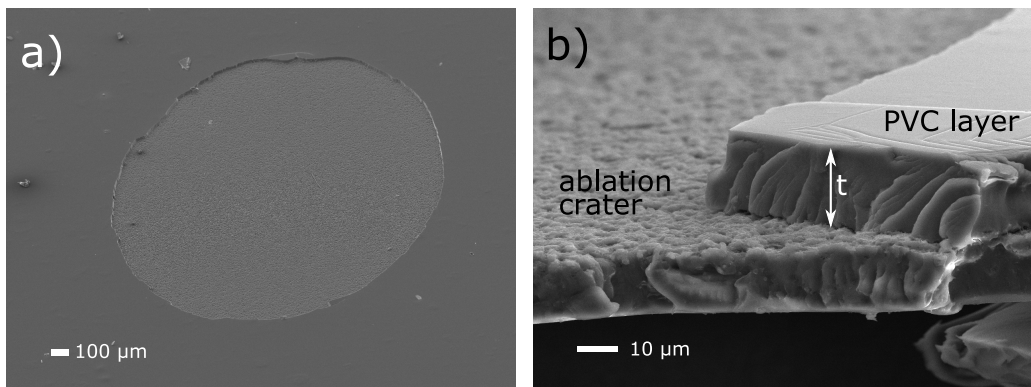


Figure 7.5: SEM images on the ablation craters obtained in the confined geometry. **a)** surface; **b)** cross section.

ablation craters, shown in Figure(7.5), where the removal of the PVC layer is

clearly visible in the irradiated region. Looking at the cross section of craters presented in Figure(7.5,b) allows also to estimate a thickness $t \simeq 20 \mu\text{m}$ of the removed confining layer.

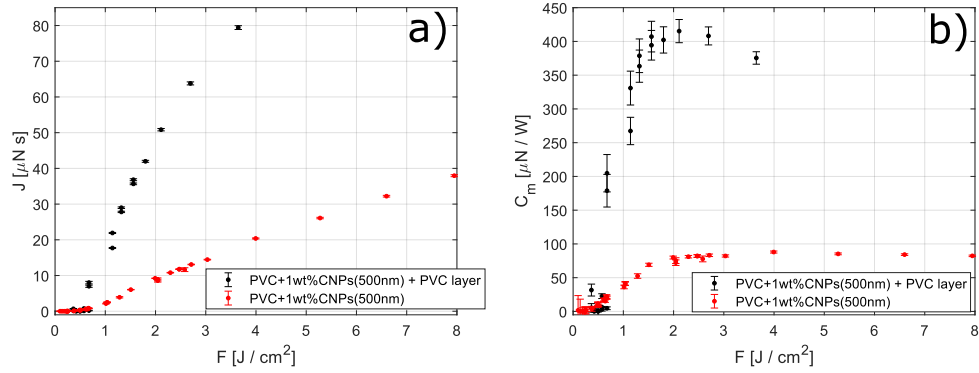


Figure 7.6: Measured impulse in confined geometry, compared with the non confined case. **a)**Generated impulse; **b)** C_m .

As visible in Figure(7.6,a) a sharp fluence threshold for impulse generation is observed, beyond which impulse grows much faster than that measured for the same material without the confining layer. This enhancement of generated impulse clearly reflects in C_m , as visible in Figure(7.6,b). Differently to what observed without the confining layer, C_m curve obtained in this case shows a maximum and a decreasing part.

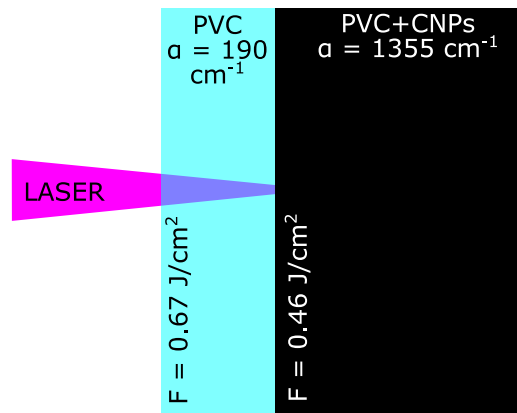


Figure 7.7: Scheme of the employed confined geometry

It is also possible to relate the measured value of impulse generation threshold for this material with and without the confinement layer. As measured in Chapter 6, this threshold without confinement layer is $F_{th} = 0.48 \pm 0.07 \text{ J/cm}^2$, while adding the confinement layer $F_{th,conf} = 0.67 \pm 0.01 \text{ J/cm}^2$ is obtained. When the confinement layer is present, a small fraction of laser energy is absorbed by the PVC layer as represented in Figure(7.7). Fluence reaching PVC+CNPs then can be estimated by Lambert-Beer law

$$F(t) = F_0 \exp(-\alpha_{PVC}t) \quad (7.2)$$

Where $\alpha_{PVC} = 190 \text{ cm}^{-1}$ is the absorption coefficient of the PVC layer and F_0 and $F(t)$ are respectively the incoming laser fluence and fluence transmitted by the confinement layer. Through equation (7.2) a fluence threshold $F'_{th} = 0.46 \text{ J/cm}^2$ is obtained, that is compatible with F_{th} measured without confinement layer. This suggests that ablation occurs on the PVC+CNPs material, so that ejected products are confined by the PVC layer.

Of Course in this configuration the ablated mass considerably increases, since it is composed by the mass of the confining PVC layer and the ablated PVC+CNPs, where this second contribution can be reasonably neglected. Ablated mass measurements in this conditions haven't been done yet, but it is possible to make a rough estimation of the mass of the ejected confining layer by multiplying its volume by PVC density. In this way a value of $m_e \sim 1.6 \times 10^{-4} \text{ g}$ is obtained, roughly ten times higher than measured values in the non confined configuration. This will cause a reduction in I_{sp} , since confinement increases generated impulse by about four times.

Bibliography

- [1] C. R. Phipps, E. Y. Loktionov, C. Bonnal, S. A. E. Boyer, E. Sharaborova, and G. Tahan. Is laser space propulsion practical?: review. *Appl. Opt.*, 60(31):H1–H11, Nov 2021. doi: 10.1364/AO.434245.
- [2] R. Fabbro, J. Fournier, P. Ballard, D. Devaux, and J. Virmont. Physical study of laser-produced plasma in confined geometry. *Journal of Applied Physics*, 68(2):775–784, 1990. doi: 10.1063/1.346783.
- [3] Zheng Zhi-Yuan, Zhang Jie, Hao Zuo-Qiang, Yuan Xiao-Hui, Zhang Zhe, Lu Xin, Wang Zhao-Hua, and Wei Zhi-Yi. The characteristics of

- confined ablation in laser propulsion. *Chinese Physics*, 15(3):580, mar 2006. doi: 10.1088/1009-1963/15/3/023.
- [4] Matej Senegačnik, Matija Jezeršek, and Peter Gregorčič. Propulsion effects after laser ablation in water, confined by different geometries. *Applied Physics A*, 126(2):1–12, 2020.
- [5] Soojin Choi, Tae-hee Han, Ardian B Gojani, and Jack J Yoh. Thrust enhancement via gel-type liquid confinement of laser ablation of solid metal propellant. *Applied Physics A*, 98(1):147–151, 2010.
- [6] R. Srinivasan, Bodil Braren, and Kelly G. Casey. Nature of “incubation pulses” in the ultraviolet laser ablation of polymethyl methacrylate. *Journal of Applied Physics*, 68(4):1842–1847, 1990. doi: 10.1063/1.346620.
- [7] Andrew V. Pakhomov, M. Shane Thompson, and Don A. Gregory. Ablative laser propulsion: A study of specific impulse, thrust and efficiency. *AIP Conference Proceedings*, 664(1):194–205, 2003. doi: 10.1063/1.1582108.
- [8] Jacopo Terragni, Pietro Battocchio, Nicola Bazzanella, Michele Orlandi, William J. Burger, Roberto Battiston, and Antonio Miotello. Evaluation of the role of beam homogeneity on the mechanical coupling of laser-ablation-generated impulse. *Appl. Opt.*, 60(31):H37–H44, Nov 2021. doi: 10.1364/AO.432991.
- [9] Andrew V. Pakhomov and Don A. Gregory. Ablative laser propulsion: An old concept revisited. *AIAA Journal*, 38(4):725–727, 2000. doi: 10.2514/2.1021.
- [10] Claude R Phipps, James R Luke, and Wesley D Helgeson. 3ks specific impulse with a ns-pulse laser microthruster. Technical report, PHOTONIC ASSOCIATES SANTA FE NM, 2005.
- [11] Claude R. Phipps, James R. Luke, and Wesley Helgeson. Laser-powered multi-newton thrust space engine with variable specific impulse. In Claude R. Phipps, editor, *High-Power Laser Ablation VII*, volume 7005, page 70051X. International Society for Optics and Photonics, SPIE, 2008. doi: 10.1117/12.786459.

Conclusion

This thesis presented Laser Ablation Propulsion (LAP) as a new attractive space propulsion technique, that offers a solution both for space debris removal and control of nanosatellites. The goal of this work was to study the main phenomena involved in laser ablation and their role in the generation of a mechanical impulse, by developing the experimental apparatus and procedures needed to measure it. This then constitutes a test facility to study specifically designed materials for LAP applications, allowing to understand how their properties are related to propulsion performances and how they can be improved.

The technological and economical environment in which LAP must be included is described in Chapter 1. Here the recent changes in space economy are reviewed, showing that the advent of private companies in this market led to an extremely fast increase in the number of satellites in orbit. Design and fabrication of satellites moreover is accelerated by reducing and standardizing their shape down to few kg mass and few cm size. This drastic reduction in size then requires the miniaturization of propulsion systems that are still lacking for these nanosatellites, so that LAP becomes an attracting solution and the development of fuel materials is required. On the other side, this vast exploitation of space produced a large number of orbiting debris, so that solutions to remove them are needed: also in this case LAP represents a promising technique to clean earth orbit.

The fundamental mechanisms at the base of laser ablation are described in Chapter 2, discussing the different processes that occur in the case of metals and polymers. In the case of metals, interaction with the laser pulse leads to a fast temperature increase that cause vaporization and, if laser fluence is sufficiently high, also phase explosion with ejection of liquid metal nan-

odroplets. In the case of polymers, ablation proceeds by the decomposition of the material into volatile products, that may occur because of a temperature increase or a chemical reaction activated by laser photons.

These different ablation mechanisms lead to different impulse generation performances. In the case of metals the ejection of light, high temperature products results in the observation of high I_{sp} values, comparable to those observed in ion thrusters. Polymers on the other hand may eject heavier products, like large molecules up to solid fragments, and they usually have lower threshold fluences for impulse generation, so that high C_m are obtained.

Chapter 3 deals with the experimental measurement of laser generated mechanical impulse. The measurement is based on the detection of the variation in angular momentum of a ballistic pendulum that operates in vacuum, whose motion and geometric and mass properties are measured through image analysis techniques. The accurate design of the apparatus and in particular of the pendulum allowed to reduce damping of oscillation, so that an harmonic motion can be correctly assumed. Additionally, the good estimation of the moment of inertia of the pendulum, that depends on the target fixed on it, allowed to obtain reproducible impulse measurements, that can be used to assess propulsion performances of the tested material.

The main parameter to study impulse generated during ablation is laser fluence, therefore it must be correctly estimated. Chapter 4 deals with fluence estimation, comparing the effects on impulse generation of a non-uniform and uniform spatial distribution of laser intensity. It is observed that difficulties appear in fluence estimation in the case of a non-uniform intensity distribution, that result in discrepancies observed in impulse curves. This problem is then solved by introducing a beam homogenizer, that produces a uniform intensity distribution, allowing to properly estimate fluence.

A first investigation of polymers for LAP applications in nanosatellites is discussed in Chapter 5. Poly(vinyl chloride) (PVC) is considered as starting polymer, that represents a sort of benchmark for LAP experiments. To increase its absorption of laser radiation, that in this case is at a wavelength of 248 nm, carbon nanoparticles (CNPs) are usually included in PVC. Here CNPs inclusion in the polymer is compared with the mixing of PVC with poly(styrene sulfonate) (PSS), an absorbing polymer at laser wavelength. The polymers are characterized from the structural, optical and thermo-

dynamical point of view, and impulse generated by their laser ablation is measured.

Laser ablation of both these polymers proceeds with their thermal decomposition, and it is observed that lower thermal energy is needed to decompose PVC:PSS. On the contrary impulse measurements showed that lower fluence is required to ablate PVC+CNP. This allows to demonstrate that the localized absorption obtained with the inclusion of CNPs is a more efficient strategy to enable ablation of PVC and gives a guideline for the development of polymers for LAP applications.

Experiments on PVC+CNP are conducted also in Chapter 6, with the goal of understanding how CNPs properties like size, morphology and concentration affect ablation and impulse generation. Different CNPs, both commercial and synthesised, are therefore included in PVC and samples are characterized looking at their structure, optical properties, and comparing impulse generation. Moreover the ablation mechanism through thermal decomposition is confirmed by analyzing composition and structure of ablation craters.

Variations in optical absorption are observed, and the main parameter governing it is found to be the number density of CNPs in the polymer, that in turn depends on CNPs size and concentration. Moreover the measured threshold fluence for impulse generation (F_{th}) is also affected by CNPs number density, since it decreases down to a constant value with increasing optical absorption. By analyzing ablation craters, F_{th} behaviour can be explained by the fact that PVC decomposition occurs around each CNP and that an increased number density of CNPs results in a more efficient heat distribution. The constant lower limit value observed for F_{th} is also explained by considering that below that fluence PVC decomposition around each single CNP is not initiated. This results then reveal other important features to consider in the development of LAP materials.

At last, Chapter 7 briefly discuss some preliminary experiments still under discussion, that show some of the open questions and future works in this research. A situation a bit closer to real applications is considered by looking at how generated impulse changes by irradiating multiple times the same region. Here a considerably different behaviour is observed between metals and polymers, with this first category showing a decrease in generated impulse, while in the second case it increases. While impulse increase

observed for polymers can be expected due to incubation phenomenon, the reason for the results on metals are still not clear.

Some results and problems related to the measurement of I_{sp} are then presented, showing that the main problem in metals is related to the fact that a very small mass is ejected during ablation.

Then an attracting possibility to increase impulse generation is briefly tested by confining ablation of PVC+CNP with a transparent PVC layer. Promising results are obtained here, however some work is still needed to clarify the ablation process and to overcome application problems.

To conclude, this thesis shows that Laser Ablation Propulsion can be considered as an attractive future propulsion technique for nanosatellites and a solution for space debris removal, two of the main emerging problems in the New Space Economy. Promising results are obtained both in the development of the experimental apparatus and in the study of materials to be employed in LAP, highlighting some important features for the development of future propellants. Obtained results also show that still work has to be done to move towards a real application of LAP, but it is also clear that many possibilities still haven't been explored, making LAP a promising candidate for the future of space activities.